NAVAL POSTGRADUATE SCHOOL
Monterey, California

19980414 090

THESIS

THE EFFECT OF WATER TEMPERATURE ON UNDERBEAD CRACKING OF UNDERWATER WET WELDMENTS

by

Robert L. Johnson

September 1997

Thesis Advisor: Alan G. Fox

Approved for public release; distribution is unlimited.

DTIC QUALITY INSPECTED 3

REPORT DOCUMENTATION PAGE

Form Approved
OMB No. 0704-0188

Public reporting burden for this collection of information is estimated to average 1 hour per response, including the time for reviewing instruction, searching existing data sources, gathering and maintaining the data needed, and completing and reviewing the collection of information. Send comments regarding this burden estimate or any other aspect of this collection of information, including suggestions for reducing this burden, to Washington headquarters Services, Directorate for Information Operations and Reports, 1215 Jefferson Davis Highway, Suite 1204, Arlington, VA 22202-4302, and to the Office of Management and Budget, Paperwork Reduction Project (0704-0188) Washington DC 20503.

1. AGENCY USE ONLY *(Leave blank)*	**2. REPORT DATE** September 1997	**3. REPORT TYPE AND DATES COVERED** Master's Thesis

4. TITLE AND SUBTITLE THE EFFECT OF WATER TEMPERATURE ON UNDERBEAD CRACKING OF UNDERWATER WET WELDMENTS	**5. FUNDING NUMBERS**
6. AUTHOR(S) Johnson, Robert L.	
7. PERFORMING ORGANIZATION NAME(S) AND ADDRESS(ES) Naval Postgraduate School Monterey, CA 93943-5000	**8. PERFORMING ORGANIZATION REPORT NUMBER**
9. SPONSORING / MONITORING AGENCY NAME(S) AND ADDRESS(ES) Naval Sea Systems Command (NAVSEA OOC) 2531 Jefferson Davis Hwy Arlington, VA 22242-5160	**10. SPONSORING / MONITORING AGENCY REPORT NUMBER**

11. SUPPLEMENTARY NOTES

The views expressed in this thesis are those of the author and do not reflect the official policy or position of the Department of Defense or the U.S. Government.

12a. DISTRIBUTION / AVAILABILITY STATEMENT Approved for public release; distribution is unlimited.	**12b. DISTRIBUTION CODE**

13. ABSTRACT *(maximum 200 words)*

Specifications for Underwater Welding have not yet addressed the effect of water temperature on weldment microstructure. The environmental effects on Underwater Wet Welding using a shielded metal arc welding (SMAW) process are severe with higher quenching rates, porosity, slag inclusions and diffusible hydrogen levels.

One of the problems associated with these high quenching rates and high diffusible hydrogen levels is the increased likelihood of underbead cracking in the heat affected zone (HAZ), particularly with steel weldments which have a higher carbon equivalent (approximately greater than 0.3). In this work, the underbead cracking resulting in three underwater test welds made on ASTM 516 grade 70 steel at three different water temperatures (2.8°C, 10°C and 31°C) was investigated. This was done by optical and scanning electron microscopy (SEM) and by making microhardness measurements.

HAZ underbead cracking was observed in all three weldments, but was much less prevalent in the 31°C sample and could only be seen at high magnifications in the optical microscope. The cracking in this weldment only appeared to occur in isolated regions where bead tempering had been ineffective for some reason. The weldments made at 10°C and 2.8°C both showed extensive evidence of underbead HAZ cracking typical of that associated with rapid cooling rates, high diffusible hydrogen levels and hard microstructures. SEM studies of the surfaces of these cracks showed evidence for transgranular failure with secondary cracking, both of which are typical of hydrogen induced cracking.

This work highlights the importance of water temperature, quenching and diffusible hydrogen levels in underwater wet welding. This is an issue of critical importance in the future wet welding structural repair of Naval ships.

14. SUBJECT TERMS Underwater wet welding, Hydrogen cracking, Underbead cracking, Non-metallic inclusions, Shielded Metal Arc Welding	**15. NUMBER OF PAGES** 108
	16. PRICE CODE

17. SECURITY CLASSIFICATION OF REPORT Unclassified	**18. SECURITY CLASSIFICATION OF THIS PAGE** Unclassified	**19. SECURITY CLASSIFICATION OF ABSTRACT** Unclassified	**20. LIMITATION OF ABSTRACT** UL

NSN 7540-01-280-5500

Standard Form 298 (Rev. 2-89)
Prescribed by ANSI Std. 239-18

DTIC QUALITY INSPECTED 3

Approved for public release; distribution is unlimited.

THE EFFECT OF WATER TEMPERATURE ON UNDERBEAD CRACKING OF UNDERWATER WET WELDMENTS

Robert L. Johnson
Lieutenant, United States Navy
B.M.E., Cleveland State University, 1987

Submitted in partial fulfillment of the
requirements for the degree of

MASTER OF SCIENCE IN MECHANICAL ENGINEERING

from the

NAVAL POSTGRADUATE SCHOOL
September 1997

Author: ______________________________
Robert L. Johnson

Approved by: A.G. Fox
Alan G. Fox, Thesis Advisor

____
Terry R. McNelley, Chairman
Department of Mechanical
Engineering

ABSTRACT

Specifications for Underwater Welding have not yet addressed the effect of water temperature on weldment microstructure. The environmental effects on Underwater Wet Welding using a shielded metal arc welding (SMAW) process are severe with higher quenching rates, porosity, slag inclusions and diffusible hydrogen levels.

One of the problems associated with these high quenching rates and high diffusible hydrogen levels is the increased likelihood of underbead cracking in the heat affected zone (HAZ), particularly with steel weldments which have a higher carbon equivalent (approximately greater than 0.3). In this work, the underbead cracking resulting in three underwater test welds made on ASTM 516 grade 70 steel at three different water temperatures (2.8°C, 10°C and 31°C) was investigated. This was done by optical and scanning electron microscopy (SEM) and by making microhardness measurements.

HAZ underbead cracking was observed in all three weldments, but was much less prevalent in the 31°C sample and could only be seen at high magnifications in the optical microscope. The cracking in this weldment only appeared to occur in isolated regions where bead tempering had been ineffective for some reason. The weldments made at 10°C and 2.8°C both showed extensive evidence of underbead HAZ cracking typical of that associated with rapid cooling rates, high diffusible hydrogen levels and hard microstructures. SEM studies of the surfaces of these cracks showed evidence for transgranular failure with secondary cracking, both of which are typical of hydrogen induced cracking.

This work highlights the importance of water temperature, quenching and diffusible hydrogen levels in underwater wet welding. This is an issue of critical importance in the future wet welding structural repair of Naval ships.

TABLE OF CONTENTS

I. INTRODUCTION 1

II. BACKGROUND 3

A. UNDERWATER WELDING 3

1. Underwater Wet vs. Dry Hyperbaric Welding 4
2. Underwater Welding vs. Dry Docking 5

B. UNDERWATER WET SHIELDED METAL ARC WELDING 6

C. THE HEAT AFFECTED ZONE MICROSTRUCTURE OF UNDERWATER WET WELDS MADE ON FERRITIC STEEL 7

1. Material Selection 8
2. Rapid Cooling Rate 9
3. Hydrogen Cracking 10

D. THE FUSION ZONE MICROSTRUCTURE OF UNDERWATER WET WELDS 11

1. Fusion Zone Grain Structure 11
2. Environmental Effects 13
3. Alloying and Consumable Effects 15
4. Non-Metallic Inclusions 16

E. SCOPE OF THE PRESENT WORK 17

III. EXPERIMENTAL PROCEDURE 37

A. WELD SAMPLES 37

B. SAMPLE PREPARATION 37

C. SCANNING ELECTRON MICROSCOPY 38

D. OPTICAL MICROSCOPY 39

E. MICROHARDNESS ANALYSIS 39

IV. RESULTS AND DISCUSSION 49
  A. WELD METAL 49
    1. Weld Metal Composition 49
    2. Electrode Composition 49
  B. NON-METALLIC INCLUSIONS 50
    1. Size and Volume Fraction 50
    2. Inclusion Differential Chemical Analysis 50
    3. Inclusion Observations 51
  C. MICROHARDNESS ANAYLSIS 52
  D. MICROSTRUCTURAL ANALYSIS 52
    1. Macroscopic 52
    2. Microscopic 52
    3. Fractography 55

V. SUMMARY 57
  A. CONCLUSIONS 57
  B. RECOMMENDATIONS 57

LIST OF REFERENCES 87

INITIAL DISTRIBUTION LIST 91

LIST OF FIGURES

2.1 Sketch of the welding and safety equipment configuration for underwater welding and cutting..19

2.2 Sketch of the shielded metal arc welding process.........19

2.3 Graville Diagram. The dashed line shows the suggested modification to the boundary between Zone II and III for underwater wet welding.........20

2.4 Welding CCT diagram for A516 Gr 70 steel of simulated CGHAZ with 1320°C peak temperature and 25°C preheat for 2.5 cm thick plate.........21

2.5 A schematic diagram of the various HAZ regions approximately corresponding to those indicated on the Fe-Fe_3C equilibrium diagram for a single pass weld.........22

2.6 A schematic diagram of multipass weld HAZ Microstructure.........23

2.7 Cooling time as a function of arc energy for surface and underwater welding.........24

2.8 Effect of water temperature on peak temperature and cooling rate (800°C-500°C) at a point 1 mm distant from the fusion line on the plate surface.........24

2.9 Diffusion of hydrogen from weld metal to HAZ during welding.........25

2.10 Competitive growth in the fusion zone.........25

2.11 Columnar-grain structure at high (a) and low (b) welding speeds.........26

2.12 Nucleation mechanism vs. microstructure around the weld pool boundary of an alloy.........26

2.13 Heterogeneous nucleation mechanism resulting in the formation of equiaxed grains in weld metal.........27

2.14 Schematic rate-gradient map showing transition in microstructure as well as refining effect of high cooling rates.........27

2.15 CCT diagram and influence of the cooling rate on weld metal microstructure.........28

2.16 Alloying element variation in underwater wet welding vs. water depth.........28

2.17 Schematic CCT diagram showing the influence of weld metal oxygen & manganese on hardenability.........29

2.18 Variation of the oxygen & manganese contents with depth of underwater welding.........29

2.19 Product of weld metal carbon and oxygen content vs. water depth for weld metal produced with treated E6013 SMA electrode.........30

2.20 Combined effects of weld metal boron and titanium on volume fraction of acicular ferrite for surface welding.........30

2.21 Effects of boron and titanium on weld metal oxygen levels of underwater wet welds.........31

2.22 Effect of titanium on manganese and silicon content in underwater wet welds.........31

2.23 Effect of boron and titanium on weld metal hardness of underwater wet welding.........32

2.24 Contour map of acicular ferrite as a function of weld metal boron and titanium content of underwater wet welding.........32

2.25 Effect of $CaCO_3$ on weld metal porosity of underwater welds.....33
2.26 Effect of $CaCO_3$ in the electrode coating on weld metal diffusible Hydrogen levels in surface welds.....33
2.27 Composition profile for unidirectional thickening of inclusion growth.....34
2.28 Schematic representation of the effect of inclusion size on austenite grain size and acicular ferrite formation.....35
3.1 SEM micrograph illustrating (a) typical inclusion field and (b) method of measurement.....45
3.2 Macrophotograph of UWW03 weld sample. Welded at a depth of 6.7m in seawater and at a temperature of 2.8°C.....46
3.3 Macrophotograph of UWW10 weld sample. Welded at a depth of 5.5m in seawater and at a temperature of 10°C.....47
3.4 Macrophotograph of UWW31 weld sample. Welded at a depth of 7.3m in freshwater and at a temperature of 31°C.....48
4.1 (a) Typical Weld Metal EDX Spectrum, without backscatter detector in place.
(b) Typical Weld Metal EDX Spectrum, with backscatter detector in place.....62
4.2 SEM Micrograph of BROCO CS-1 Cross-section.....63
4.3 SEM Micrograph of BROCO CS-1 Flux.....63
4.4 SEM Micrograph of BROCO CS-1 Special coating.....64
4.5 Typical Oxide Inclusion EDX Spectrum.....65
4.6 Typical Slag Inclusion EDX Spectrum.....65
4.7 Schematic diagram showing generation of electrons & x-rays with in the specimen.....66
4.8 UWW03 Total Inclusion Distrubution.....67
4.9 UWW03 Slag Inclusion Distrubution.....67
4.10 UWW03 Oxide Inclusion Distrubution.....68
4.11 UWW10 Total Inclusion Distrubution.....69
4.12 UWW10 Slag Inclusion Distrubution.....69
4.13 UWW10 Oxide Inclusion Distrubution.....70
4.14 UWW31 Total Inclusion Distrubution.....71
4.15 UWW31 Slag Inclusion Distrubution.....71
4.16 UWW31 Oxide Inclusion Distrubution.....72
4.17 Traverse Vicker's Hardness for Mid-section of each Weldment.....73
4.18 Traverse Vicker's Hardness for the Last Pass Weld Cap.....74
4.19 Porosity and Slag seen in UWW31 weld sample.....75
4.20 Large silicate matrix slag inclusion with Wustite dendrites (FeO).....75
4.21 Subcritical HAZ, 240.1HV.....76
4.22 Intercritical HAZ, 289.3HV.....76

4.23 Fine Grain HAZ, 429.0HV 77
4.24 Coarse Grain HAZ, 503.1HV 77
4.25 Solid-Liquid Transition Zone, 342.6HV 78
4.26 Columnar Grain FZ, 295.1HV....................78
4.27 Overall View of the Last Pass of UWW31....................79
4.28 Fine HAZ cracking, near Vicker's hardness readings on the left side near the mid-section of UWW31 79
4.29 Fine HAZ cracking on the left side near the lower section of UWW31....................80
4.30 Edge of Fusion zone, 273.1 HV 80
4.31 Weld metal field with large slag inclusions and smaller inclusions with acicular ferrite, 257.3 HV. 81
4.32 Columnar grain structure with widmanstatten ferrite and acicular ferrite, 227.7HV....................81
4.33 Upper crack in UWW10 weld sample from HAZ into the weld metal....................82
4.34 Lower crack in UWW10 weld sample from HAZ into the weld metal 82
4.35 Underbead cracking from top of weld. UWW03....................83
4.36 Underbead cracking sceond from top. Cracking progressed into the weld metal along the columnar grains....................83
4.37 Underbead cracking third from top. UWW03....................84
4.38 Underbead cracking fourth from top. The crack steps along the fusion line between the weld metal and the HAZ....................84
4.39 Underbead cracking fifth from top. UWW03 85
4.40 SEM of transgranular cracking on the surface of the fracture with secondary cracking. 85
4.41 SEM of transgranular cracking on the surface of the fracture with secondary cracking. 86
4.42 SEM of fracture surface that progressed into the weld metal.. 86

LIST OF TABLES

3.1 The welding conditions and parameters. 41

3.2 Base metal ASTM A516 Gr70 steel chemical analysis.. 41

3.3 Nominal Composition for E7014 Electrodes. 42

3.4 Microconstituent volume fraction for UWW03. 43

3.5 Microconstituent volume fraction for UWW10. 43

3.6 Microconstituent volume fraction for UWW31. 43

3.7 Microhardness testing from the initial failure at Puget Sound Naval Shipyard. 44

4.1 Weld metal, Filler rod, and Flux/coating EDX chemical composition analysis. 59

4.2 Inclusion statistics and volume fraction, UWW03 60

4.3 Inclusion statistics and volume fraction, UWW10. 60

4.4 Inclusion statistics and volume fraction, UWW31. 60

4.5 Weld Sample Vicker's Microhardness Data... 61

ACKNOWLEDGMENT

I would like to acknowledge the financial support from the Supervisor of Salvage and Diving (NAVSEA OOC). I hope to work on underwater welding again soon.

To Professor Alan Fox, I hope that your loss brings peace. I appreciate the freedom that you gave me in research. It was a pleasure to discuss the topic of underwater welding (UWW) with you. Best of luck in your future UWW research; I hope it is productive.

Finally, my wife, Lisa, and sons Derek & Tyler. Without your patience, love and support I would not have been able to produce this thesis in such a short time. Sorry for the missed bedtime stories!

I. INTRODUCTION

In 1993, changes in the specification of underwater welding [Ref. 1] were made and provisions for making underwater welds (Class A) which meet the same requirement of surface weldments became possible. However, to date underwater wet welds have not been able to meet this requirement. The U.S. Navy has played a major role in developing wet welding techniques [Ref. 2, 3], an interest spurred by increased maintenance costs.

Unfortunately, with high cooling rates and hydrogen levels coupled with a brittle microstructure, the wet welding environment presents a very difficult problem for a metallurgist. Most commercially available wet welding electrodes are modified with special coatings designed to limit water absorption in a effort to lower hydrogen levels in the weldment.

More recently, the results of underwater wet welding procedure qualification testing on ASTM A516Gr70 steel [Ref. 4] have shown extensive hydrogen cracking. This cracking is apparently a result of water temperature. Now the desire to produce strong, tough and cost effective welds for ship repair has possibly a new critical factor to overcome.

Currently, the Office of the Director of Ocean Engineering, Supervisor of Salvage and Diving (NAVSEA OOC) has directed the Naval Postgraduate School (NPS) to conduct an evaluation of the influence of water temperature on cracking in underwater welds. This began by investigation of the failed procedure testing on A516Gr70 steel weldments. The lower temperature tests resulted with extensive underbead cracking which is apparently hydrogen induced. Since wet shielded metal arc welding produces the most cost effective underwater weldments, it is necessary to overcome the poor quality results ecountered due to the wet and cold environment. The specific focus of this study is to investigate the mechanism of the cracking and the microstructure.

II. BACKGROUND

A. UNDERWATER WELDING

Welding underwater is a unique process, the obvious problem being with welding at a submerged work site. There has been increased use of underwater techniques due to offshore industry. There are two general classifications of underwater welding, wet and dry, both of which are normally exposed to the ambient pressure. Many terms are used to explain these techniques as defined by the American Welding Society [Ref. 1] and will be discussed below. It should be kept in mind that dry welding is any process which excludes water from the immediate location of the arc and the weld joint. Wet welding, on the other hand, is a process in which the arc, joint and the welder/diver are exposed to the water environment with both the temperature and the pressure at depth. All underwater welding processes which are exposed to a depth or pressure conditions in excess of the surface pressure of one atmosphere are called hyperbaric welds. The *Specifications for Underwater Welding* [Ref. 1] and the *Metals Handbook* [Ref. 5] are in agreement on the five types of underwater welding techniques currently in use. These are:

* One Atmosphere Welding (Chamber) - Welding is performed in a pressure chamber which is maintained at nearly the surface pressure (one atmosphere absolute). This approach is the only underwater welding technique which is not at a hyperbaric condition. The chamber is large enough to be placed around the work site and allow the welder to move freely. The welder need not be a diver and can be transferred in a pressure vessel to the chamber.

* Habitat Welding - Water is displaced from a chamber which is open to ambient pressure, thus making this weld a hyperbaric weld. The chamber is large enough that the welder/diver can freely move and is not required to wear diving dress. Both one atmosphere and habitat welding have chambers which are large enough to support elaborate weld preparation and positioning equipment. Furthermore, because the welder/diver is not required to wear diving dress, the welding and respiratory exhaust gases must be vented and a breathing gas/air must be supplied to the artificial environment. Boie et al, have done research into the effects of this artificial environment on weld metal metallurgy [Ref. 6].

* Dry-Chamber Welding (Dry-Box, Cofferdam) - Welding is performed in an open bottom gas/air filled chamber in which the welder/diver must wear diving dress and the chamber is at least large enough for his head and shoulders. This process does not require an artificial environment.

* Dry-Spot Welding - Welding is performed by displacing water from local weld joint in a small gas/air filled enclosure or with shielding gas surrounded by a concentric water jet which is at ambient pressure. The dry-spot provides a protective region between weld and the water environment which is just large enough for the electrode or the diver's torch. The welder/diver is in full diving dress and moves the dry-spot along the weld joint. There are two subcategories:

- Dry-Backed Weld Joint - The water is excluded from contact with any part of the weld joint for at least six inches.

- Wet-Backed Weld Joint - This is a dry chamber weld; however, the water surface is less than six inches from the weld joint.

* Underwater Wet Welding - Weld joint and welder/diver are located in the water and no special efforts are made to separate the weld joint from the water. The arc is struck in the water and the welder/diver moves the electrode along the joint with a drag technique

1. Underwater Wet vs. Dry Hyperbaric Welding

The use of underwater wet welding has been documented as early as the First World War [Ref. 7 and 8]. However, the use of wet welding was, for the most part, only for salvage and emergency repairs. It was an unreliable process until the first structural repairs were made in the early seventies.

With the expansion of offshore industry, the quality of underwater welding processes needed to be improved. Research into this problem led to different welding processes being used within a dry chamber, such as gas metal arc (GMAW), gas tungsten arc (GTAW) and plasma arc welding (PAW) [Ref. 7]. These processes showed improved results. However, they had limitations due to the complexity of the equipment and techniques. The poor quality of underwater wet welds that will be discussed was a result of environmental factors and, at times, a lack of skilled welder/divers.

The main process used for underwater wet welding is shielded metal arc welding (SMA). In fact, SMAW is still used within dry chambers since the cost and complexity needed to work at depth tend to favor a welding process with a higher deposition rate.

The environmental factors which effect underwater wet welding are:

* High weld joint cooling rates due to water quenching. Dry chambers do not have the water quenching problem. However, as Lythall, et al. noted [Ref. 9], the increased gas density at hyperbaric conditions will result in higher heat extraction rates. The dry chamber allows the possibility of pre-heat, post-heat and interpass temperature control.

* Wet welding has limited protection from environmental hydrogen sources. Dry chamber welding has more control over hydrogen levels along with the chamber's atmosphere.

* Wet welding processes experience arc stability problems, where as a dry chamber's arc is stable down to 300 meters.

* Wet welding has problems with poor visibility which leads to problems with arc striking. Dry chamber welding with fume extraction systems have the same visibility as surface welding.

It is clear from these comments that a metallurgist would always prefer to use dry chamber welding. However, the need to produce economical underwater weld repairs of complex weld joint design calls for a simple, flexible welding process with a high disposition rate. The technique most frequently tried is underwater wet welding using the SMAW process.

2. Underwater Welding vs. Dry Docking

As the Navy budget has shrunk and the fleet has downsized over the last few years, it has been necessary to reduce maintenance assets. The Department of Defense has directed that maintenance is to be performed at the lowest level that ensures optimum readiness and economic use of resource [Ref. 10]. There has been considerable movement within the Department of the Navy in discussing the budget and maintenance. In 1994, ADM Frank B. Kelso II, Chief of Naval Operations, initiated changes which started to integrate all three levels of maintenance.

To date, the use of underwater welding has not received as much publicity as it warrants. The use of underwater repairs waterborne has been viewed as an emergent or temporary method. Underwater welding has been evolving and more can be accomplished as a permanent repair. Unfortunately, the present Naval Shipyard organization is not equipped for optimum utilization of divers in performing underwater welding tasks. Most underwater welding services are still contracted out to a select few commercial Diving and Salvage companies. The certification and qualification of divers for complex underwater welding repair techniques is not a current practice. This study is actually a result of a failed underwater welding procedure qualification testing at a Naval Shipyard.

In 1993, the *Specification for Underwater Welding* [Ref. 1] was changed, requiring a rewrite of the capabilities and requirements for underwater welding. The change has provided a challenge and an opportunity to the Naval service. Until now, underwater cutting and welding have been used for the most part in ship salvage and harbor clearance operations. Ship repair was not the intended purpose; only via deviations and waivers were repairs undertaken and only then as emergent or temporary repairs. Now there exists the capability to complete permanent repairs for structural carbon steel welds performed on surface ship hulls in a dry chamber (cofferdam) or for non-structural carbon steel welds performed as underwater wet welding. Moreover, this change provides the qualification requirements for both the underwater welding and non-destructive testing (NDT) for both procedures and personnel. In short, these standards have been raised to a surface equivalent in qualification and quality.

An illustrative example of underwater repair work in a depot occurred in September of 1993. USS Providence (SSN-719) was completing a depot maintenance period (DMP) at Charleston Naval Shipyard (CNSY) and was preparing for sea trials. The high pressure air (HPA) system was unable to obtain a proper dewpoint due to an air flask being partially filled with water. The initial reaction was to put the ship back into drydock.

Eventually, the Shipyard Chief Engineer (Code 240) and the Shipyard Divers together investigated waterborne repair options. A hyperbaric weld repair was possible; however, the required NDT for a sub-safe joint proved too difficult. Ultimately, with a NAVSEA approved waiver, a mechanically attached fitting was installed. This was the first time a repair of this kind was completed on a nuclear submarine. At the next scheduled drydocking, the repair will be inspected and then possibly approved as a permanent repair.

This repair process was rapid. In fact, by the time the divers had completed all repairs and testing, the drydock was still unprepared for docking. Afterward, Capt. Connors at SUBLANT commented to Mr. Goblet at NAVSEA PMS 393 that this effort had saved approximately $500,000 [Ref. 11].

The above example addressed cost and schedule savings while avoiding an emergent drydocking. With fleet maintenance budgets continuing to decline, repair and maintenance engineers are challenged to find ways to maintain readiness with less. Underwater Welding and Repair offers substantial savings in three ways:

1) by reducing the need for drydocking;
2) extension of drydock intervals; and
3) underwater inspections used to develop accurate drydock work packages and order material necessary before the overhaul.

Underwater repairs are almost always faster than drydock repairs. For an operational ship, waterborne repairs can be accomplished while a ship retains its operational load-out, eliminating offload requirements for drydocking. Therefore, as advances are made in underwater welding technology, the maintenance and repair budget can be reduced or stretched to support the size of the Fleet.

VADM Kenneth C. Malley of Naval Sea Systems Command (NAVSEA) stated that "budget realities will mean fewer ships . . . Therefore, we must concentrate on . . . making them as affordable over their life cycle . . . and as operationally available as we possibly can." [Ref. 12] A key is underwater welding and repair.

B. UNDERWATER WET SHIELDED METAL ARC WELDING

Shielded metal arc is the process normally used for wet or open-water welding [Ref. 5]. The electrodes and base metal must be carefully selected and protective actions should be taken to limit water absorption in the electrodes before welding. The welder/diver is wearing a diving suit/helmet which restricts movement and visibility. The welder/diver needs a stable platform which is not affected by surge, current and waves to produce good quality welds. He must avoid becoming part of the welding circuit. Therefore, the equipment layout at the work site has some special safety measures installed. Figure 2.1 shows the equipment configuration as discussed in the *U.S. Navy Underwater Cutting and Welding Manual* [Ref. 13].

The underwater wet shielded metal arc welding process appears comparatively complex next to air welding. There are three significant differences between normal and underwater SMA welding:

* Specialized electrodes with special fluxes and waterproof coatings are needed.

* Direct current power supply and straight polarity (DCSP) is used.

* Equipment arrangement is remote to the welding site and safety devices.

However, wet welding does resemble the normal SMAW process. Since the welding arc and molten weld pool, both are protected from the environment, be it air or water, by the gaseous shield [Ref. 8]. SMA welding is an electric arc welding process in which the arc is formed between a manually fed consumable electrode and the base metal. Figure 2.2 is a sketch of the SMA welding process [Ref. 14]. The electrodes are a filler metal covered with a flux which contains metals, chemicals and elements. The filler metal conducts electric current and is selected to fit the base metal and the weld joint design. The flux covering as described by Kou [Ref. 14] performs the four following functions:

* Forms a gaseous shield to protect the molten metal when the flux is heated and decomposes.

* Contains fluxing agents deoxidize and cleanse the weld metal. A solid slag also forms and protects the weld metal after solidification.

* Ionized compounds provide arc stabilizers.

* Provides alloying elements.

C. THE HEAT AFFECTED ZONE MICROSTRUCTURE OF UNDERWATER WET WELDS MADE ON FERRITIC STEEL

In research conducted in the early seventies into the effects of the water environment, various workers [Ref. 7, 8, 15 and 16] all discussed the effect of the welds being quenched and the resulting microstructural effects. However, as noted by Szelagowski [Ref. 17], after underwater wet welding began being used and researched in the thirties, no noticeable improvements in equipment and weld quality had been achieved since the early seventies. While that may seem true at times, the truth is that significant progress has been made with wet welding electrode consumables research [Ref. 4, 15, 18, 19, 20 and 21] and their metallurgical and microstructural effects on underwater welding.

While air welds may possess properties similar to cast welds, underwater wet weldment properties are similar to quenched and cast materials. Since the weld is quenched in the HAZ of wet welds on ferritic steels, highly stressed martensite can be found. Furthermore, the increased cooling rate caused by quenching can lead to increased porosity and slag inclusions in the weld metal. These result from the limited time available for the gas and slag particles to reach to weld pool surface before rapid solidification has "trapped" them in the weld metal.

The dissociation of water in an underwater wet arc leads to increased hydrogen levels. This combination of highly stressed martensite from the rapid cooling rate effect and the hydrogen levels from the dissociation of water can lead to underbead cracking. Furthermore, there are other hydrogen-related imperfections that can result from the higher hydrogen levels which help identify the mechanism of the cracking these include: (1) the appearance of flakes on small fissures on a fractured surface that are parallel to the direction of maximum stress, (2) the appearance fisheyes (bright spots with cracks at their centers) on ruptured surfaces of slowly deformed hydrogen embrittled materials, and (3) a delay in the on-set of cracking.

No single correlation exists on quantity of absorbed hydrogen required to cause serious damage. Factors are: steel type, thermal treatment, physical properties and welding conditions [Ref. 5].

For all these reasons [Ref. 1], industry limits wet welding base metal carbon equivalent (CE) to less than 0.40 wt %. If higher CE steels are to be welded, then non-ferritic (austenitic) electrodes should be used. This is because the austenitic electrodes have three properties which can reduce the danger of hydrogen induced underbead cracking.[Ref. 14] First, the austenitic weld metal has a higher solubility then α-ferrite of hydrogen, therefore, less hydrogen is diffused into the HAZ of the base metal. Second, the austenitic weld metal is more ductile, therefore, the build up of excessively high residual stresses in the HAZ is prevented. Finally, the thermal expansion coefficient of the austenitic weld metal is different from the base metal, this can reduce the thermal stresses on cooling down, however, for high temperature applications this can effect the joint design.

1. Material Selection

The *Specification for Underwater Welding* [Ref. 1] lists requirements for base metals. Both carbon content and carbon equivalent are listed as essential variables for wet welding. The carbon equivalent is a convenient measure of how sensitive the base metal is to hydrogen cracking [Ref. 14]. The carbon equivalent for underwater welding is specified as [Ref. 1]:

$$CE = C + \left(\frac{Mn}{6}\right) + \left(\frac{(Cr + V + Mo)}{5}\right) + \left(\frac{(Cu + Ni)}{15}\right) \tag{2.1}$$

$CE = Carbon\ Equivalent$

$C = Weight\ \%\ Carbon$

$Mn = Weight\ \%\ Manganese$

$Cr = Weight\ \%\ Chromium$

$V = Weight\ \%\ Vanadium$

$Mo = Weight\ \%\ Molybdenum$

$Cu = Weight\ \%\ Copper$

$Ni = Weight\ \%\ Nickel$

It is better to have the material selected for the welding procedure qualification to be as close as possible to that of the actual base metals carbon equivalent; however, in no case may the carbon content of the material used for the procedure qualification be less then the actual base metals.

While fundamental studies were conducted into wet welding carbon equivalent vs. hydrogen cracking during the Seventies [Ref. 22, 23, 24 and 25], Grubbs, et al. [Ref. 22] found that hydrogen cracking was a minor problem unless 0.4 CE was exceeded. This has become the industry accepted limit. However, Masubuchi, et al. [Ref. 23] reported in 1977 that other studies indicate that hydrogen cracking can occur in steels with a 0.3 → 0.42 CE [Ref. 26]. The material selected for qualification (ASTM A 516 Gr 70) for underwater welding is toward the upper end of the limit with 0.40 CE and a 0.2 wt% carbon content. Thus, as can be seen on a Graville diagram [Ref. 27], Figure 2.3, this may not be easy to weld, even in air. The Graville diagram should perhaps be modified to reflect those comments by moving the zone II-III line toward the left at least 0.1 CE.

2. Rapid Cooling Rate

The cooling rate for welds affects the weld metal phase transformations and the resulting microstructure. A continuous cooling transformation (CCT) diagram can be used to explain the weld microstructure. Figure 2.4 is a welding CCT diagram for the coarse-grained HAZ (CGHAZ) region of A516 Gr 70 steel showing regions of martensite (M), bainite (B), ferrite (F) and pearlite (P).

As discussed by Lundin, et al., the weld metal heat affected zone can be described as four general regions [Ref. 28]:

Coarse-grained HAZ (CGHAZ)	>1100°C
Fine-grained HAZ (FGHAZ)	AC_3 - 1100°C
Intercritical HAZ (ICHAZ)	AC_1 - AC_3
Subcritical HAZ (SCHAZ)	$<AC_1$

Figure 2.5 is a cross section view of a single pass weld showing the four microstructural regions corresponding to the critical temperatures and the equilibrium diagram. During multipass welds, the HAZ can become more complex since the areas are further altered [Ref. 28].

Figure 2.6 shows the alteration of the HAZ in a multipass weld. The cooling rate is the most important factor controlling the microstructure, the resulting fracture toughness and the microhardness. As can be seen from Figure 2.4, as the weld heat input is increased, the cooling rate is lower and the hardness is lower.

While the above research was not for wet welding. Ibarra, et al. [Ref. 29] noted that the time to cool from 800°C to 500°C (Δt8/5) for surface (air) SMA welds was from 8 to 16 seconds, while for wet SMA welds it was from 1 to 6 seconds. This can be seen in Figure 2.7. The result is that almost all mild steel wet welds will have coarse-grained HAZs that are martensitic.

Tsai, et al. [Ref. 25] studied the mechanism of rapid cooling and its effect on the HAZ near the fusion zone. The effect of the welding parameters, plate thickness and water temperature were considered. Their numerical analysis shows only a minor change in the cooling rate in the HAZ with respect to changes in water temperature. Figure 2.8 shows the effect on the peak temperature. Tsai recommended further studies into this subject beyond their simple treatment of this issue as a boundary heat loss problem.

3. Hydrogen Cracking

As the martensite content increases near the fusion line in the CGHAZ, the weld is more susceptible to hydrogen cracking. Surface welds of high strength steels use a careful selection of welding consumables to limit diffusible hydrogen levels.

There are generally four conditions present simultaneously for hydrogen cracking to occur [Ref. 14, 5 and 29]:

1) Susceptible microstructure
2) Critical concentration of diffusible hydrogen
3) Stress intensity
4) Relatively low temperature less than 200°C (400°F)

These conditions are easily met in underwater wet welding. First, the susceptible microstructure is martensite which is normally a result of the high cooling rate already discussed. Second, the wet welding environment has a high content of water vapor in the plasma column. This water vapor will dissociate into hydrogen and oxygen [Ref. 29]:

$$H_2O_{(v)} \rightarrow H_{2(g)} + \frac{1}{2}O_{2(g)} \tag{2.2}$$

This hydrogen and oxygen will raise the hydrogen and oxygen contents of the weld metal. The hydrogen will then diffuse into the austenite of the CGHAZ. This is because hydrogen has a lower solubility ferrite (α) than in austenite (γ). Figure 2.9 indicates how hydrogen diffuses from the plasma to the weld metal, then into the CGHAZ. The hydrogen is then trapped in the CGHAZ since the diffusion coefficient is much lower in austenite than in ferrite. Then the fusion line austenite transforms into martensite and two of the four conditions have been met. A study of hydrogen-induced cracking by Savage, et al., [Ref. 30] observed that initially the liquid films along the grain boundaries of the partially melted zone acted as a flow path from weld metal into the CGHAZ. When this area resolidifies, the hydrogen is trapped and the result is preferred nucleation sites for intergranular cracking. The *Metals Handbook* [Ref. 5] indicates that hydrogen-induced cracking is generally transgranular. So the exact mechanism of hydrogen cracking in the partially melted zone and the CGHAZ is not completely established. Third, the high stress in the weld can result from weld joint design. The joint may be restrained resulting in tensile stresses upon cooling. The degree of restraint is further affected by the differences in thermal and volumetric expansion coefficient for the weld metal and base metal. The resultant stresses interact with hydrogen concentrations at existing discontinuities to produce cracking. Finally, the water environment will ensure the relatively low temperature of the weld.

D. THE FUSION ZONE MICROSTRUCTURE OF UNDERWATER WET WELDS

1. Fusion Zone Grain Structure

Underwater wet welding of mild steels results in the weld metal having three basic structures of ferrite, bainite and martensite. The solidification process has grains growing in a dendrite or columnar dendrite fashion from the fusion boundary toward the weld pool centerline. The growth direction is that of the maximum temperature gradient and the growth is competitive. Since the grains, which are growing parallel to the temperature gradient and have a <100> orientation, will crowd out the other grains [Ref. 14].

Figure 2.10 shows the competitive growth in the fusion zone. The welding parameters affect the columnar-grain structure since, as the weld pool changes shape, the columnar grains still grow perpendicular to the weld pool surface. Figure 2.11 shows the different columnar grain structure between a high and low welding speed. The resultant columnar grain structure could result in grain abutment which is poor and can lead to center line solidification cracking. The columnar grains can be controlled by nucleation of new grains in the weld metal.

Kou [Ref. 14] discusses four mechanisms of grain nucleation: surface nucleation, dendrite fragmentation, grain detachment and heterogeneous nucleation. Figure 2.12 shows the four mechanisms of nucleation in a weld pool. First, the surface cooling mechanism is always present in wet welding. The surface is water quenched after the covering gas bubble collapses. When this occurs, solid nuclei can form on the weld surface and they then act as nucleation points within the weld pool as they shower down from the surface. Second, dendrite fragmentation occurs when the weld pool convection breaks off a dendrite fragment from the mushy zone. It is then carried into the weld pool and may act as a nucleation site for new grain formation. This is referred to as a grain refining mechanism for weld metals. Third, grain detachment again occurs due to weld pool convection. However, this time, the grains come from the partially melted zone from the weld metal at the leading edge. Finally, classical nucleation theory in a liquid requires that a critical energy barrier be overcome to form a nuclei of a critical radius.

The equation for total free energy in homogenous nucleation [Ref. 31 and 21] is:

$$\Delta G = \Delta G_v + \Delta G_s \tag{2.3}$$

Where,

ΔG_v = bulk or chemical-free energy

ΔG_s = surface energy of solid-liquid interface

$$\Delta G = \left(-4\pi r^3 \Delta G_v / 3\right) + 4\pi r^2 \gamma \tag{2.4}$$

Where, for a spherical nucleus

$r =$ nucleus radius

$\gamma =$ surface free energy of unit area

When the above equation is differentiated and set equal to zero, the critical radius is found:

$$\frac{d\Delta G}{dr} = -4\pi\Delta G_v + 8\pi r\gamma = 0 \tag{2.5}$$

resulting in:

$$r^* = \frac{-2\gamma}{\Delta G_v} \tag{2.6}$$

From this critical radius, the energy required to form a stable nucleus is found:

$$\Delta G^* = \frac{16\pi\gamma^3}{3(\Delta G_\gamma)^2} \tag{2.7}$$

The above critical energy barrier $\left(\Delta G^*\right)$ is usually high and difficult to overcome. However, if the weld pool has a significant number of foreign solid particles, then nucleation may be easier at that surface. Figure 2.13 shows formation of equiaxed dendrite grains from heterogeneous nucleation. Research [Ref. 14] has found that welding parameters affect heterogeneous nucleation of equiaxed grains. Higher heat inputs and welding speeds have been found to enhance the heterogeneous nucleation. As the heat input is raised, the temperature gradient (G) of the weld pool is lowered. As the welding speed is raised, the solidification rate (R) is also raised. Therefore, the G and R ratio will be lower and the mode of solidification will tend to be equiaxed. This follows the constitutional supercooling theory [Ref. 14]. Figure 2.14 shows the affect of temperature gradient (G) and solidification rate (R) on the mode of solidification. Furthermore, the cooling rate which is the product of G/R will determine the fineness of the resulting microstructure. Therefore, a wet weld will have a finer microstructure as a result of the small austenite grain sizes.

There are three morphologies of ferrite which develop in weld metals [Ref. 29 and 14]:

* Allotriomorphs which are chunky ferrite particles which form at the grain boundaries. This is normally called grain boundary ferrite (GBF).

* Widmanstatten plates (named after the man who first discovered them) growing from grain boundaries are normally called side plate ferrite (SPF).

* Acicular ferrite (AF) is formed intragranularly. Therefore, it has a fine basket-weave structure than SPF.

The weld metal microstructure can also have other microconstituents such as bainite and martensite. As the cooling rate raises, the amount of ferrites will be lower and more bainitic aligned carbides (sometimes called ferrite with aligned second phases) and martensite will result [Ref. 29]. Kluken, et al. [Ref. 32] concluded that the controlling factor with respect to acicular ferrite formation is the orientation with respect to the austenite and the prior δ-ferrite columnar grain in which it grows. This orientation falls within the bain distortion and follows a Kurdjumov-Sachs relationship.

The acicular ferrite grows parallel to the original dendrite growth of the austenite grain. The fine lath growth of acicular ferrite into the austenite is separated by high angle boundaries. This morphology is like that of upper bainite. Thus, the growth of acicular ferrite is closely related to the mechanism of upper bainite and it seems that AF is just like bainite nucleated intragranularly on non-metallic inclusions. Acicular ferrite has been shown to be the microstructural constituent that is responsible for higher weld metal toughness in low carbon structural steel welds [Ref. 14 and 29]. In closing, the microstructures to be avoided are those with a high percentage of GBF or martensite and the desired microstructure is one with a high percentage of acicular ferrite.

In the next few sections, discussion will turn to the way underwater wet welds are affected by environmental changes, consumables and welding parameters with respect to inclusion and microstructural characteristics.

2. Environmental Effects

While it has been stated that a weld must have a strong microstructure, the question of how it can be achieved must always be kept in mind. The environmental effects of water, salinity and pressure all change the weld metal chemistry and microstructure.

a. Water

The water environment will result in a much higher cooling rate. While this paper has already discussed that effect on the HAZ, now the influence of the cooling rate on the fusion zone microstructure will be examined.

Again the most useful tool to examine this influence is the continuous cooling transformation (CCT) diagram. Figure 2.15 shows the effect of cooling rate. The low cooling rate curve intersects the acicular ferrite curve. This is obtained by using a higher heat input as discussed above [Ref. 29]. As illustrated in Figure 2.15, as the cooling rate increases there is a higher propensity for bainite and martensite formation at the expense of acicular ferrite. This will be discussed again in the Results and Discussion section. In studies of the mechanism of cooling, Tsai, et al. [Ref. 25 and 28] found that various insulation methods can have a positive effect on cooling rates. Furthermore, they noted that the effect of water temperature on the cooling rate was small [Ref. 28].

b. *Salinity*

Seawater tends to produce smoother arcs than fresh water. This is possibly due to the influence of ions which result from the dissociation of salts in the seawater. The extra ions lead to more charge carriers which result in a smoother, more stable arc [Ref. 5].

The effect of salinity was found by Kononenko [Ref. 33] to lower weld metal hydrogen content while it raised the oxygen content. That is to say that in comparison to freshwater, as the salinity increases the hydrogen levels will be lower, but they will still be much higher then that of surface welds. This appears to be a result of the dissociation of salts (potassium, sodium, magnesium and calcium) in the seawater which were dissociated into the arc. That dissociation caused a higher heating and, therefore, high oxidation in the weld metal droplets thus resulting in lower hydrogen solubility in the weld metal.

c. *Pressure*

Hyperbaric effects tend to constrict the arc and the large heat sink of the water leads to elevated arc core temperatures. These result in an increased weld penetration on higher rate of filler metal transfer. Because of arc construction, voltage and current, settings increase with water depth [Ref. 5]. Christensen, et al. [Ref. 34 and 35] have shown the adverse effects that underwater welding has on weld metal manganese and silicon contents. Figure 2.16 shows the effect of water depth on alloying elements. While the manganese and silicon contents decrease, the oxygen and carbon contents increase. These changes can result in considerable changes in weld metal hardenability and reduced toughness [Ref. 29, 34 and 36]. Figure 2.17 shows the influence of oxygen and manganese contents on the weld metal CCT diagram.

Ibarra, et al. [Ref. 29, 32, 33 and 35] have studied the chemical compositions of underwater wet SMA welds as a function of water depth. The manganese and silicon contents decrease in direct relationship to the oxygen increase. As noted above and seen in Figure 2.18, Grong, et al. [Ref. 35] found that, for hyperbaric welds, there exists a linear relationship between the product of oxygen [O] and carbon [C] and total pressure down to about 300 meters. This means that the [C][O] reaction is controlling and care should be taken in using carbonite fluxes. Ibarra, et al. [Ref. 29] plotted this effect for wet welding (Figure 2.19) and found that CO controls initially and then a hydrogen-oxygen product takes over at greater depths.

At greater depths, the effect of Ibarra, et al's., findings seem to indicate that, after about 50 meters, depth carbon monoxide no longer controls the weld metal manganese and silicon levels. Since the present study is for shallow depth where ship repairs take place, further theories will not be discussed in detail. Both Ibarra, et al. [Ref. 29] and Pope, et al. [Ref. 19] have alternate interpretations of the plateau seen in Figure 2.19. Whereas Ibarra, et al., describe this as a [H][O] controlling process, Pope, et al., contend that the oxygen saturation content in FeO is the cause. Their model is supported by the presence of FeO dendrites formed on inclusions.

The combined effect of depth (pressure) and dissociation of water result in increased porosity in wet welds [Ref. 29]. Porosity is the most common defect and is of great concern. The gas content was reported to contain approximately 96% by volume of hydrogen. In wet welding near the surface, porosity was up to 5%. This value increased to nearly 20% at 90 meters depth.

3. Alloying and Consumable Effects

Recently there has been a great deal of work done on welding consumable electrodes [Ref. 2, 33, 18, 19, 21 and 37]. Commercial welding electrodes have not been found to provide weldments of the high quality requirement shown in AWS D-3.6. For the most part, these electrodes are not designed for underwater welding and only have an additional waterproofing treatment to limit excess moisture in the flux [Ref. 21]. Industry has used a variety of techniques to limit excess moisture ranging from heating followed by paint, resin, etc. to keeping them in a holding oven [Ref. 21]. in the early Seventies, Silva et al. [Ref. 16] found that iron powder electrodes yielded better quality welds. Now, with changes in specifications, there has been increased research into consumable fluxes in an attempt to reduce hydrogen levels and promote a strong, tough microstructure.

Electrodes for underwater welding are generally ferritic filler metals for carbon equivalent less than 0.4. However, if the weld depth is at greater than 100 meters, austenitic or nickel filler metals are used since these have a higher hydrogen solubility and more ductility. Therefore, the resulting weldment will be less susceptible to hydrogen-assisted cracking.

a. Oh, et al. [Ref. 38] have reported that boron and titanium have shown great promise in promoting the formation of acicular ferrite in weld metal. Figure 2.20 shows the combined effect of boron and titanium in the weld metal on the volume fraction of acicular ferrite. The delicate balance of boron and titanium in the formation of proper size and distribution of inclusions which result in this high volume fraction of acicular ferrite will be discussed later.

Sanchez-Osio, et al. [Ref. 21 and 37] conducted a series of tests with different alloying elements to determine a better consumable mix for underwater wet welding. The following general relationships were found:

* Since titanium and boron are strong deoxidizers, they have a significant effect on weld metal oxygen content [Ref. 21, 37 and 38]. Figure 2.21 shows the effect of boron and titanium on weld metal oxygen levels in underwater wet welds. Notice that as boron and titanium levels increase, the oxygen content decreases as expected.

* As the titanium content of the weld metal increases, both manganese and silicon contents also increase (Figure 2.22). The increase in manganese content raises the weld metal hardenability, a desirable effect which could lead to more acicular ferrite formation. The increase in silicon content is undesirable for it reduces the weld metal toughness. However, when a plot of weld metal hardness versus boron and titanium is examined (Figure 2.23), it is seen that increases in boron also raise the hardness.

* Since a tough microstructure for the weld metal is desired, the lowest points of Figure 2.23 are of interest. Investigators [Ref. 21, 37 and 38] found that, in fact, there is a competing process with the additions of titanium and boron on the resulting microstructure. However, Sanchez-Osio, et al. reported that optimal ranges of titanium and boron were lower for underwater wet welds than for surface welds. This may be due to the higher cooling rate's effect on acicular ferrite content. Figure 2.24 shows volume fraction acicular ferrite as a function of boron and titanium. The optimal levels are about 15 ppm and 300 ppm, respectively. This can be compared to Figure 2.20 as reported by Oh, et al. for surface welds.

b. The effect of calcium carbonate ($CaCO_3$) additions have also been investigated [Ref. 21, 37, 21 and 18]. Sanchez-Osio, et al. reported that for small additions (<13 wt%) of $CaCO_3$, the porosity was reduced along with the weld metal hardness. These findings concurred with Chew's (1973) findings where additions of $CaCO_3$ reduced diffusible hydrogen content since porosity has been found to contain large amounts of H_2, CO and CO_2 gases [Ref. 21, 24 and 37].

Figure 2.25 shows the effect of $CaCO_3$ addition on porosity. While Figure 2.26 shows the effect of $CaCO_3$ on weld metal diffusible hydrogen levels. Note that Sanchez-Osio, et al. reported that when $CaCO_3$ wt% was raised to higher levels, arc instability actually increased porosity as seen in Figure 2.25. The combined effects of the carbon-oxygen and the hydrogen-oxygen reactions and the resultant impact on SMA electrode design was discussed by Liu, et al. [Ref. 21] who developed a methodology for estimating residual hydrogen content.

4. Non-Metallic Inclusions

Inclusion nucleation and growth is similar to the classical nucleation theory discussed above. Since the activation energy (ΔG^*) for homogeneous nucleation of oxide is large, Sanchez-Osio, et al. [Ref. 21] discussed the effect of supersaturation required to promote their growth. Furthermore, they repeated that the solidification time is short and dependent on the cooling rate during solidification ($\propto (GR)^{-1}$). Since the time for growth is less than surface welds, it should be expected that they would have a smaller average diameter. This is not the case and it has been observed [Ref. 21] that the weld metal oxygen content tends to raise the average inclusion size. This can be explained if the growth mechanism is assumed to be diffusion controlled and if the weld metals have a supersaturation of oxygen. The composition profiles for oxygen for a unidirection diffusion controlled growth of the inclusions are shown in Figure 2.27.

The inclusion growth rate is then described by:

$$\gamma = \frac{(C_o - C_e)}{2(C_\beta - C_e)}(\frac{D}{t})^{\frac{1}{2}} \tag{2.8}$$

C_o = Oxygen concentration of weld metal

C_e = Equilibrium oxygen concentration of solid-liquid interface

C_β = Oxygen concentration of inclusion

D = Diffusion coefficient

t = Time

Therefore, as oxygen content in the weld metal increases, the average size of the inclusions increase.

The effect of non-metallic inclusions on the weld metal are two fold. First, if they can be grown to the proper size with an appropriate chemical composition, they provide sites for heterogenous nucleation within the prior austenite grains for acicular ferrite. Second, they tend to pin the grain boundaries of austenitic grains and thereby limit their growth, resulting in a finer and tougher microstructure of the weld metal. This can be seen in Figure 2.28, a schematic representation of the effect of inclusion size on austenite grain size and acicular ferrite formation.

E. SCOPE OF THE PRESENT WORK

The Office of the Director of Ocean Engineering, Supervisor of Salvage and Diving (NAVSEA OOC) and Naval Postgraduate School are investigating the results of water temperature on the failure of underwater wet welding procedure qualification programs using ASTM A516 Gr 70 steel. Since the *Specification for Underwater Welding* [Ref. 1] has omitted the water temperature from being considered an essential variable, its variation was not considered. However, when Puget Sound Naval Shipyard attempted the qualification at a lower water temperature (2.8°C), what appeared to be hydrogen induced cracking occurred in the CGHAZ of the welds they made on A516 Gr 70 steel. The ultimate objective of this research is: (1) to determine the cause and the mechanism of the cracking, and (2) to determine the influence of water temperature on the weld metal and HAZ cracking in underwater wet welds in steels at the current upper limit of the carbon equivalent and carbon content. The approach toward achieving the objective is detailed in the five subtasks listed below:

* Subtask A: Metallurgical Analysis of Cracking - Samples from the existing cracked weldments and existing lab reports will be evaluated. Evaluation will be sufficient to determine the mechanism of cracking.

* Subtask B: Literature Reviews - Reviews of the following topics:

1) The influence of water temperature on cracking in wet welds.

2) Diffusible hydrogen levels in wet welds and the influence of water temperature on these levels. The goal is to locate data, information on measurement techniques and any models that could be used to predict diffusible hydrogen levels in wet welds.

3) Cooling rates in wet welds and the influence of water temperature on these rates. The goal is to locate data, information on measuring techniques and any models that could be used to predict cooling rates in wet welds.

4) The influence of depth (approx. 45') and welding position on hydrogen content and cooling rate.

* Subtask C: Diffusible Hydrogen in Wet Welds - Determine diffusible hydrogen levels for the electrodes and wet welding conditions of interest. Procedures will be developed to measure diffusible hydrogen levels in the wet welds. These procedures will be used to make measurements on the weld deposited at different water temperatures, welding position and depth. In addition to the experimental work, applicable models identified in Subtask B will be used to predict diffusible hydrogen levels (and the influence of water temperature).

*Subtask D: Cooling Rates in Wet Welds - Determine cooling rates for wet welding conditions of interest. Procedures will be developed to measure cooling rates during wet welding in different positions and depth. These procedures will be used to make measurements on welds deposited at different water temperatures. In addition to the experimental work, applicable expressions identified in Subtask B will be used to predict cooling rates (and influence of water temperature).

* Subtask E: Effect of Water Temperature on Cracking - If warranted by the results of Subtasks A through D, cracking tests will be conducted to determine the influence of changing water temperature from approximately 10°C to approximately 25°C on cracking susceptibility.

This study involves subtask A and B. The initial review of the existing weld samples and laboratory reports was conducted and further evaluations were conducted by optical microscopy, microhardness and scanning electron microscopy to determine the mechanism of cracking. A literature review was conducted to determine if the influence of water temperature on wet welding cooling rate, diffusible hydrogen levels and cracking had been studied in detail. Follow-on studies should address the other subtasks and will include modeling of underwater wet welding and, if warranted, more testing to prove the models and mitigate the cracking problems.

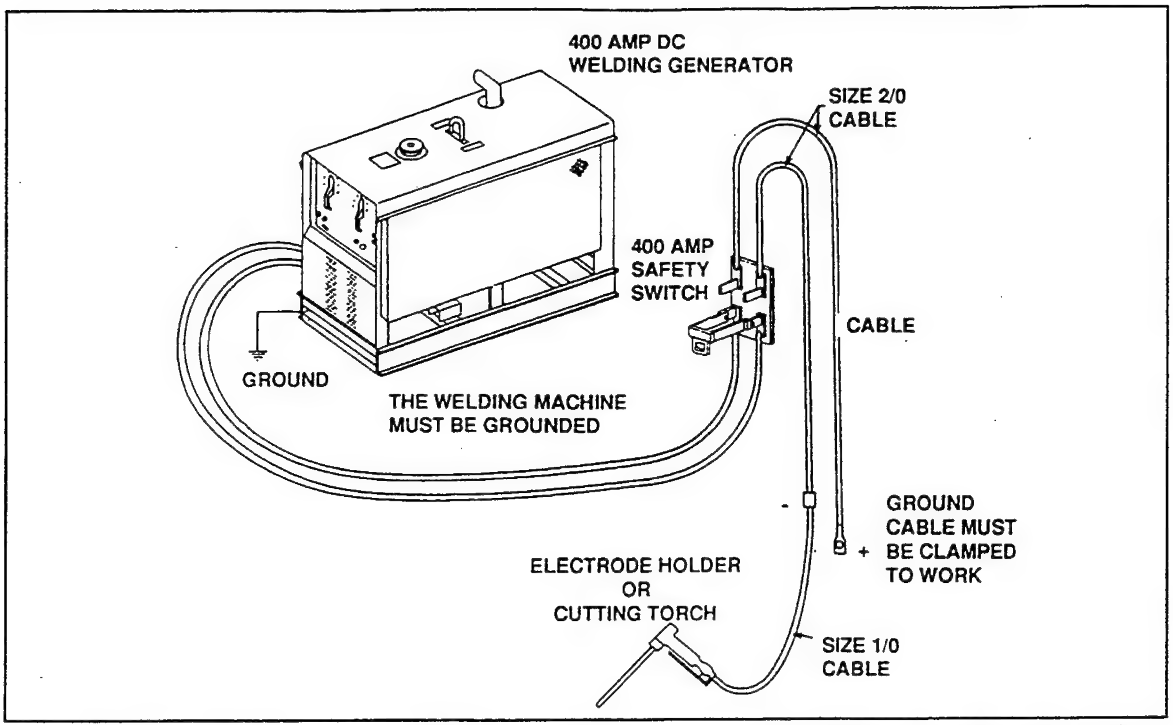
400 AMP DC
WELDING GENERATOR
SIZE 2/0
CABLE
400 AMP
SAFETY
SWITCH
CABLE
GROUND
THE WELDING MACHINE
MUST BE GROUNDED
-
+
GROUND
CABLE MUST
BE CLAMPED
TO WORK
ELECTRODE HOLDER
OR
CUTTING TORCH
SIZE 1/0
CABLE

Figure 2.1 Sketch of the welding and safety equipment configuration for Underwater welding and cutting. [Ref. 13]

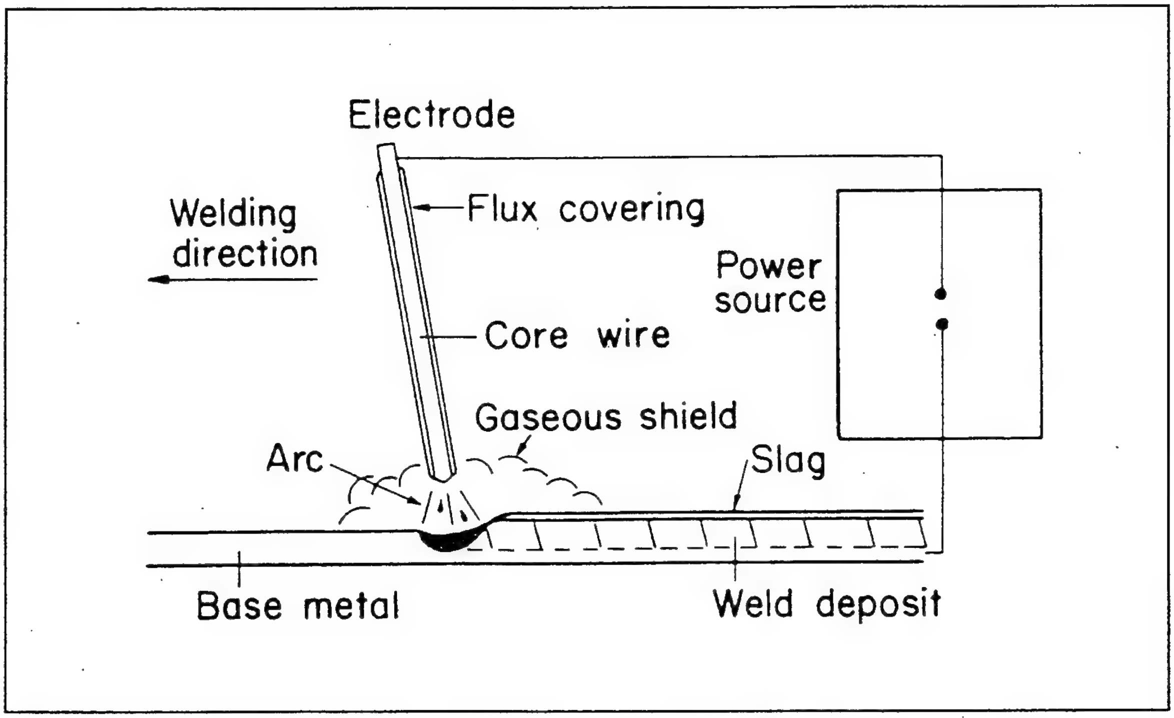
Electrode
Welding
direction
Flux covering
Power
source
Core wire
Gaseous shield
Arc
Slag
Base metal
Weld deposit

Figure 2.2 Sketch of the shielded metal arc welding process. [Ref. 14]

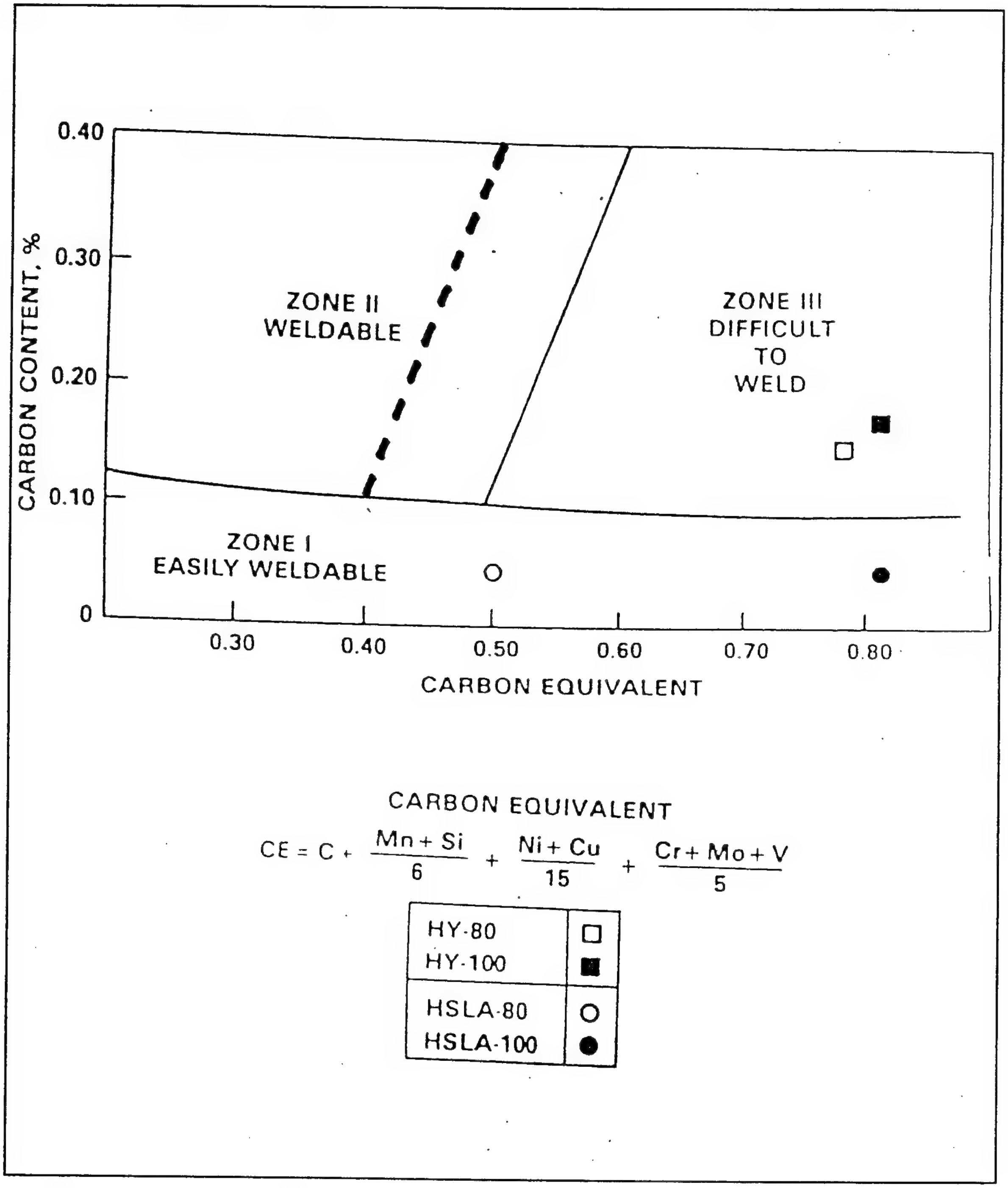

$$CE = C + \frac{Mn + Si}{6} + \frac{Ni + Cu}{15} + \frac{Cr + Mo + V}{5}$$

Figure 2. 3 Graville Diagram. The dashed line shows the suggested modification to the boundary between Zone II and III for underwater wet welding. [Ref. 27]

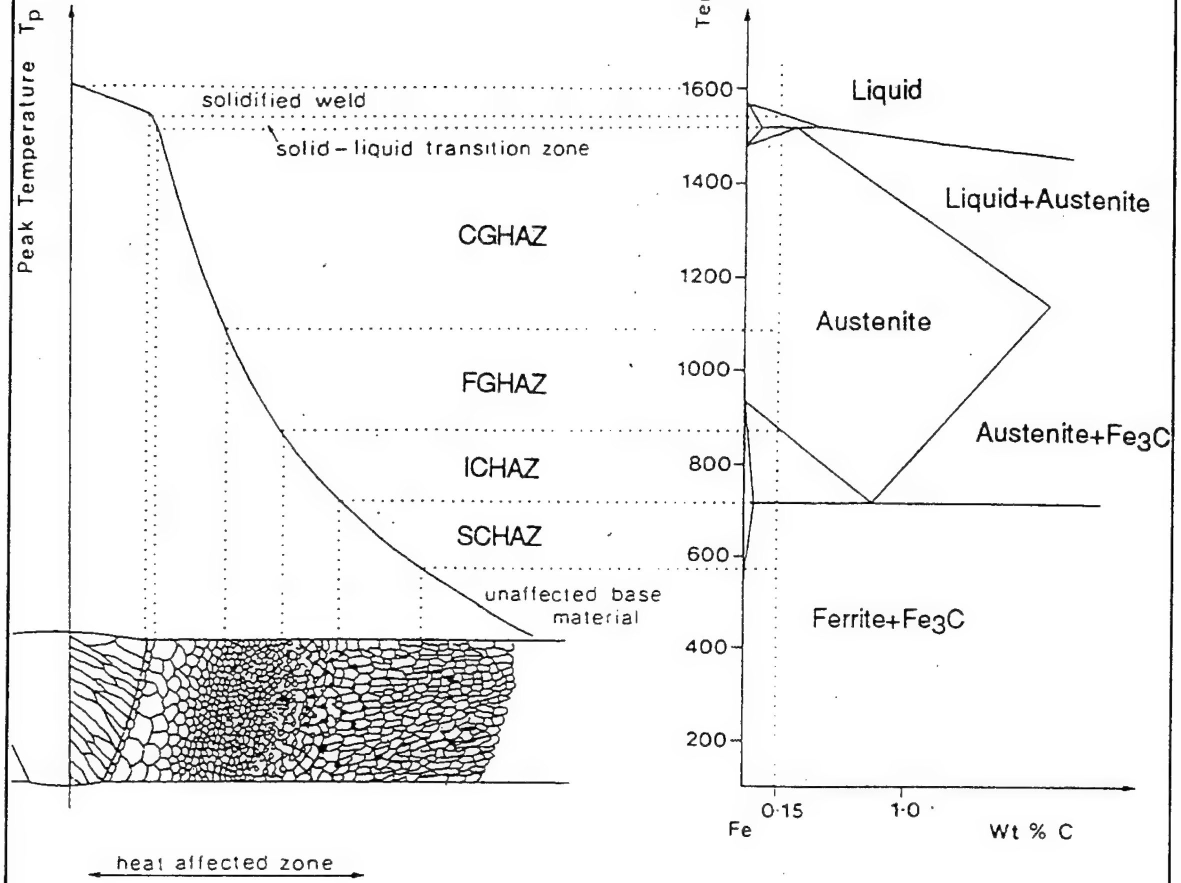
Peak Temperature Tp
solidified weld
solid – liquid transition zone
CGHAZ
FGHAZ
ICHAZ
SCHAZ
unaffected base material
heat affected zone
Temp °C
1600
1400
1200
1000
800
600
400
200
Liquid
Liquid+Austenite
Austenite
Austenite+Fe3C
Ferrite+Fe3C
Fe
0·15
1·0
Wt % C

Figure 2.4 Welding CCT diagram for A516 Gr 70 steel of simulated CGHAZ with 1320°C peak temperature and 25°C preheat for 2.5 cm thick plate. [Ref. 28]

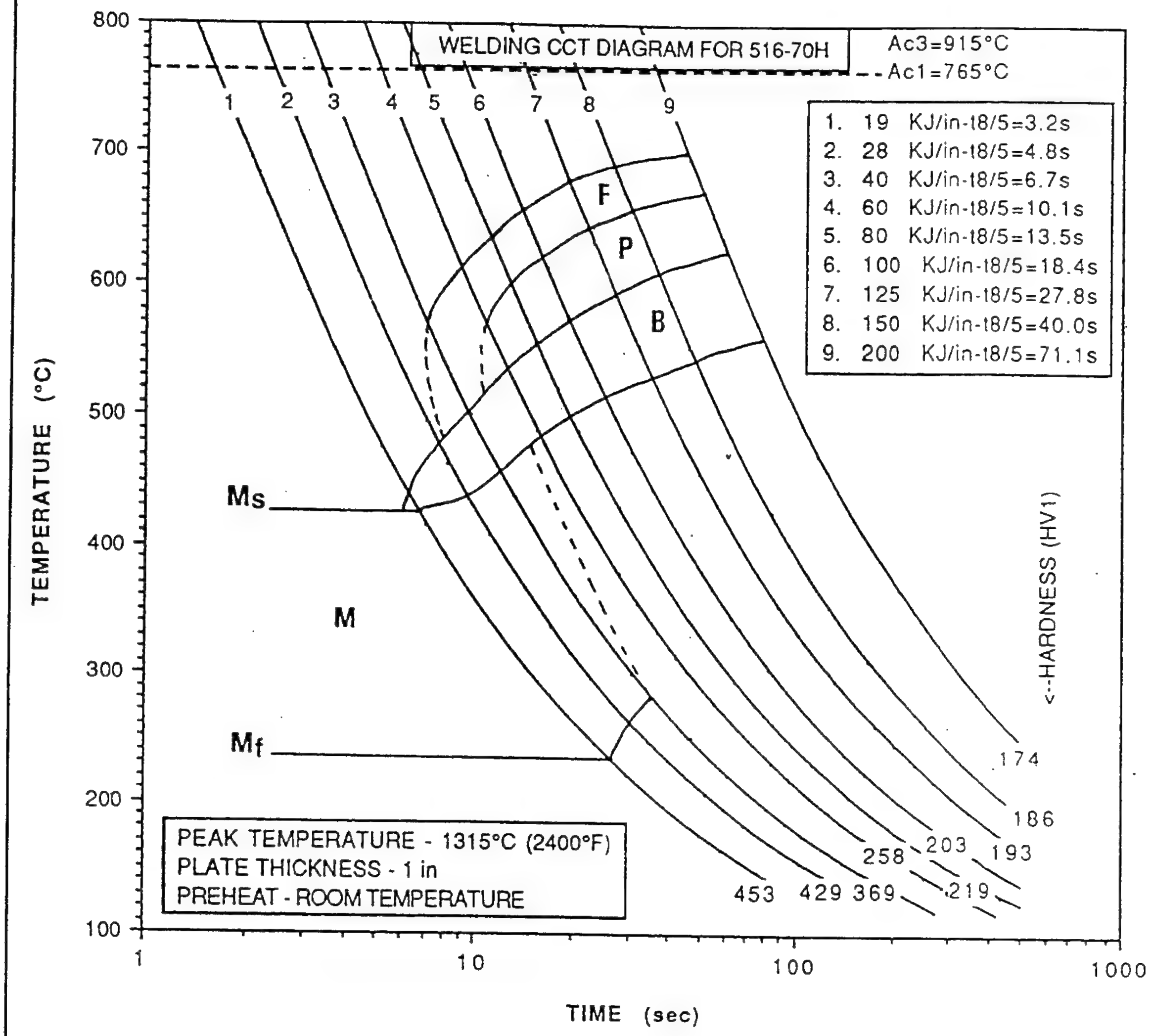

Figure 2.5 A schematic diagram of the various HAZ regions approximately corresponding to those indicated on the Fe-Fe$_3$C equilibrium diagram for a single pass weld. [Ref. 28]

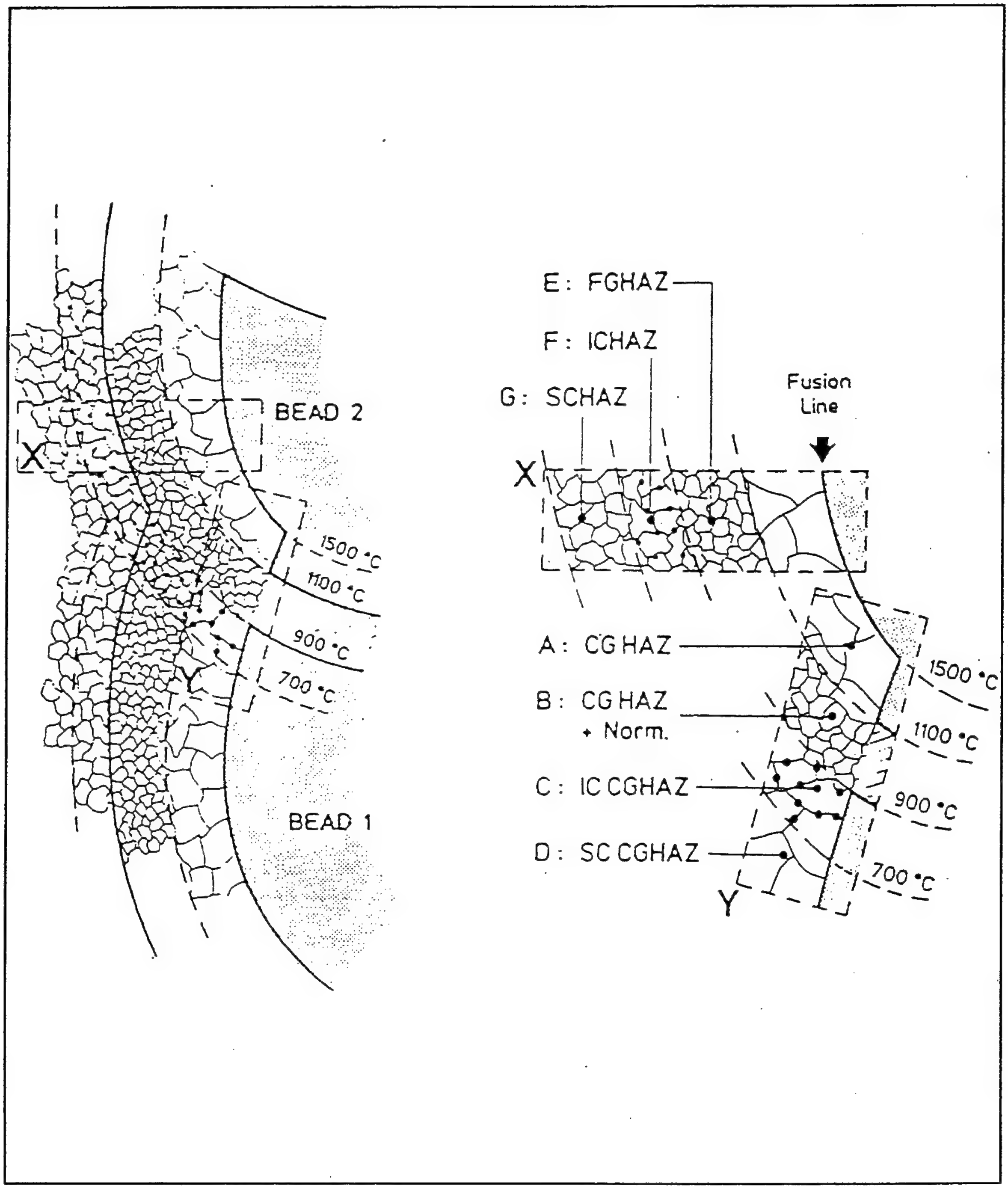
BEAD 2
BEAD 1
X
Y
1500 °C
1100 °C
900 °C
700 °C
E : FGHAZ
F : ICHAZ
G : SCHAZ
Fusion Line
A : CG HAZ
B : CG HAZ + Norm.
C : IC CGHAZ
D : SC CGHAZ

Figure 2.6 A schematic diagram of multipass weld HAZ Microstructure. [Ref. 28]

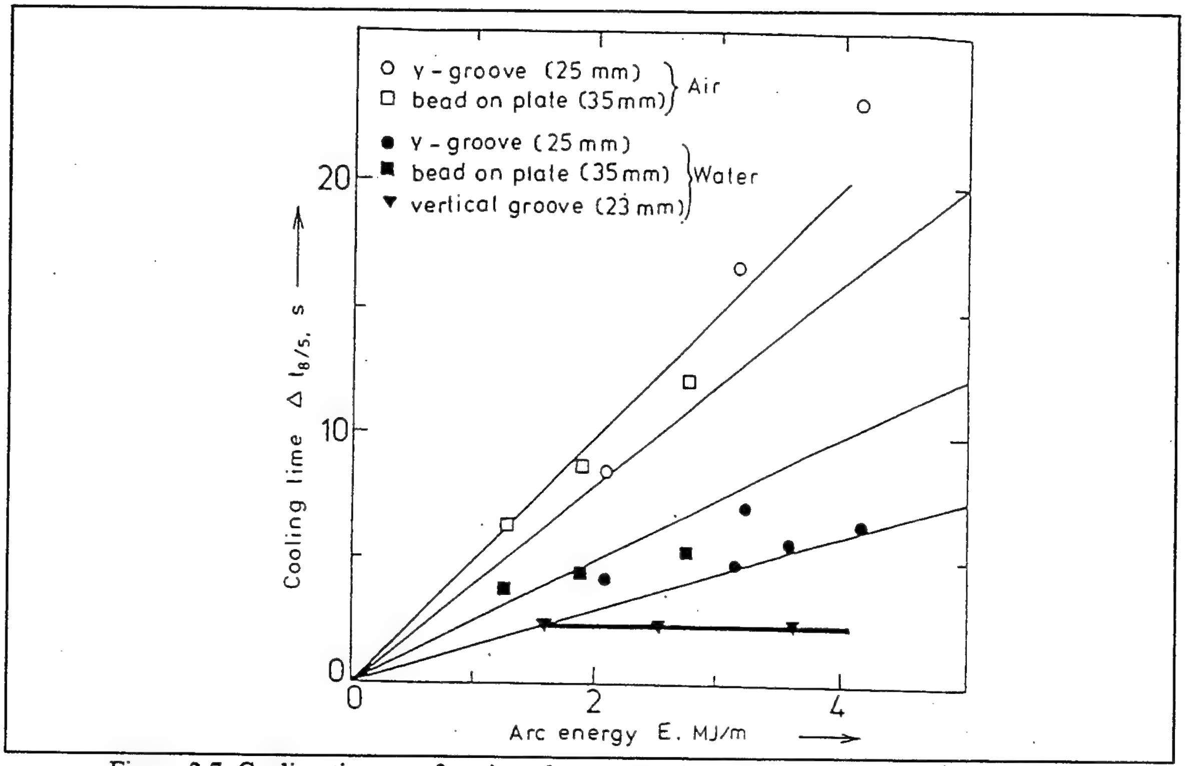

Figure 2.7 Cooling time as a function of arc energy for surface and underwater welding. [Ref. 29]

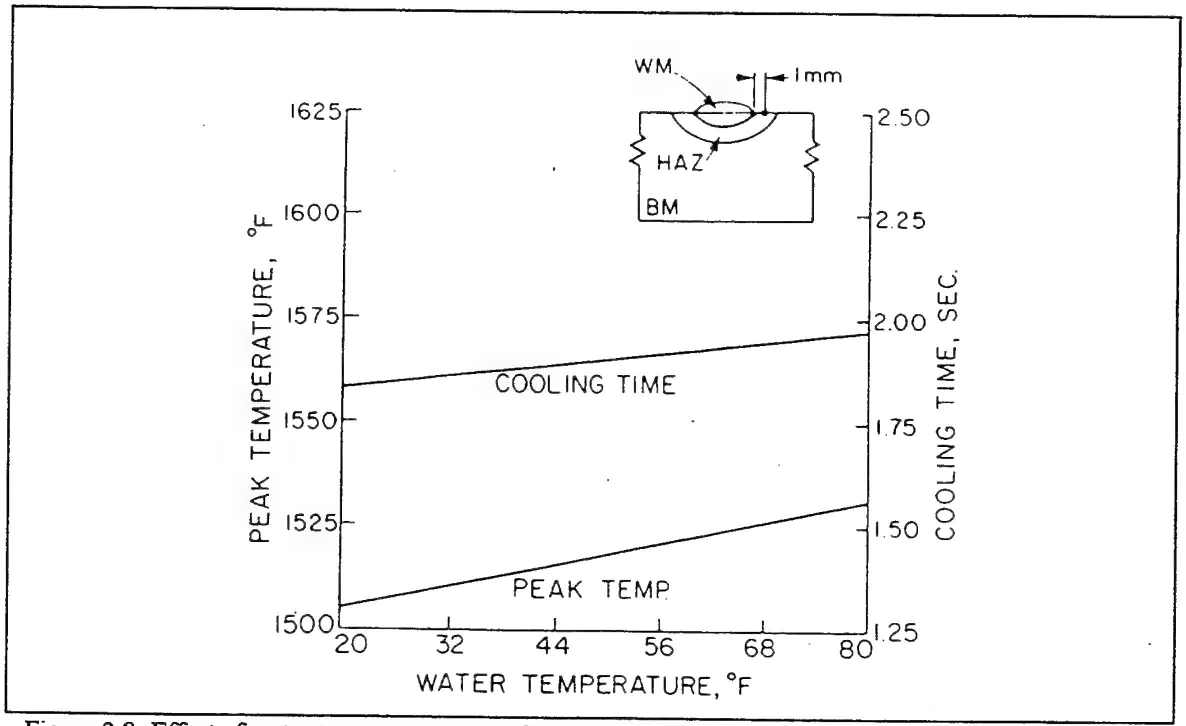

Figure 2.8 Effect of water temperature on peak temperature and cooling rate (800°C-500°C) at a point 1 mm distant from the fusion line on the plate surface. [Ref. 25]

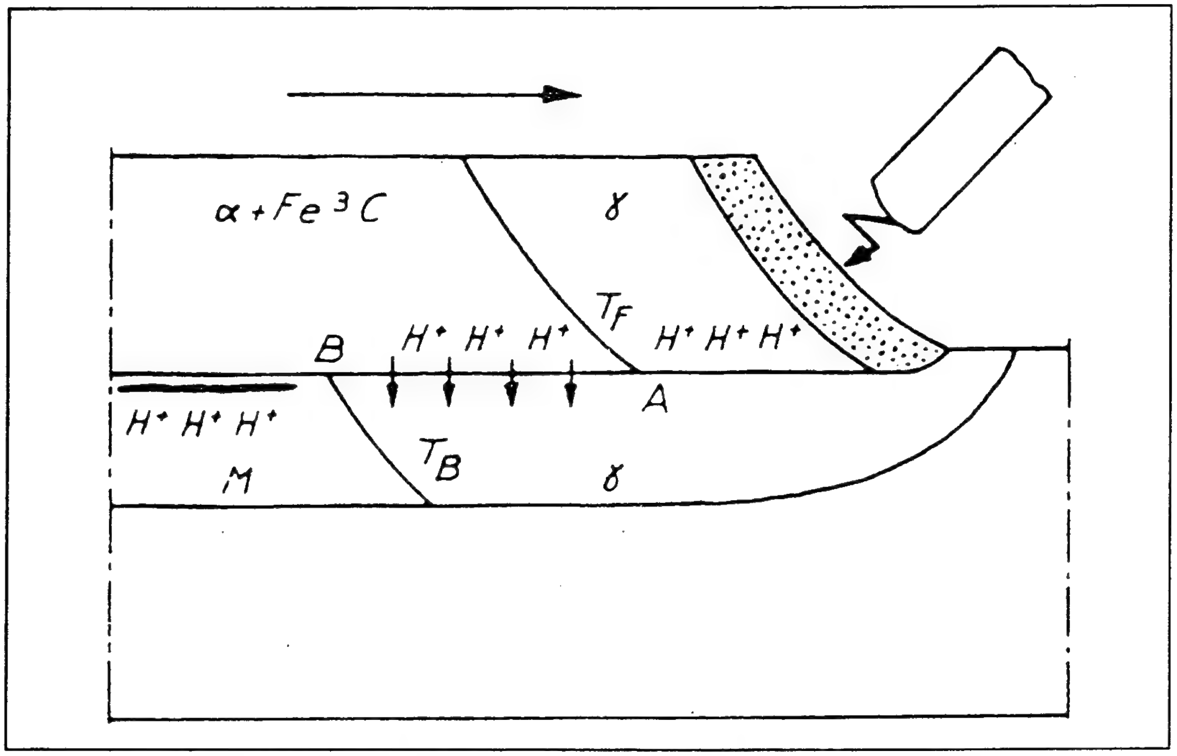
α + Fe 3 C
γ
T_F
B
H⁺ H⁺ H⁺
H⁺ H⁺ H⁺
A
H⁺ H⁺ H⁺
M
T_B
γ

Figure 2.9 Diffusion of hydrogen from weld metal to HAZ during welding. T_f and T_B are the $\gamma/(\alpha+P)$ and γ/M transformation temperatures. [Ref. 14]

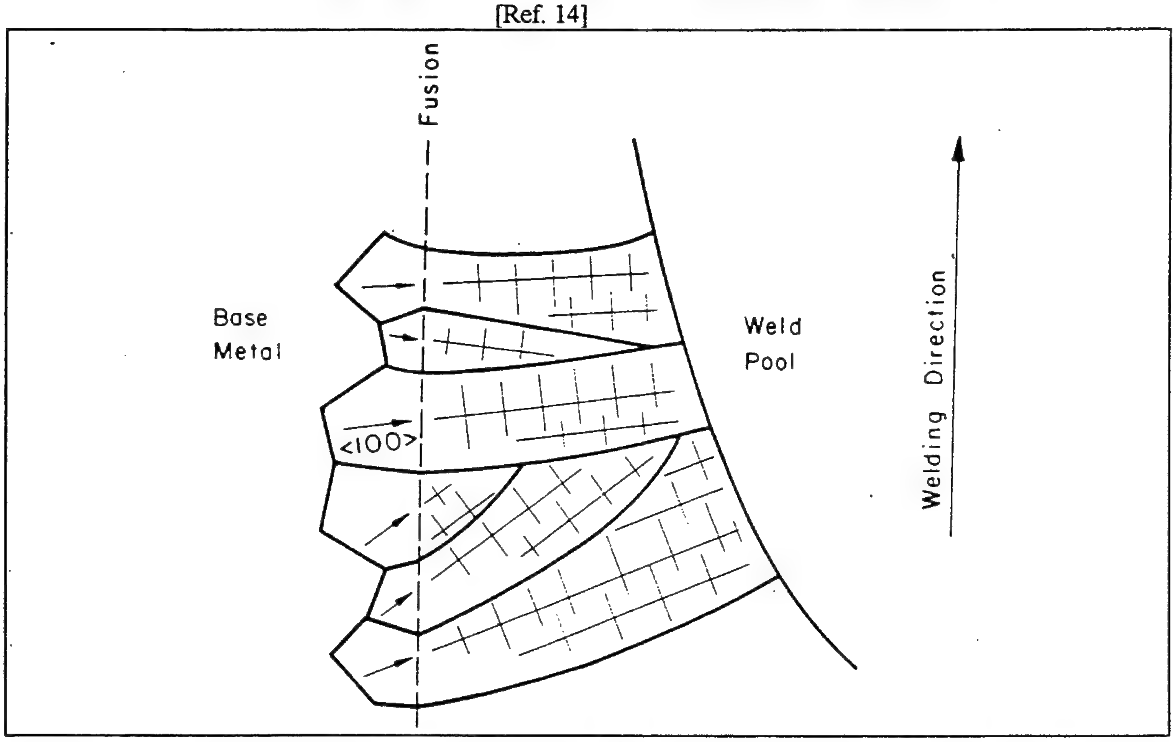
Fusion
Base
Metal
Weld
Pool
<100>
Welding Direction

Figure 2.10 Competitive growth in the fusion zone. The arrows in the grains of the base metal indicate the easy growth direction of <100> in metals. [Ref. 14]

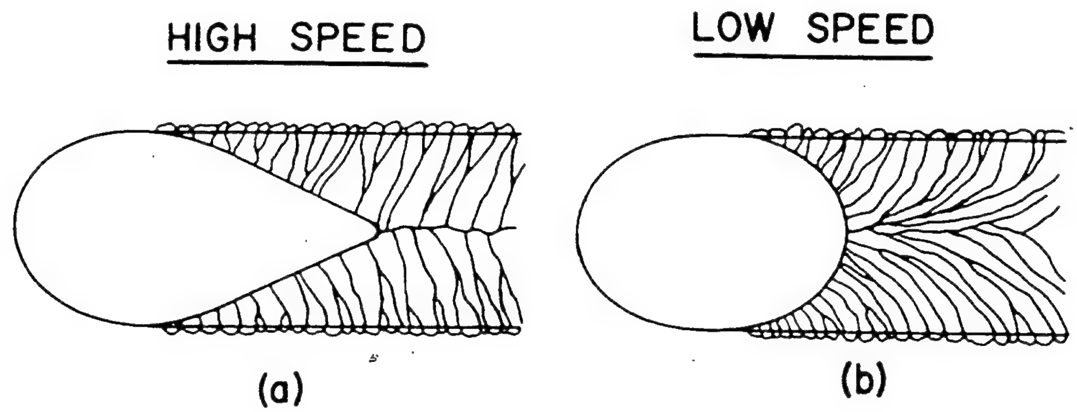
HIGH SPEED
LOW SPEED
(a)
(b)

Figure 2.11 Columnar-grain structure at high (a) and low (b) and welding speeds. [Ref. 14]

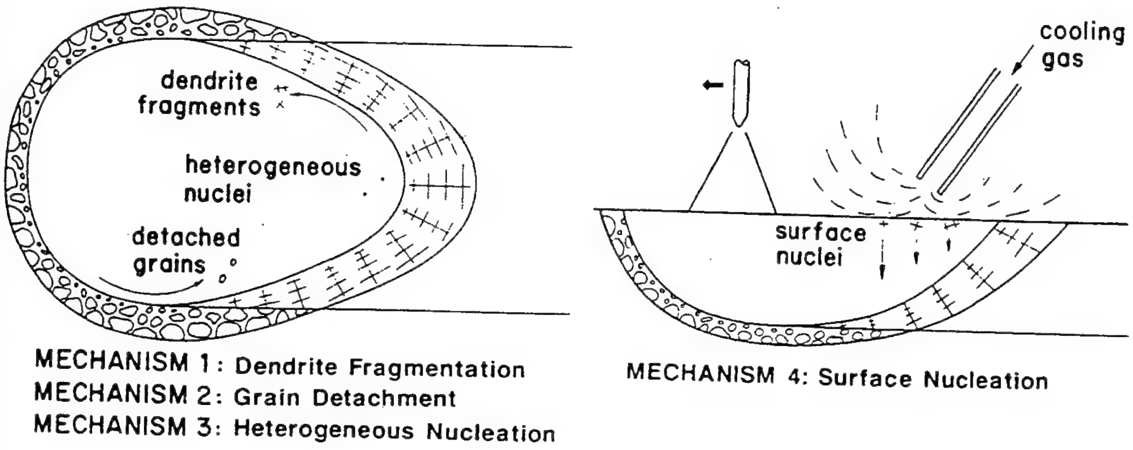
dendrite fragments
heterogeneous nuclei
detached grains
MECHANISM 1 : Dendrite Fragmentation
MECHANISM 2 : Grain Detachment
MECHANISM 3 : Heterogeneous Nucleation
cooling gas
surface nuclei
MECHANISM 4: Surface Nucleation

Figure 2.12 Nucleation mechanism vs. microstructure around the weld pool boundary of an alloy. [Ref. 14]

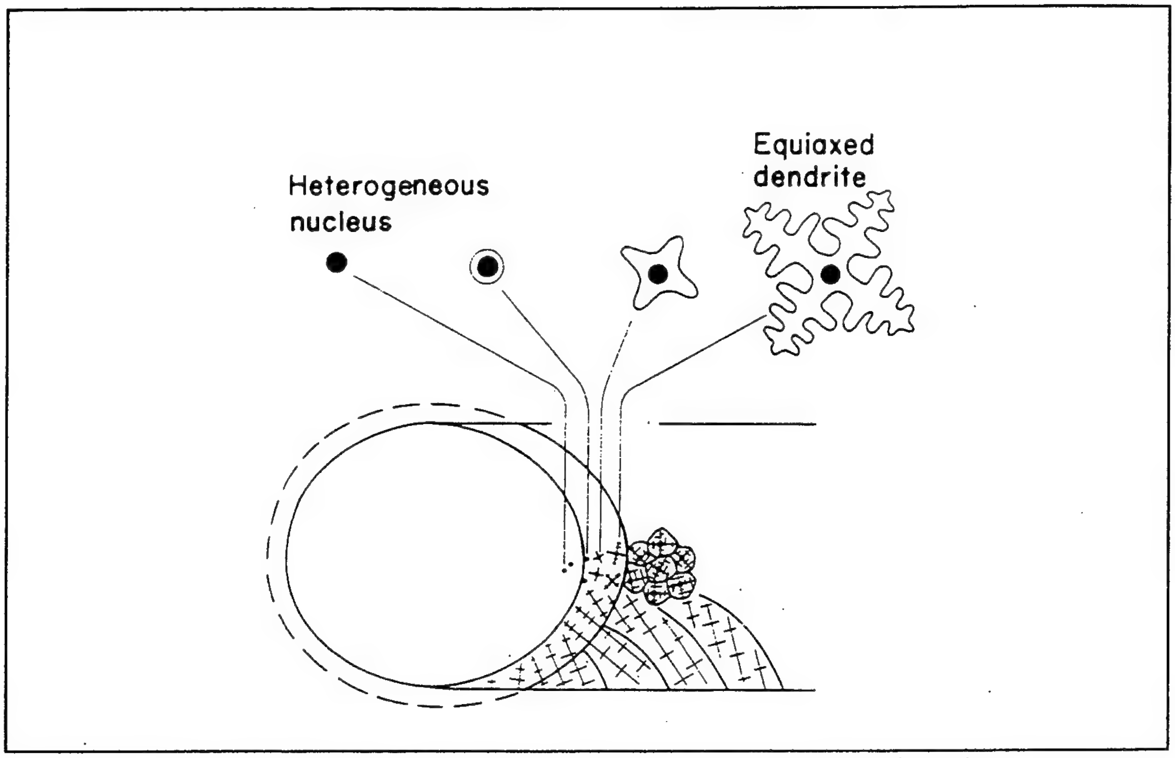
Heterogeneous nucleus
Equiaxed dendrite

Figure 2.13 Heterogeneous nucleation mechanism resulting in the formation of equiaxed grains in weld metal. [Ref. 14]

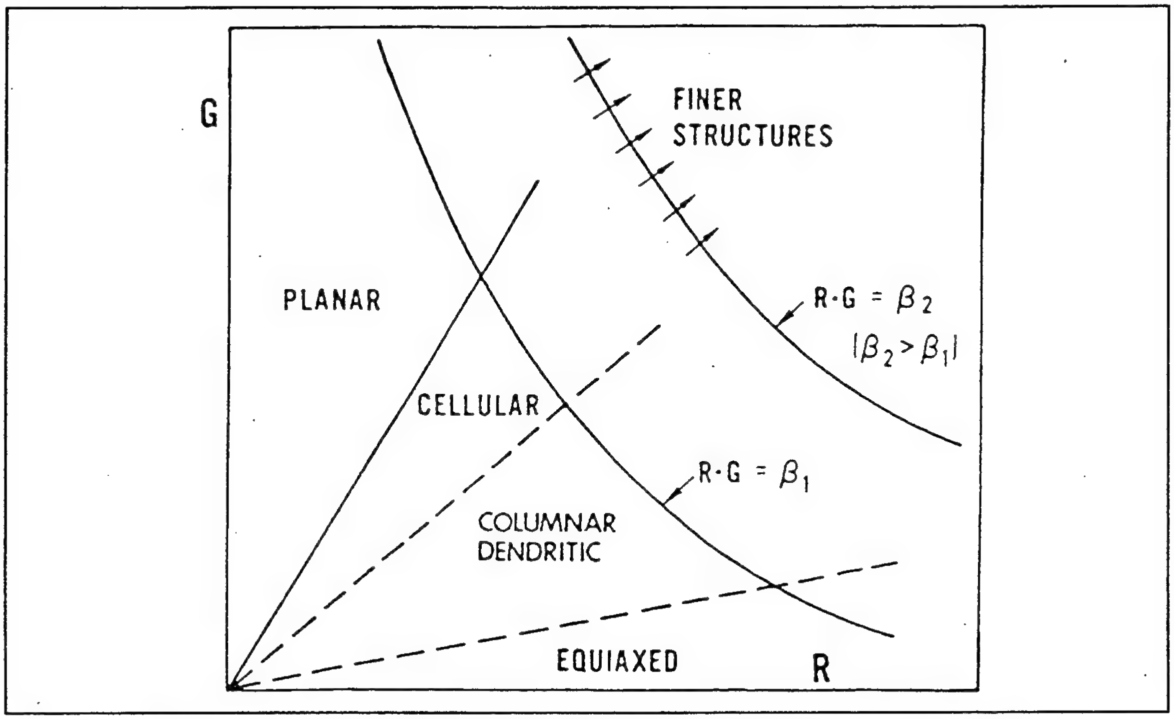
G
R
FINER STRUCTURES
PLANAR
CELLULAR
COLUMNAR DENDRITIC
EQUIAXED
R·G = β_2
($\beta_2 > \beta_1$)
R·G = β_1

Figure 2.14 Schematic rate-gradient map showing transition in microstructure as well as refining effect of high cooling rates.
[Ref. 14]

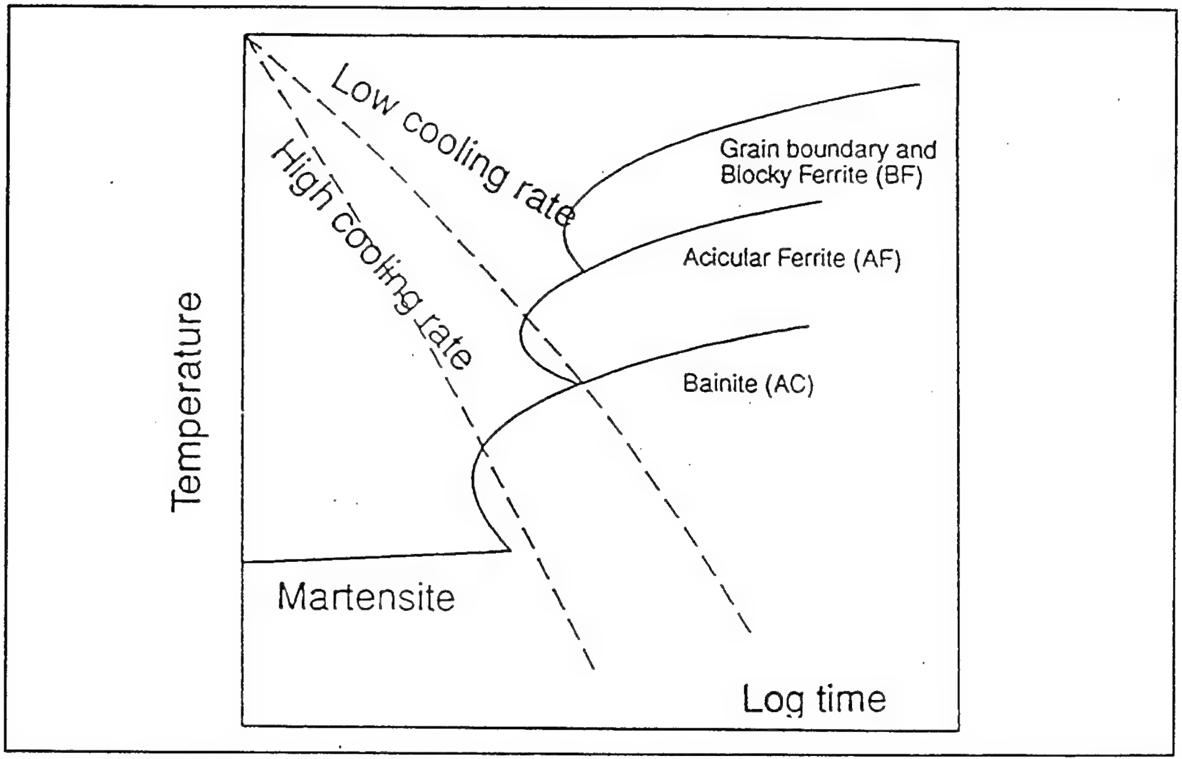
Low cooling rate
High cooling rate
Grain boundary and Blocky Ferrite (BF)
Acicular Ferrite (AF)
Bainite (AC)
Temperature
Martensite
Log time

Figure 2.15 CCT diagram and influence of cooling rate on the weld metal microstructure. [Ref. 29]

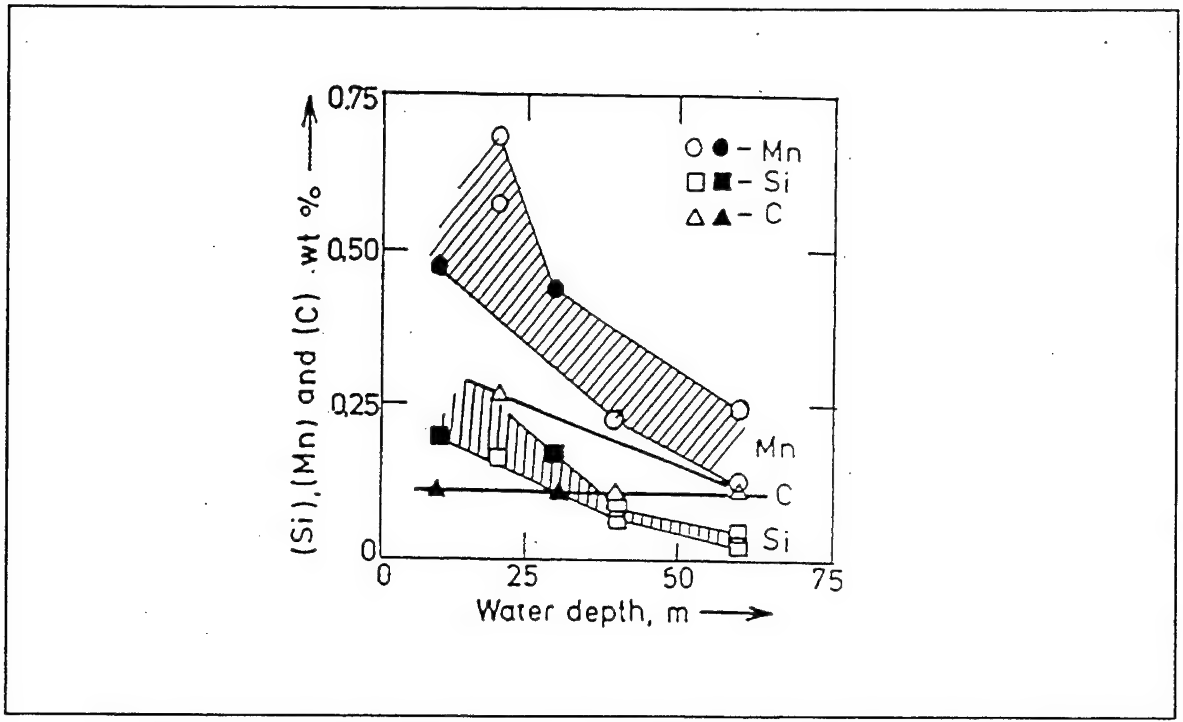

Figure 2.16 Alloying element variation in underwater wet welding vs. water depth. [Ref. 34]

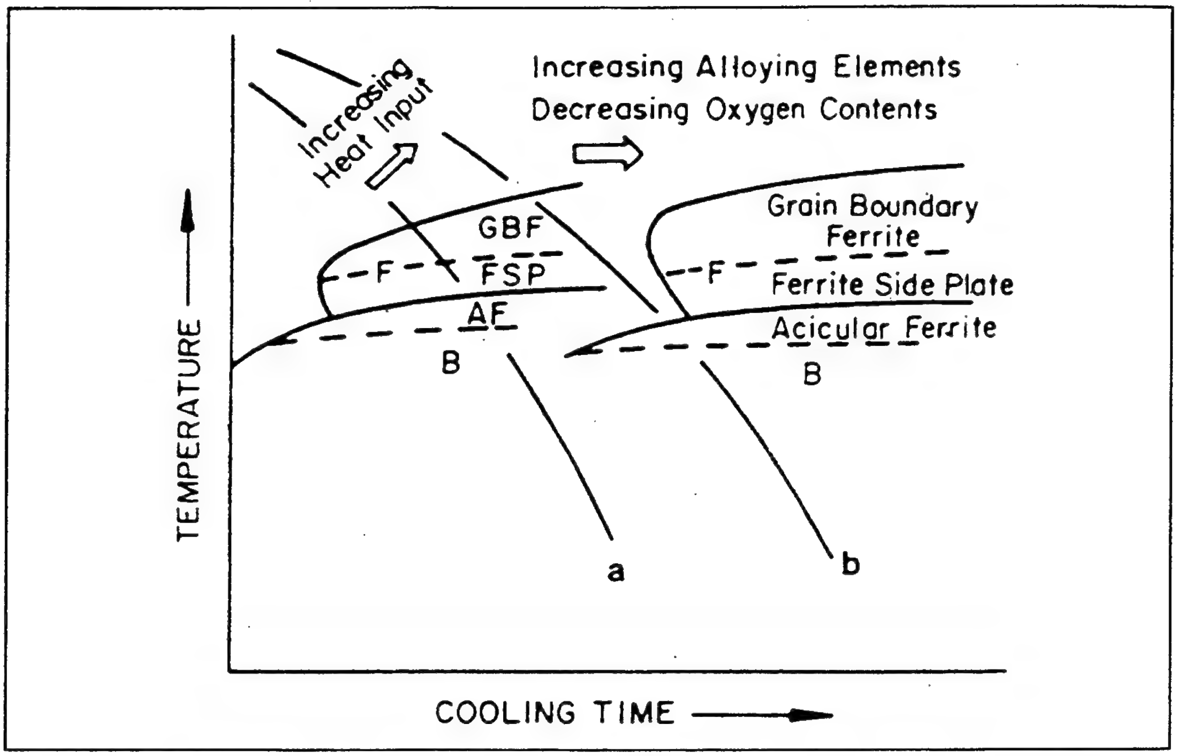
Increasing Heat Input
Increasing Alloying Elements
Decreasing Oxygen Contents
GBF
F
FSP
AF
B
Grain Boundary Ferrite
F
Ferrite Side Plate
Acicular Ferrite
B
a
b
TEMPERATURE
COOLING TIME

Figure 2.17 Schematic CCT diagram showing the influence of weld metal oxygen & manganese on hardenability.
[Ref. 14]

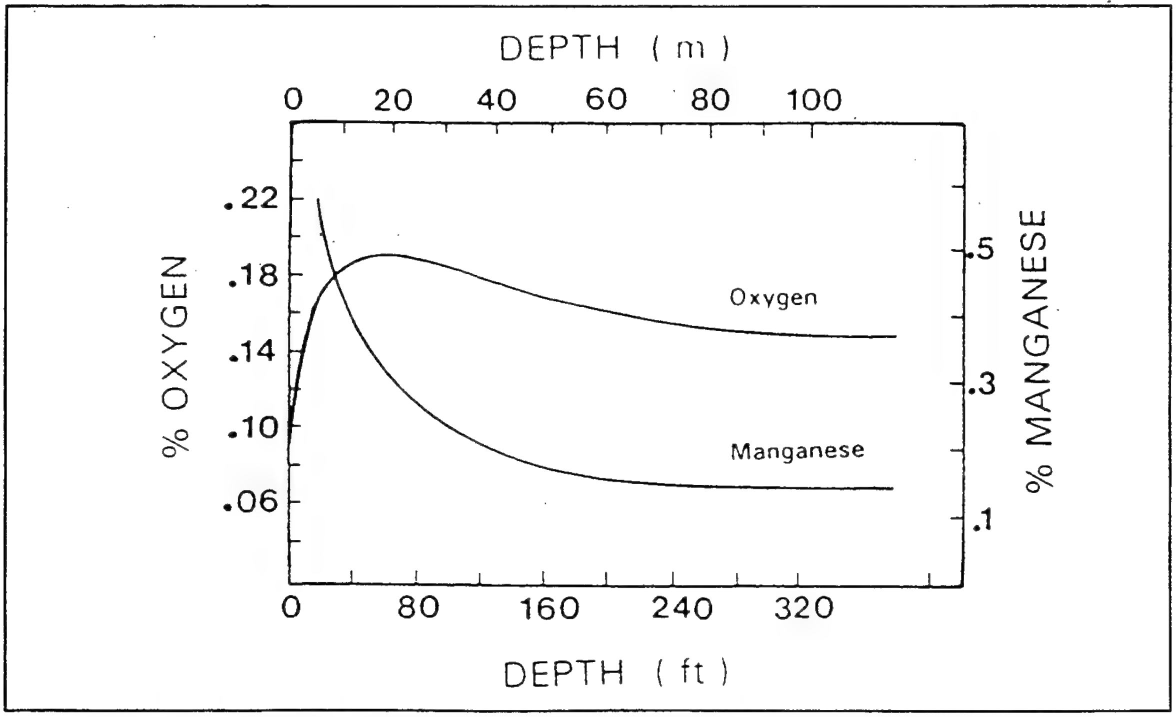

Figure 2.18 Variation of the oxygen & manganese contents with depth of underwater welding.
[Ref. 19]

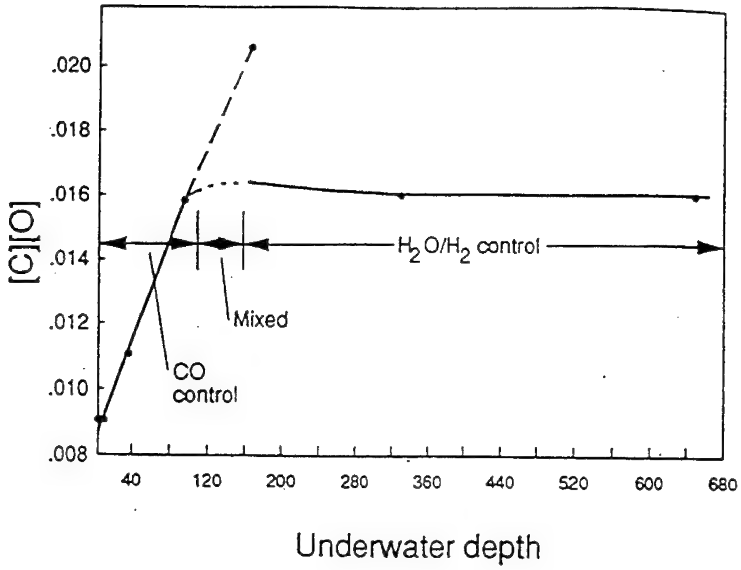

Figure 2.19 Product of weld metal carbon and oxygen content vs. water depth for weld metal produced with treated E6013 SMA electrode. [Ref. 29]

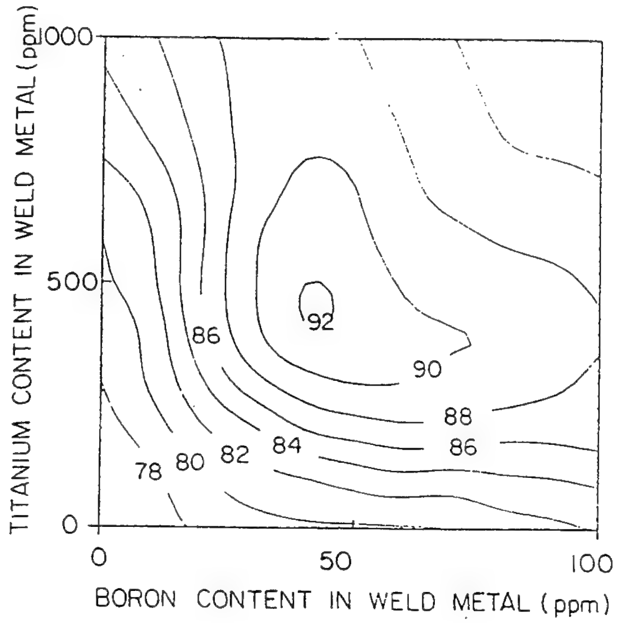

Figure 2.20 Combined effects of weld metal boron and titanium on volume fraction of acicular ferrite for surface welding. [Ref. 38]

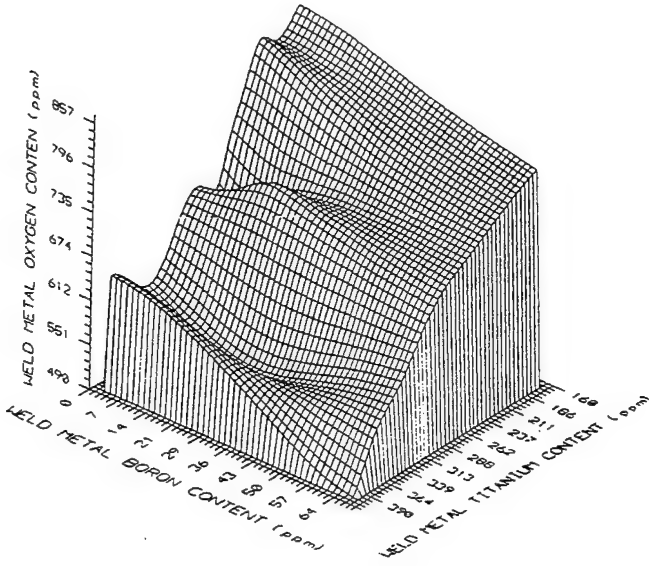

Figure 2.21 Effects of boron and titanium on weld metal oxygen levels of underwater wet welds. [Ref. 20]

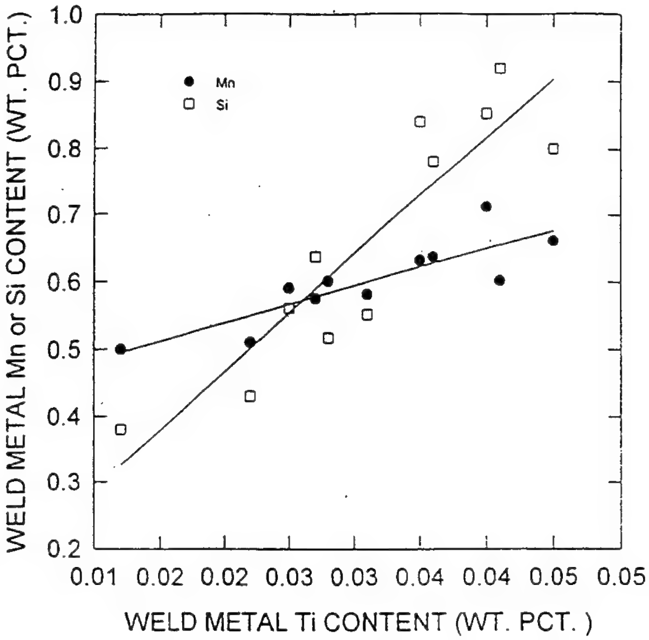

Figure 2.22 Effect of titanium on manganese and silicon content in underwater wet welds. [Ref. 20]

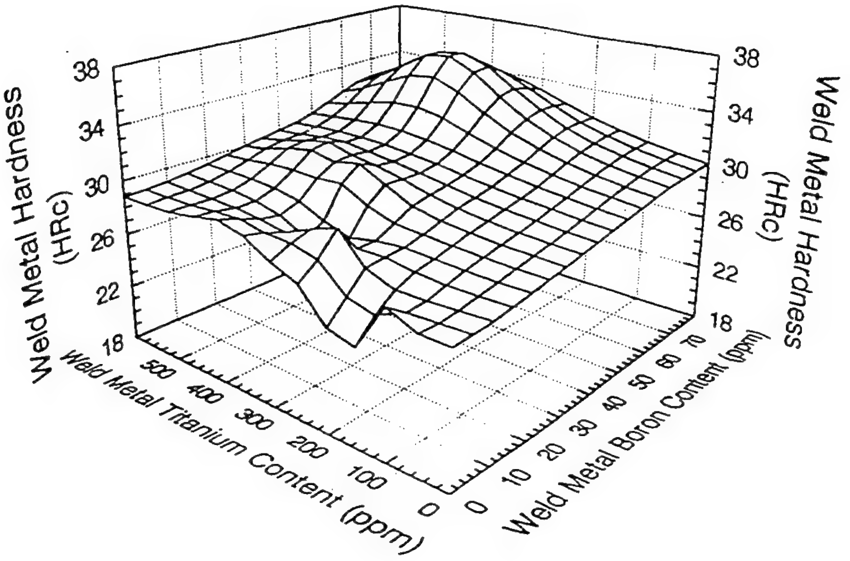

Figure 2.23 Effect of boron and titanium on weld metal hardness of underwater wet welding. [Ref. 20 &21]

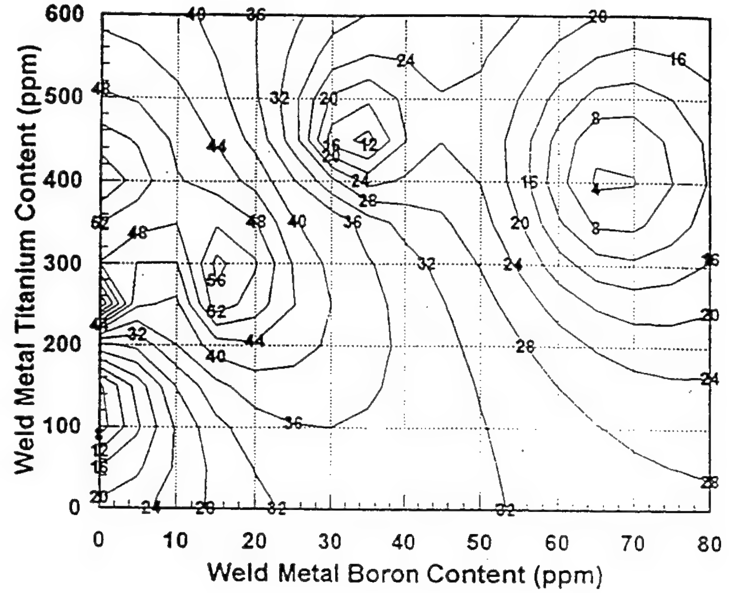

Figure 2.24 Contour map of acicular ferrite as a function of weld metal boron and titanium content of underwater wet welding. [Ref. 20]

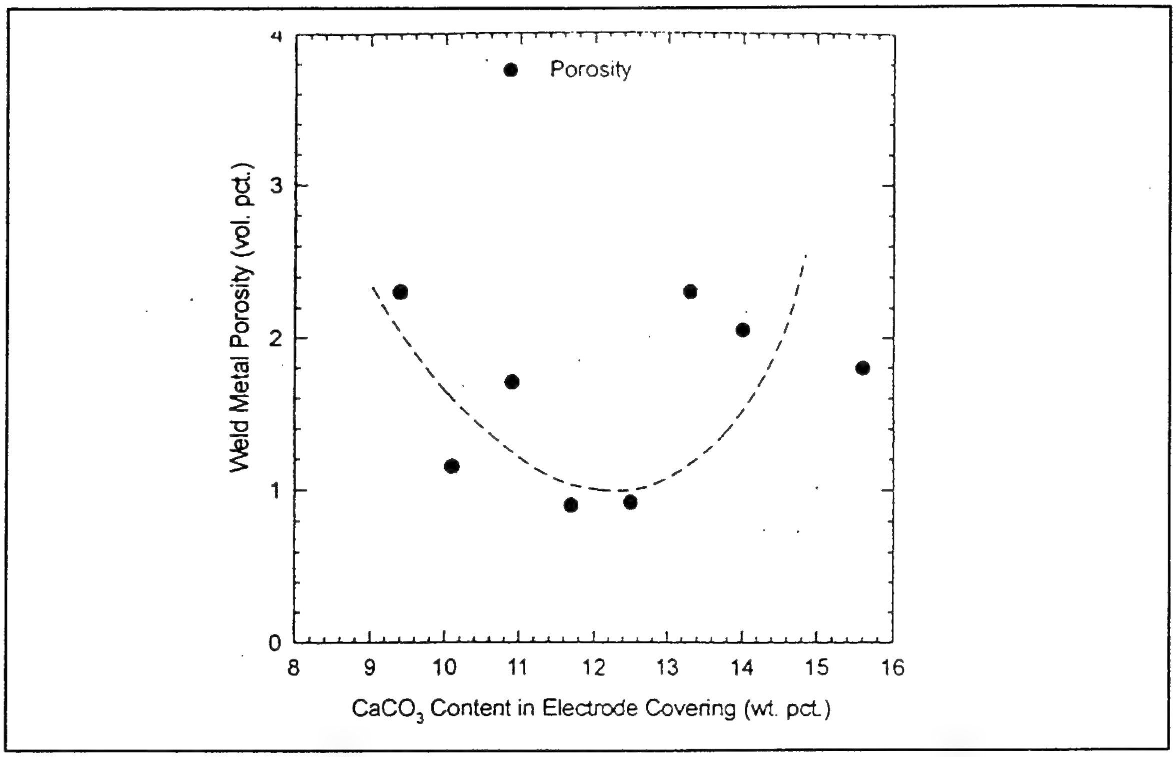

Figure 2.25 Effect of $CaCO_3$ on weld metal porosity of underwater welds. [Ref. 18 & 21]

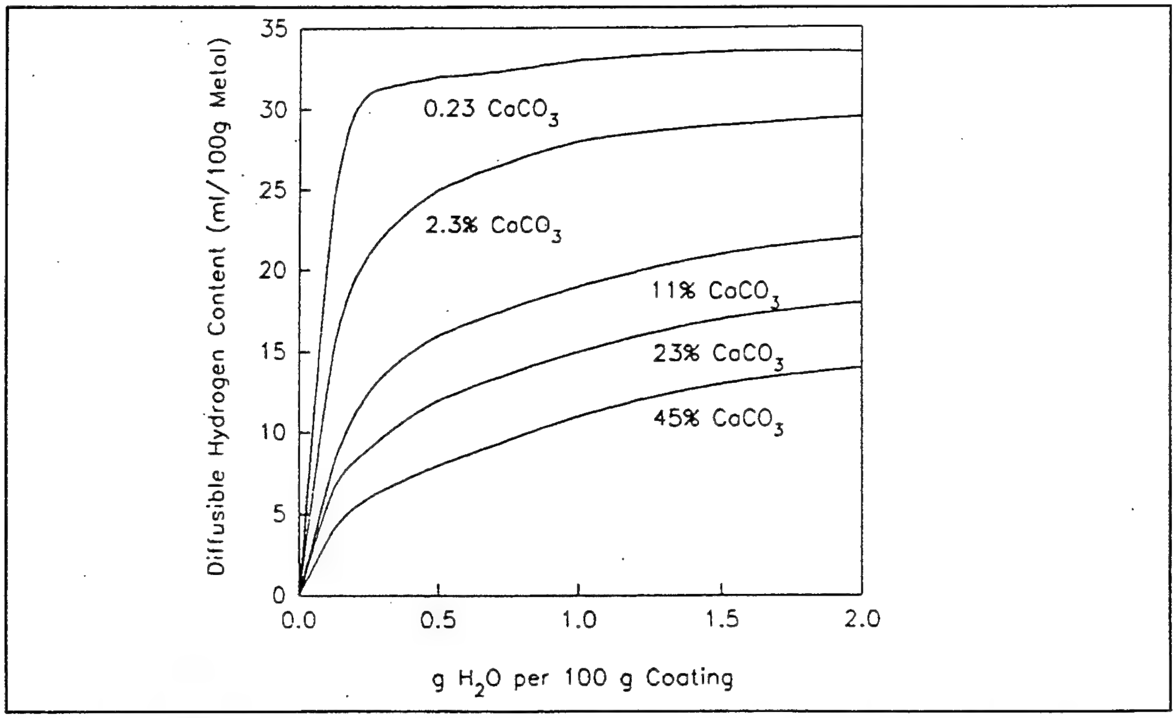

Figure. 2.26 Effect of $CaCO_3$ in the electrode coating on weld metal diffusible Hydrogen levels in surface welds. [Ref. 18]

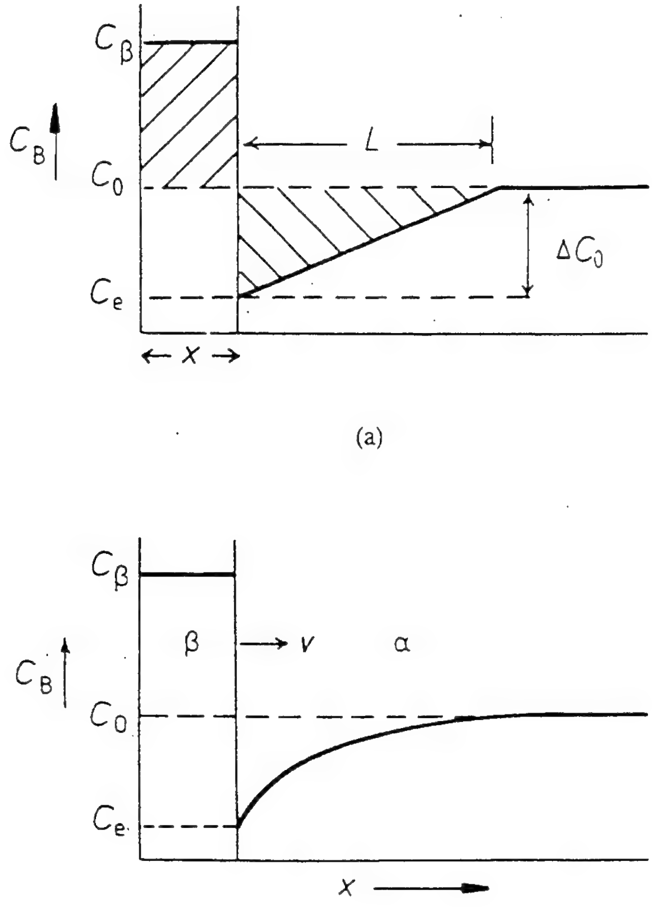
Cβ
CB
L
C0
ΔC0
Ce
x
Cβ
β
v
α
CB
C0
Ce
x

(a)

(b)

Figure 2.27 Composition profile for unidirectional thickening of inclusion growth. [Ref. 20]

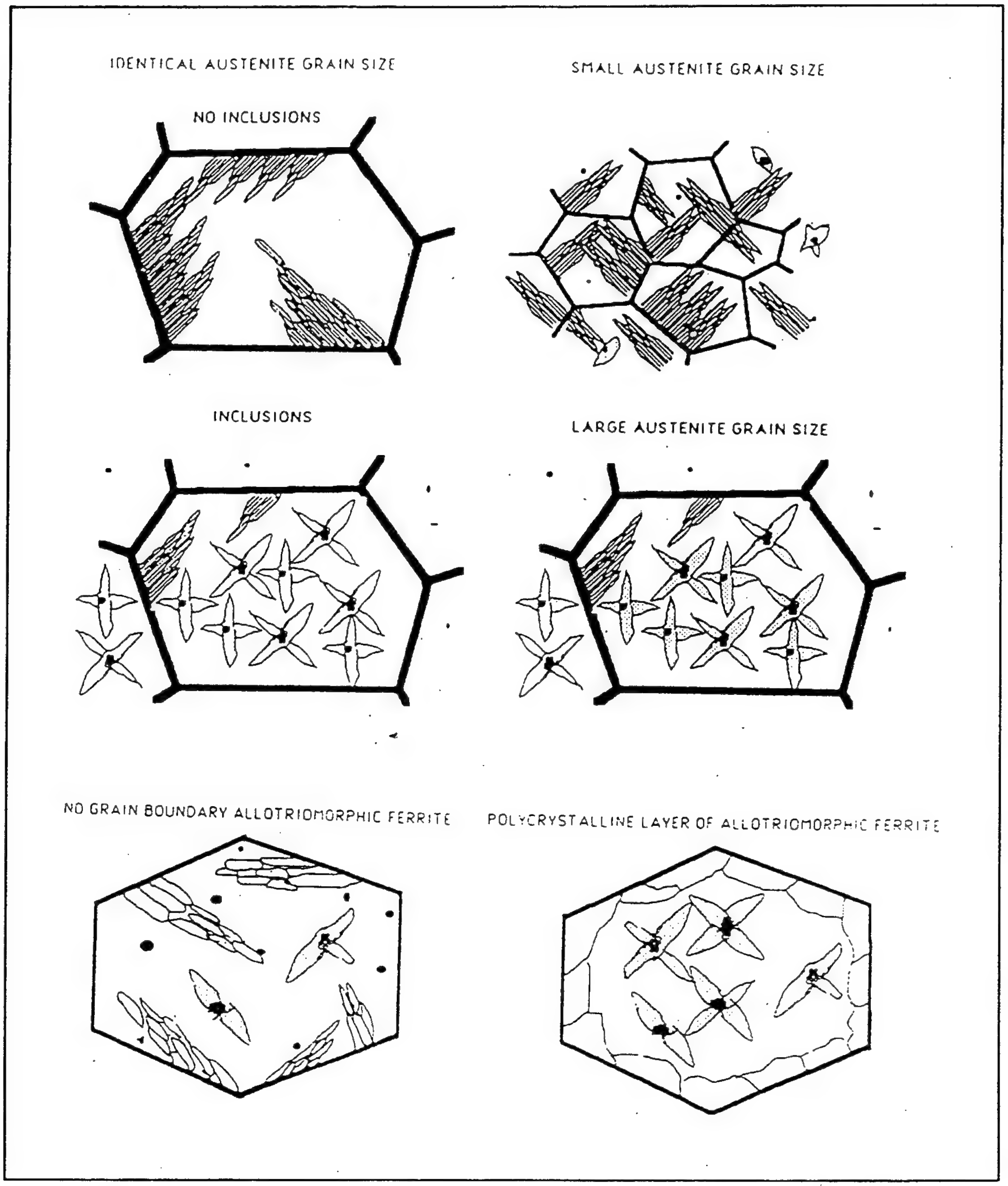
IDENTICAL AUSTENITE GRAIN SIZE
SMALL AUSTENITE GRAIN SIZE
NO INCLUSIONS
INCLUSIONS
LARGE AUSTENITE GRAIN SIZE
NO GRAIN BOUNDARY ALLOTRIOMORPHIC FERRITE
POLYCRYSTALLINE LAYER OF ALLOTRIOMORPHIC FERRITE

Figure 2.28 Schematic representation of the effect of inclusion size on austenite grain size and acicular ferrite formation. [Ref. 20]

III. EXPERIMENTAL PROCEDURE

A. WELD SAMPLES

Three weld samples (UWW03, UWW10, UWW31) along with three BROCO CS-1 wet welding electrodes were received from the Supervisor of Salvage and Diving (NAVSEA OOC), Arlington, Virginia, for analysis. The weld sample designation UWW10 means UnderWater Wet sample from a water temperature of 10°C, UWW03 a water temperature of 3°C and UWW31 a water temperature of 31°C. All welds were produced with an underwater wet shielded metal arc process on 19.1 mm (3/4 inch) test plates of ASTM A516 Gr70 steel with 3.2 mm (1/8 inch) diameter BROCO CS-1 wet welding electrodes. The joint configuration was identical in all three cases: a single-V, full penetration weld joint with a backing bar. In addition, the weldment was fully restrained using strongbacks. All welding was performed in the horizontal position by Oceaneering International using the NAVSEA approved procedure (OI-WW-56). The welding conditions and parameters are shown in Table 3.1.

After each weld sample was evaluated as discussed below they were sectioned and a weld metal sample and a base metal sample were sent out for chemical analysis. The chemical analysis results have not yet been received. However, general data on the base metal and SEM/EDX analysis of the weld metal is available and these will be discussed in the Results and Discussion. Base metal ASTM A516 Gr70 steel chemical analysis was conducted by Partek Lab on three different samples. These results were compared to the reported results of Lundin, et al. [Ref. 28]. This data is presented in Table 3.2. The base metal was analyzed using a multiple-burn technique.

The electrodes selected for qualification were 1/8 inch BROCO soft touch (CS-1). These electrodes are normally a E7014 Hobart electrode on which BROCO puts a special coating and finally covers with paraffin so that water is excluded form the flux. For the AWS classification (E7014): (1) the first two numbers specify the minimum tensile strength (70 KSI); (2) the third number (EXX1X) specifies for which welding positions the rod should be successful: 1= all welding positions; and (3) the fourth number (EXXX4) specifies the cover type and current: iron powder, titania and either polarity (AC or DC). Table 3.3 lists the nominal content/chemistry for these electrodes. An SEM/EDX analysis of the BROCO CS-1 was conducted; this will be discussed in the Results and Discussion section.

B. SAMPLE PREPARATION

Each weld sample was ground using 180, 220, 320, 500, 1000 and 2400 grit Struers waterproof silicon carbide paper on a Struers Knuth-Rotor-3. Final polishing was completed using 3 μm diamond suspension on Buehler Texmat 1000 followed by 0.05 μm alumina suspension on Buehler Microcloth on a Buehler Ecomet 4.

The BROCO CS-1 electrode was sectioned, then mounted in a sample "puck" of conducting phenolic mounting compound (carbon filled) using a Buehler Simplimet-2 mounting press. This mounting was required to allow scanning electron microscope analysis later. After mounting, the sample was ground and polished as above.

The samples were examined in the polished (unetched) condition for scanning electron microscope (SEM) analysis. After SEM analysis was completed, the weld samples were etched with a 5% nital solution for 5 seconds for optical microscopy. The samples were stored in a vacuum to reduce corrosion.

C. SCANNING ELECTRON MICROSCOPY

The polished weld samples were placed in a Cambridge Stereoscan S200 scanning election microscope (SEM) for inclusion type, size and volume fraction analysis. For improved observation, the SEM was operated in the backscattered mode. In order to differentiate between slag and an oxide inclusions, energy dispersive analysis of emitted x-rays (EDX) on each inclusion was performed. Fifty random fields were selected for analysis from the fusion zone of each sample. All inclusion measurements and EDX counts were taken with the SEM filament (LaB_6) energized to 20 KV at a working distance of 18 mm and a magnification of 7030X. Figure 3.1 illustrates a typical inclusion field. The inclusion field size was $152.6 \times 10^{-12}\ m^2$ for all measurements. The inclusion histograms, mean diameter, confidence and volume fraction were determined for each sample. The statistical analysis that was used to determine the mean inclusion diameter and the standard deviation from a population normally tried to incorporate a confidence. Where the confidence is the range on either side of the sample mean that 99% of all data should exist. The confidence was calculated by:

$$\text{Confidence} = \pm 2.575\ (\sigma_d / (n)^{(1/2)}) \tag{3.1}$$

where

n = population

σ_d = standard deviation = $[(n\mathcal{E}d^2-(\mathcal{E}d)^2)/n(n-1)]^{(1/2)}$

The inclusion volume fraction was calculated using the equation below:

$$\text{Volume fraction} = \left(S\pi d^2\right)/4f \tag{3.2}$$

$S \equiv$ Average number of inclusions per field

$f \equiv$ Inclusion field size ($152.6 \times 10^{-12}\ M^2$)

$d \equiv$ Mean diameter of inclusion sample

The volume fraction and the area fraction were assumed to be the same as the polished plane contains the same average area fraction as any other plane in the sample and therefore the same volume fraction.

The BROCO CS-1 electrode was analyzed with the SEM/EDX to determine the nominal chemistry. This is listed in Table 3.3 and will be discussed again in the Results and Discussion section.

The cracked section of the UWW03 sample was sectioned using the Buehler Isomet 2000 with a diamond blade. A 2.5 mm (0.1 inch) slice was then cooled in liquid nitrogen and the crack surface was exposed and cleaned as discussed in Volume 12 of the Metals Handbook[Ref. 39]. These fracture surfaces were then analyzed in the SEM to try to identify the mechanism of failure.

D. OPTICAL MICROSCOPY

The weld samples were examined optically after SEM analysis and etching as described above. First, macroscopic photographs were taken by GRM Photo, Inc. using a standard macro lens on a 35 mm camera. The macrophotographs are shown in Figures 3.2 through 3.4. Higher magnification analyses were then conducted on a Ziess Jenaphot 2000 optical photomicroscope with an attached Pulnix TMC-74 optical camera connected to a 486/DX2 computer with Semicaps software. This was done to obtain micrographs for analysis. Fusion zone microstructure analysis for individual microstructure constituents using ASTM-E562 practice for determining volume fraction at three distinct zones was provided by Partek Laboratories, Inc.:

* Zone A ≡ weld metal unaffected by subsequent passes

* Zone B ≡ weld metal inner edge of HAZ with particle grain refinement

* Zone C ≡ weld metal outer edge of HAZ with full grain refinement

Tables 3.4 through 3.6 provide a summary of their results.

E. MICROHARDNESS ANALYSIS

Results of microhardness testing from the initial failure at Puget Sound Naval Shipyard were provided by Partek Labs, Inc. and are presented in Table 3.7. Their testing was with a Vickers-type testing unit with a 5 Kgf load (HV5).

The weld samples provided were analyzed for microhardness using a Buehler Micromet 2004 with a 360° rotating stage. The load applied (0.20 Kgf, HV0.2) was minimized in order to obtain more exact measurements near the cracking with less averaging effect of a larger diamond pyramid indenter. Measurements were taken randomly of the base metal and the HAZ and FZ at both the toe and midsection location for each sample. Then transverse hardness readings were taken at the cap and completely across the weldment starting in the base metal with a step size of 0.635 mm (0.025 inch). Finally, hardness readings were taken around the cracking noted in UWW03 and UWW10 samples.

Weld Sample #	Partek Inc #	Welding conditions and parameters.					
		Environmental Conditions			Horizontal Position		
		Temperature	**Depth**	**Location**	**Voltage (volts)**	**Current (amps)**	**Travel spd, (in./min.)**
UWW03	30154-3	2.8°C (37°F)	6.7m (22ft)	Seawater, open water.	24 - 33	120 - 155	5.0 - 8.0
UWW10	30382-3	10°C (50°F)	5.5m (18ft)	Seawater, open water.	24 - 33	120 - 155	5.0 - 8.0
UWW31	95-281	31°C (88°F)	7.3m (24ft)	Freshwater , test tank.	24 - 33	120 - 155	5.0 - 8.0

Table 3.1 The welding conditions and parameters.

ELEMENTS Wt%	Partek, 1/29/93	Partek, 5/25/94	Partek, 3/30/95	Partek, Average	Lundin [Ref. 28] A516-70H
Carbon	0.21	0.20	0.22	0.210	0.21
Manganese	1.10	0.98	0.93	1.003	0.97
Phosphorus	0.019	0.014	0.014	0.016	0.007
Sulfur	0.004	0.022	0.023	0.016	0.002
Copper	0.02	0.15	0.03	0.067	0.06
Nickel	0.02	0.06	0.08	0.053	0.05
Chromium	0.02	0.04	0.04	0.033	0.04
Molybdenum	<0.01	0.01	0.08	0.033	0.01
Silicon	0.28	0.26	0.22	0.253	0.20
Vanadium	<0.01	<0.01	<0.01	<0.01	0.002
Titanium					0.002
Aluminum	0.07	0.04	0.06	0.057	0.019
Niobium					0.002
Oxygen					0.002
Nitrogen					0.009
Tin		<0.01	0.01	<0.006	
CE, AWS D3.6	0.4040	0.3893	0.4083	0.4004	0.3894
CE + Si/6	0.4507	0.4327	0.4450	0.4425	0.4227

Table 3.2 Base metal ASTM A516 Gr70 steel chemical analysis.

Constituent of Covering	Function of Constituent	Composition Ranges		Filler Metal Chemistry		Filler Metal Mechanics	
Composition	**Primary**	**Secondary**	**E7014**	**Elements**	**Wt %**	**As, Welded**	
Cellulose	Shielding gas	-	2 - 6	**Carbon**	0.06	**UTS**	79 Ksi
Calcium carbonate	Shielding gas	Fluxing agent	0 - 5	**Manganese**	0.54	**YS**	68.1 Ksi
Titanium dioxide (rutile)	Slag former	Arc stabilizer	20 - 35	**Phosphorus**	0.026	**Elongation % in 2"**	27.5
Feldspar	Slag former	Stabilizer	0 - 5	**Silicon**	0.35		
Mica	Extrusion	Stabilizer	0 - 5	**Sulfur**	0.013		
Clay	Extrusion	Slag former	0 - 5				
Iron powder	Deposition rate	Contact welding	25 - 40				
Ferrosilicon	Deoxidizer	-	0 - 5				
Ferromanganese	Alloying	Deoxidizer	5 - 10				
Sodium silicate	Binder	Fluxing agent	0 - 10				
Potassium silicate	Arc stabilizer	Binder	5 - 10				

Table 3.3 Nominal Composition for E7014 Electrodes.
[Ref. 5]

Microconstituent / Location	Unaffected Weld Metal Zone A	Partial Grain Refinement Zone B	Full Grain Refinement Zone C
% Grain Boundary Ferrite	4.2	28.0	<1.0
% Acicular Ferrite	37.0	28.0	51.0
% Windmanstatten S.P.	7.0	<1.0	<1.0
% Total Ferrite	48.2	56.0	51.0

Table 3.4 Microconstituent volume fraction for UWW03.

Microconstituent / Location	Unaffected Weld Metal Zone A	Partial Grain Refinement Zone B	Full Grain Refinement Zone C
% Grain Boundary Ferrite	2.0	14.0	<1.0
% Acicular Ferrite	38.0	48.0	60.0
% Windmanstatten S.P.	2.8	<1.0	<1.0
% Total Ferrite	58.2	62.0	60.0

Table 3.5 Microconstituent volume fraction for UWW10.

Microconstituent / Location	Unaffected Weld Metal Zone A	Partial Grain Refinement Zone B	Full Grain Refinement Zone C
% Grain Boundary Ferrite	8.0	5.7	<1.0
% Acicular Ferrite	34.0	51.0	68.6
% Windmanstatten S.P.	2.8	<1.0	<1.0
% Total Ferrite	44.8	56.7	68.6

Table 3.6 Microconstituent volume fraction for UWW31.

MICROHARDNESS TEST DATA:

Weld #1

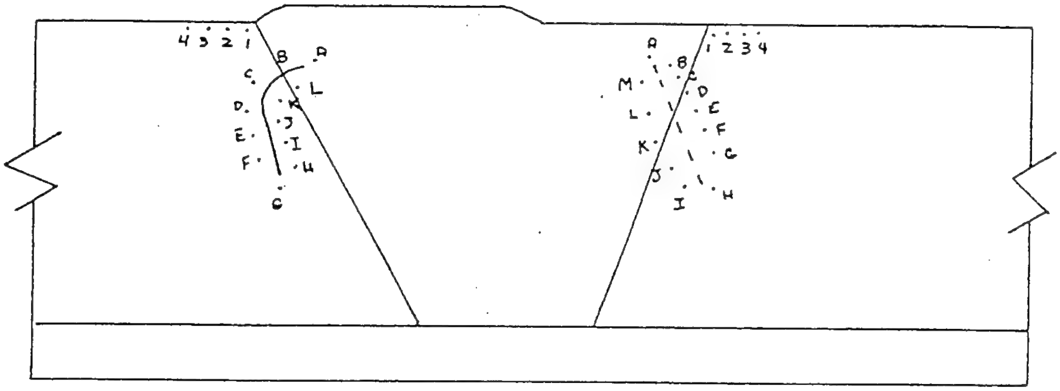

All hardness testing was performed using a Vickers-type test unit applying a 5 Kgf load (HV 5).

Top of Weld

Test Loc.	Hardness	Test Loc.	Hardness
1	386	1	441
2	367	2	299
3	241	3	239
4	190	4	185

Around Crack

A.	283	G.	219
B.	251	H.	265
C.	221	I.	232
D.	197	J.	254
E.	257	K.	199
F.	203	L.	260

Opposite Side

A.	251	H.	221
B.	241	I.	303
C.	371	J.	280
D.	283	K.	229
E.	241	L.	227
F.	229	M.	239
G.	223		

Table 3.7 Microhardness testing from the initial failure at Puget Sound Naval Shipyard.

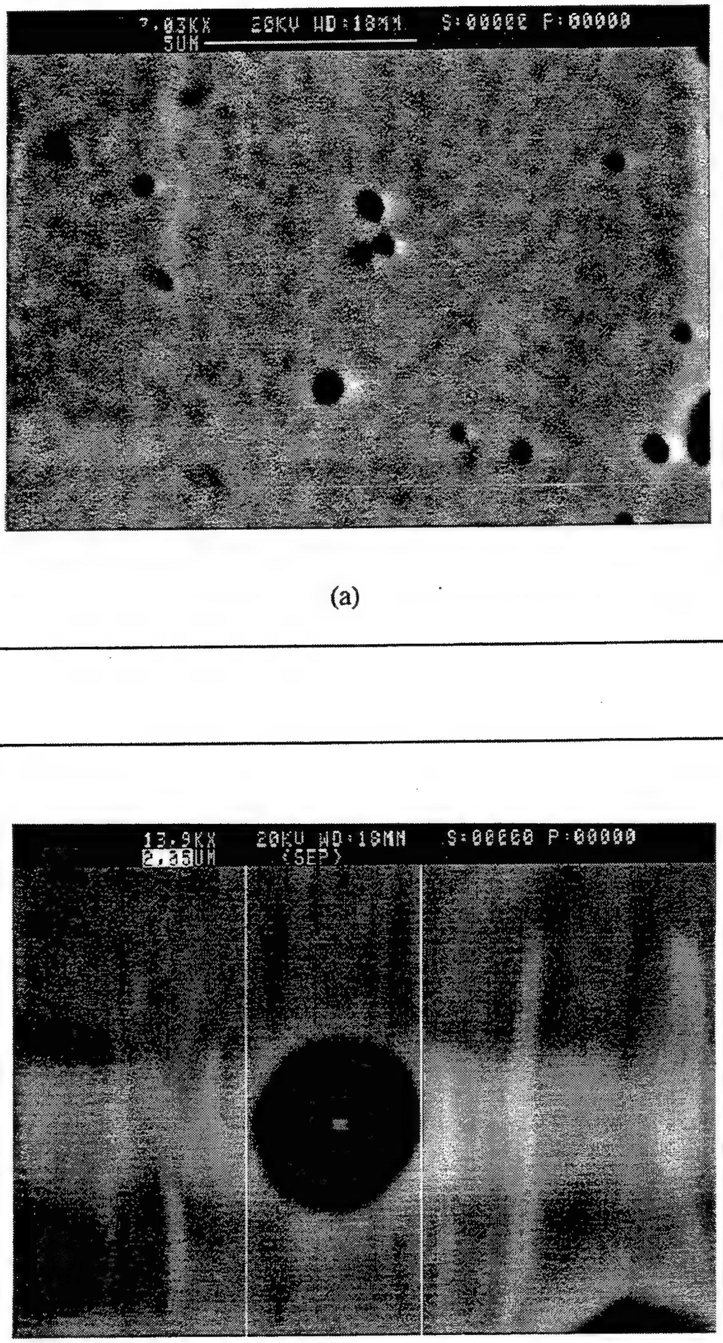
7.03KX 20KV WD:18MM S:00002 P:00000
5UM
13.9KX 20KV WD:18MM S:00000 P:00000
2.35UM
(SEP)

(a)

(b)

Figure 3.1 SEM micrograph illustrating (a) typical inclusion field and (b) method of measurement

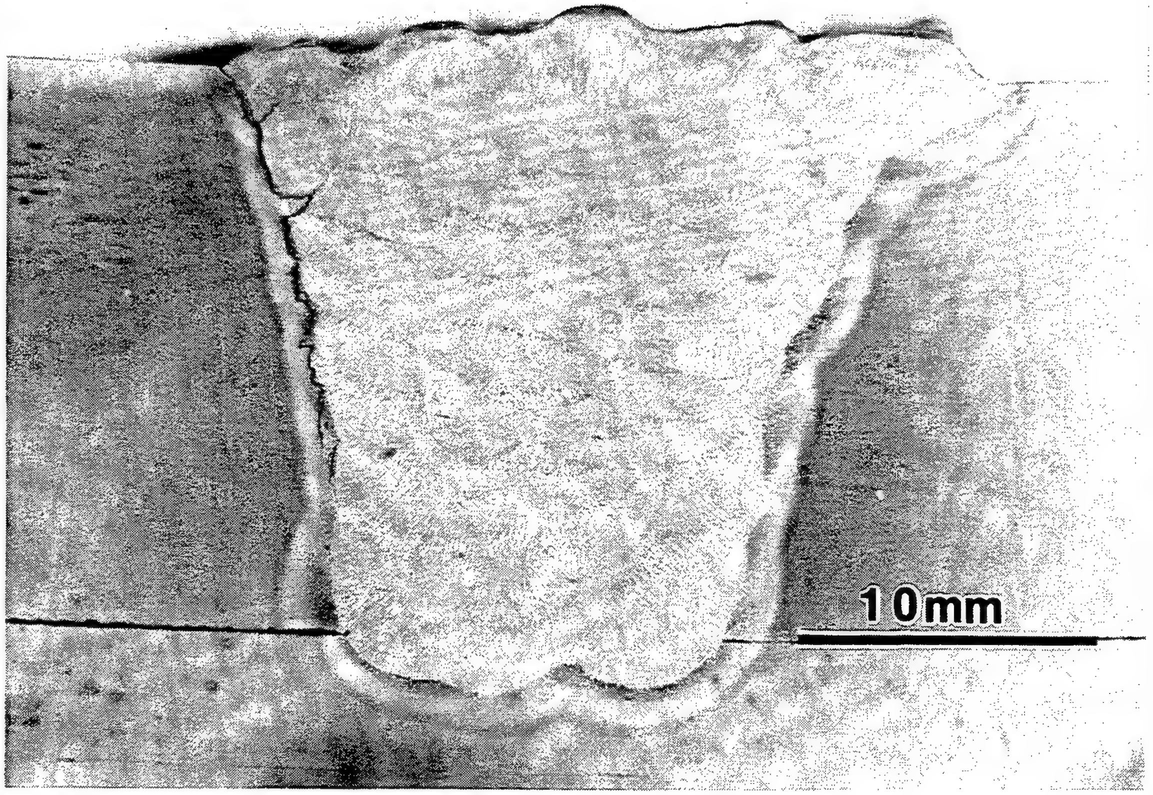

Figure 3.2 Macrophotograph of UWW03 weld sample. Welded at a depth of 6.7m in seawater and at a temperature of 2.8°C.

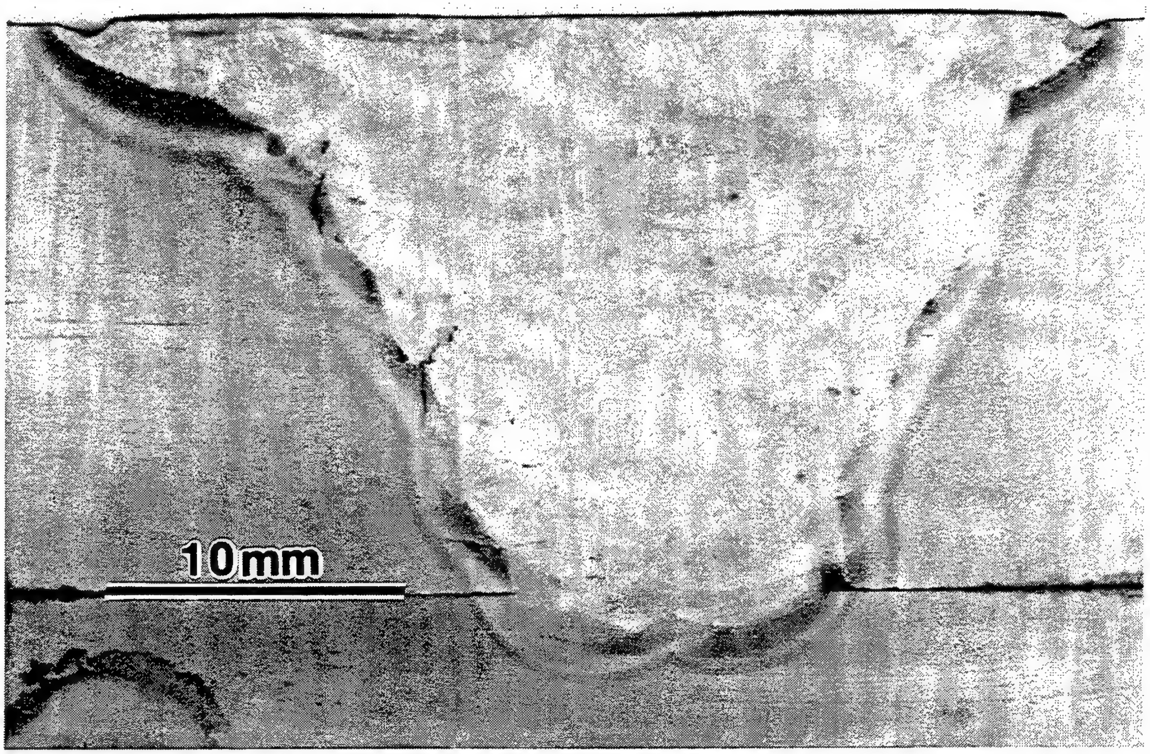

Figure 3.3 Macrophotograph of UWW10 weld sample. Welded at a depth of 5.5m in seawater and at a temperature of 10°C.

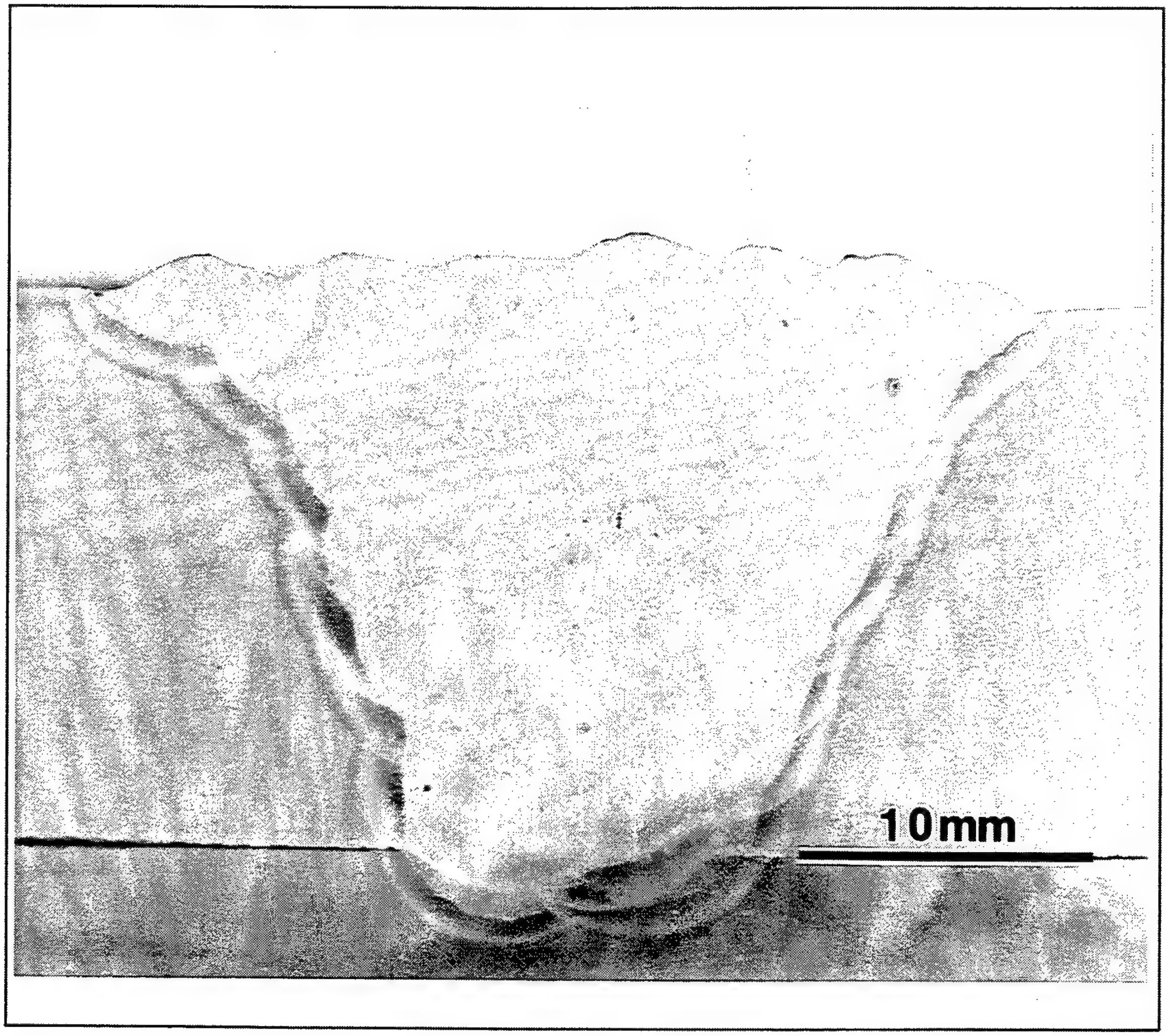

Figure 3.4 Macrophotograph of UWW31 weld sample. Welded at a depth of 7.3m in freshwater and at a temperature of 31°C.

IV. RESULTS AND DISCUSSION

A. WELD METAL

The final chemical analysis results have not yet been received. However, the SEM/EDX analysis results of the weld metal and the electrode filler rod and flux have been compiled into Table 4.1. Figure 4.1 is a typical spectrum of the weld metal. The base metal information is listed in Table 3.2.

1. Weld Metal Composition

The weld metal composition is dependent upon the base metal composition, filler rod composition, the environmental effects of hyperbaric pressure and dissociation of H_2O into hydrogen and oxygen [Ref. 29]. The results of the SEM/EDX analysis is a good base line. Unfortunately this data is not sufficient to fully understand the weld metal chemistry since light elements (i.e., less than atomic number 11) are present in such small amounts it is impossible to quantify them. Figure 4.1 is a typical EDX spectrum from the weld metal. As a result important information about the oxygen and carbon was not obtained for the samples. Since the welds were completed with the same electrodes and the depths were very close, the expected results would be for the oxygen and carbon content to increase over a weld made on the surface. Figure 2.18 and 2.19 show these expected results. Furthermore, the manganese and silicon will/should decrease as the depth increases.

2. Electrode Composition

The BROCO CS-1 electrode was analyzed with the SEM/EDX. EDX analysis was conducted on the filler rod, the flux and the special waterproof coating as discussed in the Experimental Procedure. The BROCO CS-1 electrode is a modified Hobart E7014 electrode. Figure 4.2 is a SEM cross-section micrograph showing the filler rod and flux coating while Figure 4.3 is a micrograph of the flux. The EDX results of the weld metal and the flux listed in Table 4.1 verify the standard specifications listed in Table 3.3 when compared. Furthermore, the special coating listed in Table 4.1 is probably an aluminum-silicon alloy, which is close to the eutectic composition. Figure 4.4 is a micrograph of the special coating. The use of this alloy to form a protective coating for waterproofing may be helpful in other ways since this alloy deoxidises the weld metal and could help in the formation of normal oxide inclusions[Ref. 20]. In fact, the extra silicon may help to off set to effect of lower silicon levels due to depth seen in Figure 2.22.

B. NON-METALLIC INCLUSIONS

1. Size and Volume fraction

Inclusions in the fusion zone were analyzed for all three weldments for mean diameter, standard deviation, confidence and volume fraction as described in the Experimental section (IIIC). Since, the amount of slag and porosity in underwater wet welds was so high it made the task more complex. In order to differentiate between "normal" oxide inclusions and slag inclusions, the SEM was set up with a longer working distance (18mm) such that EDX analysis could be utilized. After a randomly selected field, see Figure 3.1(a), had been mapped each "inclusion" was measured, see Figure 3.1(b), and an electron probe microanalysis was conducted to obtain an EDX spectrum for classification.

2. Inclusion Differential Chemical Analysis

Inclusions resulting from weld metal oxidation were found to have an MnO, SiO_2, Ti_xO_y and Al_2O_3 type of chemical composition with a spherical morphology. The slag inclusions had irregular shapes and a CaO, SiO_2 and Al_2O_3 type of chemical composition. As a result the oxide inclusions normally produced both strong Mn and Ti Kα signals while the slag inclusions gave higher Al, Si and Ca Kα intensities. Figure 4.5 shows a typical oxide inclusion EDX spectrum and Figure 4.6 shows a typical slag inclusion EDX spectrum. The use of the EDX analysis was very effective; however, since each inclusion needed to be analyzed the process of measurement and classification became very slow and tedious.

Three additional problems were presented in the classification of the inclusions. First, the backscatter detector has silicon in it, so, the Si Kα peak in the EDX spectrums was enlarged somewhat. Therefore, each EDX reading was not reviewed on the absolute value but was "normalized" by the operator before the inclusion was classified. Second, the backscatter mode could return a view that sometimes appeared to be an inclusion which subsequently turned out to be porosity which would return a typical weld metal EDX spectrum. Sometimes the porosity could be determined by adjustments to the backscatter detector and the time to run the EDX analyzer was not required. However, since the volume fraction of porosity in wet welds can be near 5% as discussed in the Background this differential analysis became important. Third, the smaller inclusions would not return a significantly different EDX spectrum to the weld metal. This can be explained by referring to Figure 4.7 which shows the bulb of interaction of the electron microprobe with the sample material.[Ref. 31] As the diameter of the inclusion becomes smaller the bulb will actually be reacting with the weld metal underneath the inclusion, thereby, the resulting EDX spectrum will be mostly that of the weld metal. In the end the operators experience, which improved as time progressed, was required to make the classification in the presence of these three problems.

3. Inclusion Observations

With the process established the inclusion statistics were analyzed and the resulting mean diameter and volume fraction of each weld sample was determined. Table 4.2, 4.3, and 4.4 display the statistics for the inclusions of each weld sample. From this information the total, the slag and finally the oxide inclusion distributions were plotted on a histogram for UWW03 in Figures 4.8, 4.9, and 4.10. The total, the slag and the oxide inclusion distributions were plotted on a histogram for UWW10 in Figures 4.11, 4.12, and 4.13. The total, the slag and the oxide inclusion distributions were plotted on a histogram for UWW31 in Figures 4.14, 4.15, and 4.16.

The expected weld metal oxygen content will be higher then a surface weld as seen in Figure 2.18. This indicates that the mean inclusion diameters will be larger than those of a surface weld. The increase in the inclusions mean diameter and volume fraction with an increase in the weld metal oxygen content is anticipated.[Ref. 20] This is because the higher oxygen content results in increased reaction of deoxidizing elements within the weld metal which leads to more and larger inclusions. With this information and the data listed in Tables 4.2 -4.4, it is reasonable to conclude that weld metal oxygen content increases with water temperature, since the volume fraction and numbers of oxide inclusions have increased directly with the ambient temperature.

The UWW31 sample had the largest number of inclusions and was the most difficult to analyze. There were over three times as many slag inclusions compared to either UWW03 or UWW10. This is important since, as noted above, it appears that the oxygen content is higher at higher water temperature and as Ibarra, et al., [Ref. 29] noted the diffusible hydrogen levels of the weld metal appear to be inversely related to the weld metal oxygen content. This argument indicates that diffusible hydrogen contents are likely to be less in higher temperature water; therefore, lowering the likelihood of hydrogen assisted cracking. A probable explanation for this is that the hydrogen is actually trapped around the oxide inclusions and in the porosity in the weld metal. This is a result of the reaction of the increased oxygen in the weld metal.

The UWW03 and UWW10 samples had a few inclusions that appeared to contain some sodium and chlorine, these elements were not seen in the UWW31 sample. As discussed the ions in the saltwater normally aid the plasma stability. Apparently some were trapped in the weld metal and may have aided in the heterogeneous nucleation of inclusions. The UWW03 sample had some large irregular shaped inclusions which appeared to have daughters. In these inclusion types the larger slag type of an inclusion would be in contact with the smaller spherical oxide inclusion indicating that it acted as a nucleation site.

C. MICROHARDNESS ANALYSIS

Each weld sample was analyzed as described in the experimental section. The maximum, average and minimum Vickers hardness data for each weldment is presented in Table 4.5. The hardness profile across the mid-section of each weldment is presented in Figure 4.17. The hardness values in the HAZ and especially in the last pass weld cap area were very high. The hardness profile across the last pass weld cap for each weldment is presented in Figure 4.18. This is an indication of the extremely brittle nature of the HAZ and the expected almost 100% martensite microstructure. This microstructure is very susceptible to hydrogen induced cracking. Additional analysis and comparison of the optical (at the Vickers indentation) microstructural condition at these high microhardness values verified that the microstructure was martensitic. Results of microhardness testing from the initial failure at Puget Sound Naval Shipyard were provided by Partek Labs, Inc. and were presented in Table 3.7. As discussed in the Experimental section the load applied for the current testing (0.20 Kgf, HV0.2) was minimized in order to obtain more exact measurements. Therefore, the results reported here should be more exact, since the Vickers diamond indentor is smaller and the averaging effect over different microstructures will be minimized.

D. MICROSTRUCTURAL ANALYSIS

1. Macroscopic

The macroscopic micrographs up to 64X showed the massive extent of the cracking in the UWW03 sample. The UWW10 sample appeared to have only two cracks and the UWW31 sample appeared to be crack free, however, while conducting microscopic analysis very fine HAZ cracking was discovered in this sample. The multipass weld nature is clearly seen in the macrographs of each sample (Figure 3.2 - 3.4) and is as described by Lundin, et al., [Ref. 28] as seen in Figure 2.6. This Figure clearly shows how each HAZ region is effected by the second pass. Each section of the first weld will be further altered by the second pass, thereby, the microstructure will be altered. This can lead to local brittle zones which are discontinuous and may be surrounded by tougher structures. This sort of behavior was indeed observed during the microhardness measurements. In fact, there are even gaps in the HAZ which resulted in lower hardness values, this can be seen clearly in the UWW10 sample shown in Figure 3.3.

2. Microscopic

The BROCO CS-1 electrode cross-section was inspected on the SEM with the EDX to verify the chemical composition. The microscopic analysis was confined to the verification of the size and distribution of the flux and the special coating. As can be seen in Figure 4.3 the flux is a composite of many fine particles and it is bound together with a non-metallic material (clay) which is approximately 1 mm thick, while the special oxide coating is only about 10 μm thick. The EDX analysis that was displayed in Table 4.1 verified the standard nominal composition which was listed in Table 3.3.

Partek analysis of the weld samples was conducted in September 1995. The volume fractions of the microconstituents were reported and have been summarized in Tables 3.4 - 3.6. This data clearly indicates that the amount of acicular ferrite in the weld metal is reduced by decreased water temperature which results in a more rapid cooling rate. For optimal strength and toughness the microstructure that is most desired is that of acicular ferrite in the weld metal, with low percentages of grain boundary ferrite and no martensite.[Ref. 29] This data was taken from different sections of the same weldments. The UWW03 sample results may have been altered since the Welder/Diver noticed cracking after a few weld passes and ground it out, therefore, its thermal history is different from that of the other samples and the volume fraction of the microconstituents may have been altered. However, the acicular ferrite volume fraction of the samples for the fully grain refined regions clearly show a direct relationship with the water temperature.

The weld sample (UWW31) which was conducted in the highest water temperature (31°C or 88°F) resulted in the highest volume fraction of inclusions of both slag and oxide as shown in Table 4.4. In addition, it resulted in the most porosity, some of this porosity and slag inclusion are shown in Figure 4.19. The composition of the gases in the porosity has been reported to be very high in hydrogen, 62-82% H_2, 11-24% CO, 4-6% CO_2 and the remained consisting of N_2 and vapors from the rod and minerals[Ref. 29]. This argument indicates, again, as discussed above for the higher oxygen content, that diffusible hydrogen contents are likely to be less in higher temperature water; therefore, again lowering the likelihood of hydrogen assisted cracking. Some of the larger slag inclusions which were made up of a silicate matrix seemed to have Wustite dendrites (FeO) which would indicate that the oxygen levels in the weld metal had gotten to a quite high level.[Ref. 23] Figure 4.20 shows a possible example of one of these very large inclusion with wusitite dendrites. That the UWW31 weld sample had a higher oxygen content and therefore a lower hydrogen content seems to be proven with out having yet received the chemistry results.

Micrographs were made for the weld cap area of the UWW31 sample these can be correlated to the single pass weld schematic diagram presented in Figure 2.5. Furthermore, they were taken at the Vicker's hardness locations so the hardness can be correlated to the microstructure. The Subcritical HAZ (SCHAZ) region was subjected to a peak temperature below Ac_1, it exhibits a typical rolled steel ferrite (α) and Fe_3C microstructure the Vickers hardness was 240.1HV, this is seen in Figure 4.21. The Intercritical HAZ (ICHAZ) region was subjected to a peak temperature between Ac_1- Ac_3 the prior pearlite has transformed into austenite (γ) and expanded into the prior ferrite (α) grains upon heating above the Ac_1 temperature and then decomposed very fine ferrite (α) and pearlite grains upon cooling, the Vickers hardness was 289.3HV, this is seen in Figure 4.22. The Fine Grain HAZ (FGHAZ) region was subjected to a peak temperature just above the effective upper critical temperature (Ac_3) and below 1100°C, therefore, the austenite (γ) grains will nucleate and then decompose into fine ferrite and bainite grains since the cooling rate prohibits pearlite growth, the Vickers hardness was 429.0HV, this is seen in Figure 4.23. The Coarse Grain HAZ (CGHAZ) region was subjected to a peak temperature above the 1100°C and just below the melting point, therefore, the austenite (γ) grains will coarsen the resulted microstructure will be bainitic and martentisitic due to the high cooling rate, the Vickers hardness was 503.1HV, this is seen in Figure 4.24. Figure 4.25 shows the solid-liquid transition zone the martensite structure is giving way to a columnar grain microstructure, the Vickers hardness was 342.6HV. Figure 4.26 is in the weld metal and has a column grain microstructure, the Vickers hardness was 295.1HV. These figures clearly show the correlation between the weld microstructure and the microhardness for a single pass weld. This can be further seen in Figure 4.27 which is a overall view of the last pass of this weld.

While observing the HAZ of the UWW31 in the optical microscope an important discovery was made. The previous studies of these weld samples had reported that there was no cracking in the higher water temperature weldment. However, in this work, two very fine areas of cracking were noticed. Both areas were in the HAZ and both were on the left side of the weldment which is the same side on which the other (lower temperature) samples had extensive cracking. This seems to indicate that if the bead sequencing was adjusted then some stress relief would/could be expected. Two micrographs are shown in Figures 4.28 shows the upper crack in the fine HAZ near two Vicker's hardness readings (361.0 and 429.0) and Figure 4.29 shows the lower crack in the fine HAZ which seems to be intergranular in nature.

The traverse Vicker's readings were taken for each weld sample and then each sample was analyzed at the Vickers point since then the microstructure and the hardness could be correlated. The samples were as expected for a multipass weld and looked very similar to the schematic diagram discussed in Figure 2.6. The typical sequence of microstructure for the traverse Vicker's hardness sites are displayed in figures 4.30 through 4.32. The amount of slag and oxide inclusions are clearly visible and the microstructure is mostly acicular and bainitic in nature.

The UWW10 sample was welded in water temperature of 10°C (50°F). This weldment had two cracks on the left hand edge and these cracks seemed to start in the HAZ and continued into the weld metal. By looking at the macrograph Figure 3.3 it should be noted that the cracking was perpendicular to the direction of maximum tensile stress resulting from cool down. Figures 4.33 and 4.34 were taken in dark field with a blue filter to show these cracks. The cracking progressed into the weld metal both times along the columnar grains and at the junction of the two CGHAZ weld passes.

The UWW03 sample was welded in water temperature of 2.8°C (37°F). This weldment had cracking over two thirds of the height of the weld. By looking at the macrograph in Figure 3.2 it is seen that the cracking progressed along the HAZ and at times did progress into the weld metal. The micrographs presented in Figures 4.35 through 4.39 were taken in dark field with a blue filter, the weld metal is at the top of the micrograph with the HAZ at the bottom. They show that when the cracking did progress into the weld metal the cracking appeared to follow the columnar grain structure in the fusion zone. Furthermore, note that the cracking seems to step in a zig zag motion from the tougher weld metal back into the brittle HAZ as the cracking progressed up the weld. In the next section the fracture surface of this cracking will be described.

3. Fractography

The SEM was used after the UWW03 weld sample was sectioned and the fracture surface was exposed. Unfortunately the weld samples were old and the cracking had progressed completely to the surface and saltwater had gotten into the crack. Furthermore, when the weld was etched and then ultrasound cleaned some etchant had been trapped in the cracks. This meant that the crack surfaces were difficult to examine. However, the results did seem to indicate that the cracking was transgranular in nature and that there was secondary cracking which progressed perpendicularly to the fracture surface[Ref. 39]. Figure 4.40 and 4.41 shows the transgranular cracking and secondary cracking from the fracture surface. On the fracture surface that progressed into the weld metal the surface appears differently since the cracking appeared to follow the columnar grains in the weld metal. The surface of the large peninsula seen in Figure 4.36, for example, has horizontal marks on the fracture surface parallel with the crack face which could indicate a temporary arresting point in the cracking, this is seen in Figure 4.42.

V. SUMMARY

A. CONCLUSIONS

For the underwater welds studied the weldment cracking was directly related to the water temperature. The elements for hydrogen assisted cracking were all present: (1) hydrogen availability from the dissociation of H_2O, (2) weldment restraint resulting in high tensile stresses, (3) susceptible microstructure and (4) a relatively low temperature combined with a very rapid cooling rate. In addition the base metal was on the border line of being difficult to weld on the modified Graville diagram.

There was fine cracking found even in the highest water temperature sample (UWW31). The difference in the water temperature range was about 30°C, this is very small when compared to the CGHAZ temperature range from 1100°C to the melting point near 1800°C. Therefore, the cooling rate difference would not be expected to be very great between the three samples. In fact, Tsai, et al., [Ref. 25] calculated this to be the case as seen in Figure 2.7. The cause of cracking would therefore appear to be hydrogen assisted with more diffusible hydrogen apparently available for lower water temperatures. The amount of slag and oxide inclusions present in the UWW31 sample may have aided in limiting the hydrogen diffusion from the weld metal and into the CGHAZ region. Because there were fewer inclusions in the lower temperature weldments this could have resulted higher diffusible hydrogen levels in the CGHAZ leading to the massive cracking of this region as seen, for example, in the UWW03 sample Figure 3.2 and Figures 4.35 to 4.39.

B. RECOMMENDATIONS

Further testing should be started as outlined in subtask E of the scope of present work: cracking tests should be conducted to determine the influence of changing water temperature from approximately 10°C to approximately 30°C on cracking susceptibility.

The welding of the samples should be carefully controlled and the diffusible hydrogen and oxygen levels determined as soon as possible after the weldments are completed. Furthermore, since the change in depth is so critical over the range at which normal ship repairs are made the first round of testing for diffusible hydrogen levels should be made at a very shallow depth maybe only 1 meter. Thus, the additional factor of partial pressure difference during the diffusional off-gas of the hydrogen would not be a factor and a data point could be collected and the measurement techniques for the diffusible hydrogen could be adjusted before further testing is completed at normal repair depths of 10 meters.

In addition any samples which exhibit cracking should be sectioned and fractographic analysis of the fracture surface should be made before corrosion and or handling can damage the surface. The objective should be toward identifying more indications of hydrogen induced cracking such as "fish-eyes".

ELEMENTS Wt%	**Weld Metal w/o BS 6/10/97**	**Weld Metal w/ BS 6/10/97**	**Hobart E7014 Filler Rod 5/30/97**	**Hobart E7014 Flux 5/30/97**	**BROCO CS-1 Coating 5/30/97**
Sodium	-	-	-	5.94	-
Magnesium	-	-	-	5.28	-
Aluminum	0.03	0.03	-	18.72	73.65
Silicon	0.10	1.01	0.29	37.04	26.35
Phosphorus	0.01	0.01	0.07	-	-
Sulfur	0.01	0.03	0.04	-	-
Potassium	-	-	-	3.95	-
Calcium	0.11	0.04	-	1.23	-
Titanium	0.08	0.03	-	14.25	-
Manganese	0.51	0.32	0.41	1.01	-
Iron	99.15	98.52	99.19	12.58	-

Table 4.1 Weld metal, Filler rod, and Flux/coating EDX chemical composition analysis.

Type	**Average Number Incl/Field**	**Average Diameter (μm)**	**Standard Deviation (μm)**	**99% Confidence (μm)**	**Volume fraction %**
Oxide	6.600	0.49837	0.33017	0.04680	**0.844**
Slag	0.940	2.25168	1.68254	0.63197	**2.452**
Total	7.540	0.71695	0.88209	0.11698	**1.994**

Table 4.2 Inclusion statistics and volume fraction, UWW03.

Type	**Average Number Incl/Field**	**Average Diameter (μm)**	**Standard Deviation (μm)**	**99% Confidence (μm)**	**Volume fraction %**
Oxide	7.120	0.49275	0.31492	0.04298	**0.890**
Slag	0.780	1.82223	2.01830	0.83221	**1.333**
Total	7.900	0.62402	0.79995	0.10364	**1.583**

Table 4.3 Inclusion statistics and volume fraction, UWW10.

Type	**Average Number Incl/Field**	**Average Diameter (μm)**	**Standard Deviation (μm)**	**99% Confidence (μm)**	**Volume fraction %**
Oxide	7.860	0.49025	0.32952	0.04280	**0.972**
Slag	3.080	1.29088	1.71664	0.35620	**2.641**
Total	10.940	0.71565	1.01667	0.11193	**2.883**

Table 4.4 Inclusion statistics and volume fraction, UWW31.

Averages /Sample	Base Metal	HAZ Left Toe	HAZ Left Middle	Fusion Zone	HAZ Right Middle	HAZ Right Toe
UWW03:						
Max	212.2	342.6	**447.1**	259.5	372.5	326.5
Ave	175.4	316.2	315.6	248.5	326.7	288.0
Min	163.0	287.7	273.1	226.6	273.1	254.8
UWW10:						
Max	206.3	370.2	355.4	268.7	**397.3**	309.7
Ave	176.6	321.0	322.5	250.6	356.2	293.3
Min	165.0	271.6	283.8	226.6	274.6	274.6
UWW31:						
Max	200.5	343.6	366.7	296.7	**429.0**	323.6
Ave	186.9	309.5	334.5	267.8	366.5	293.6
Min	168.2	283.0	308.0	236.5	343.6	250.2

Table 4.5 Weld Sample Vicker's Hardness Data.

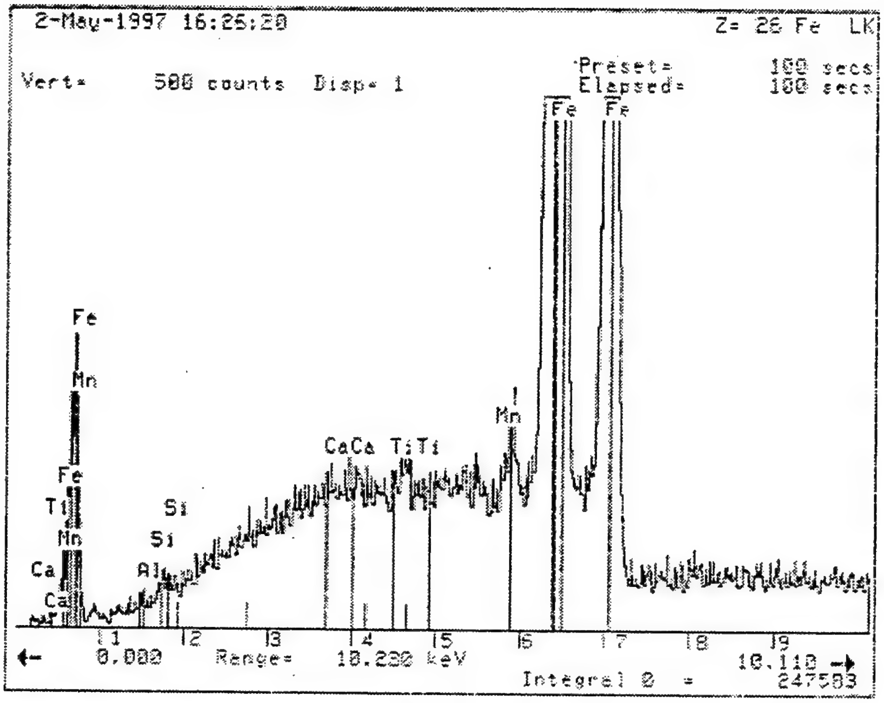

(a)

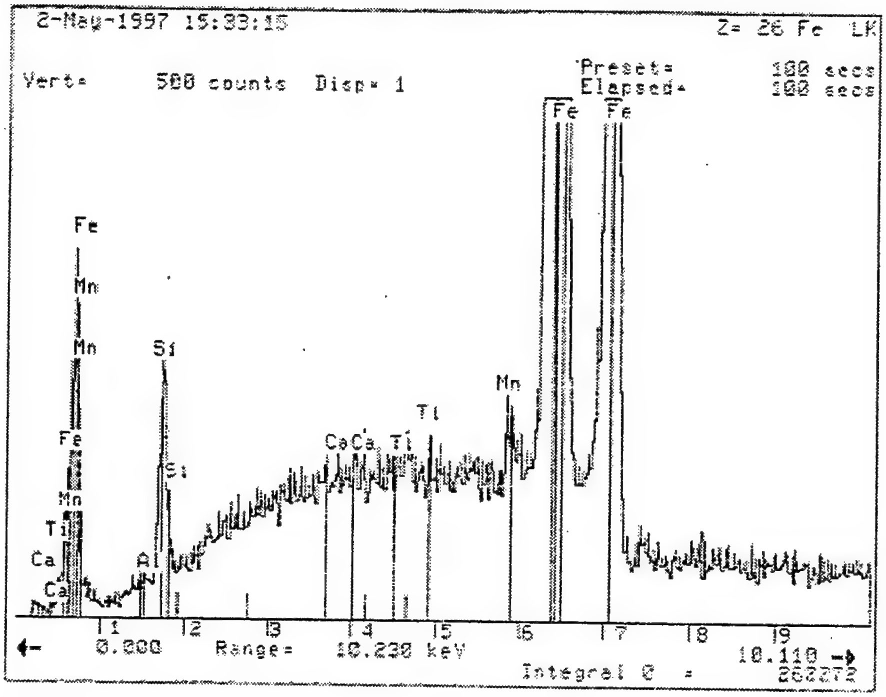

(b)

Figure 4.1 (a) Typical Weld Metal EDX Spectrum, without backscatter detector in place.
(b) Typical Weld Metal EDX Spectrum, with backscatter detector in place.
Note the high Si intensity peak.

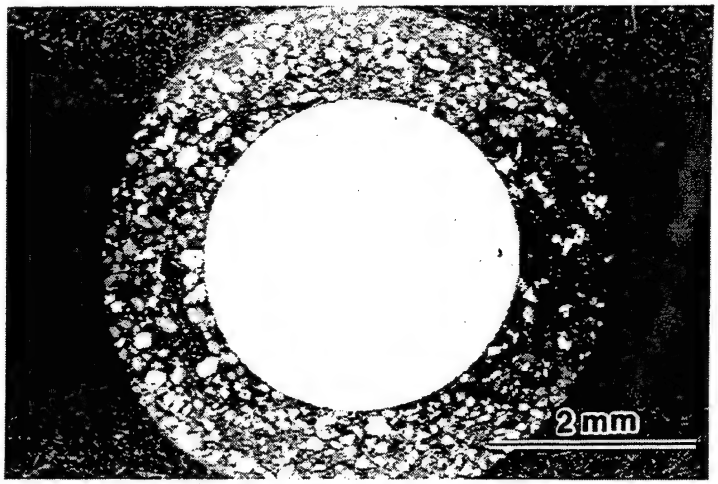

Figure 4.2 SEM Micrograph of BROCO CS-1 Cross-section.

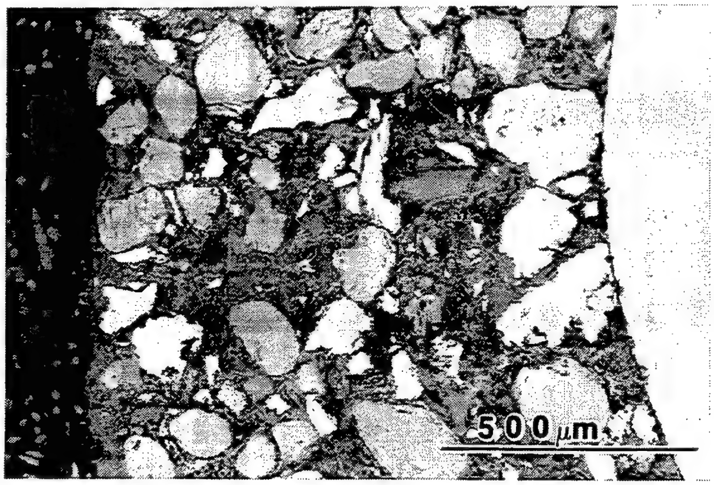

Figure 4.3 SEM Micrograph of BROCO CS-1 Flux.

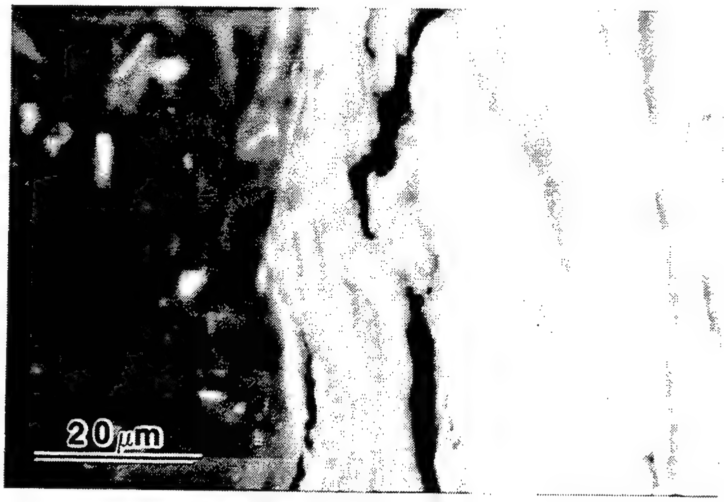

Figure 4.4 SEM Micrograph of BROCO CS-1 Special coating.

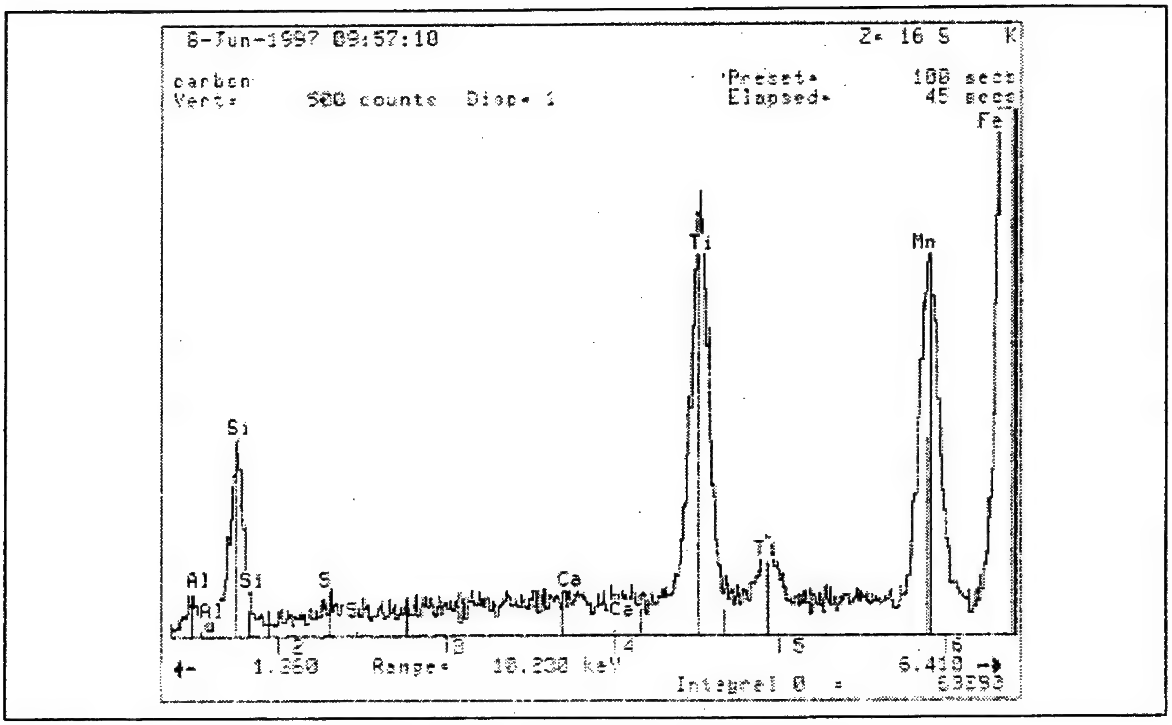

Figure 4.5 Typical Oxide Inclusion EDX Spectrum.

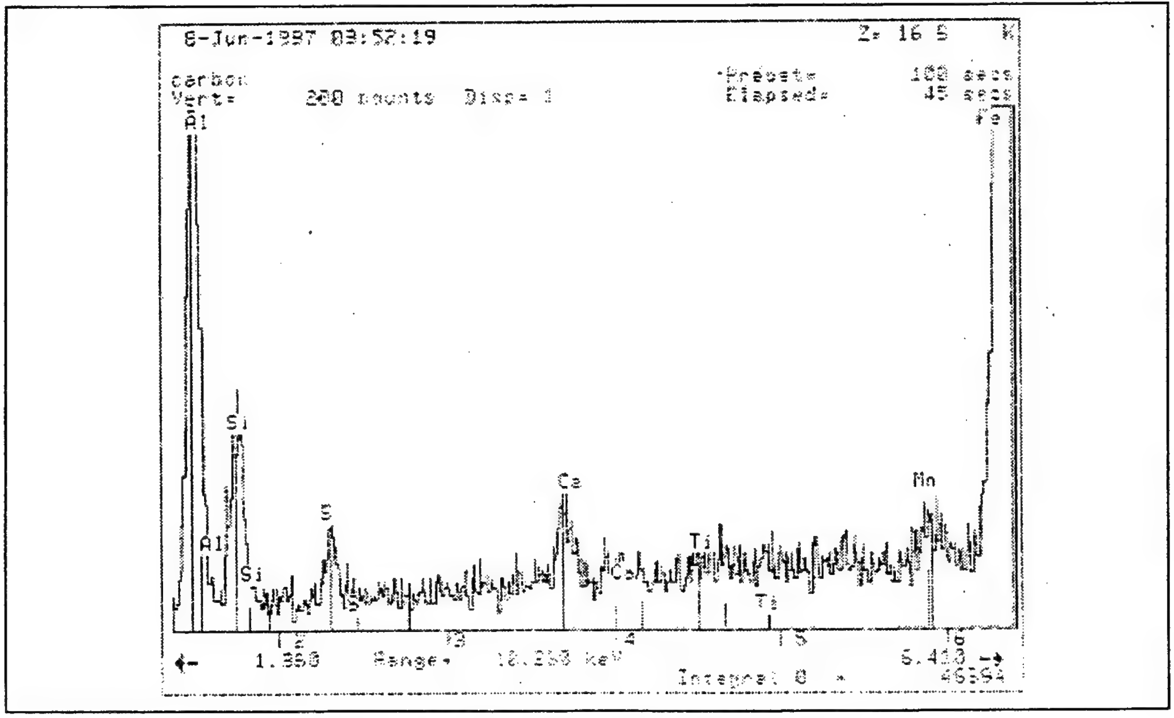

Figure 4.6 Typical Slag Inclusion EDX Spectrum.

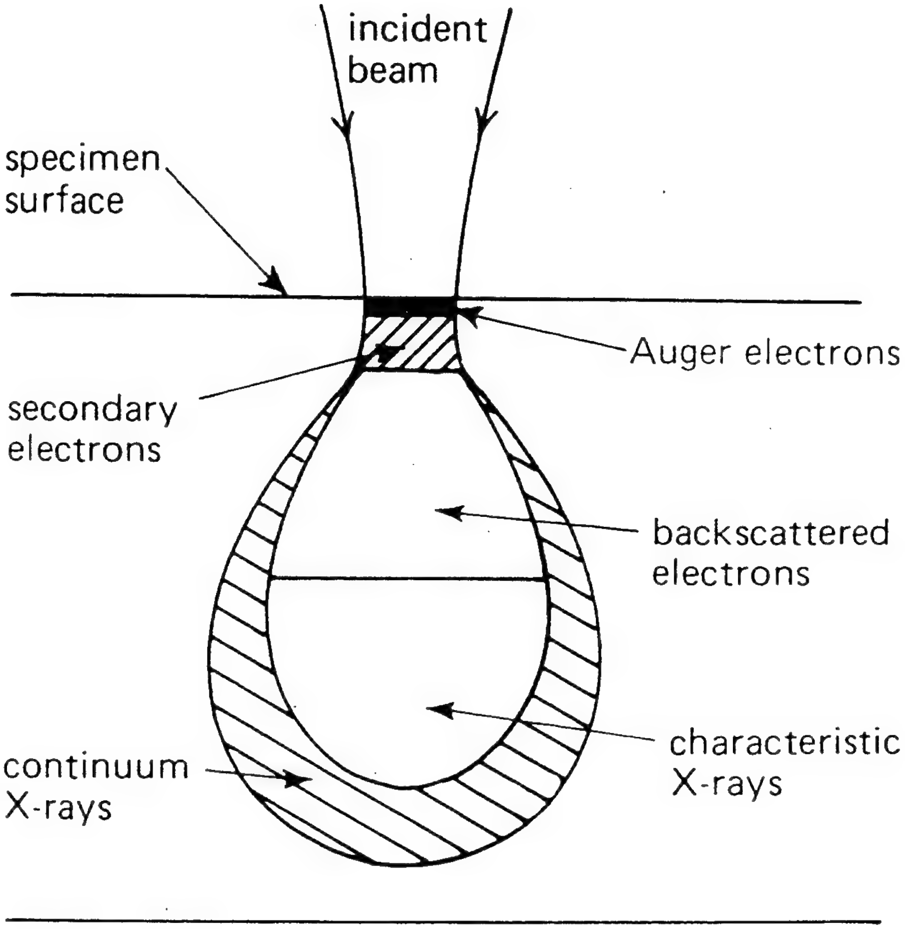
incident
beam
specimen
surface
Auger electrons
secondary
electrons
backscattered
electrons
characteristic
X-rays
continuum
X-rays

Figure 4.7 Schematic diagram showing generation of electrons & x-rays with in the specimen. [Ref. 31]

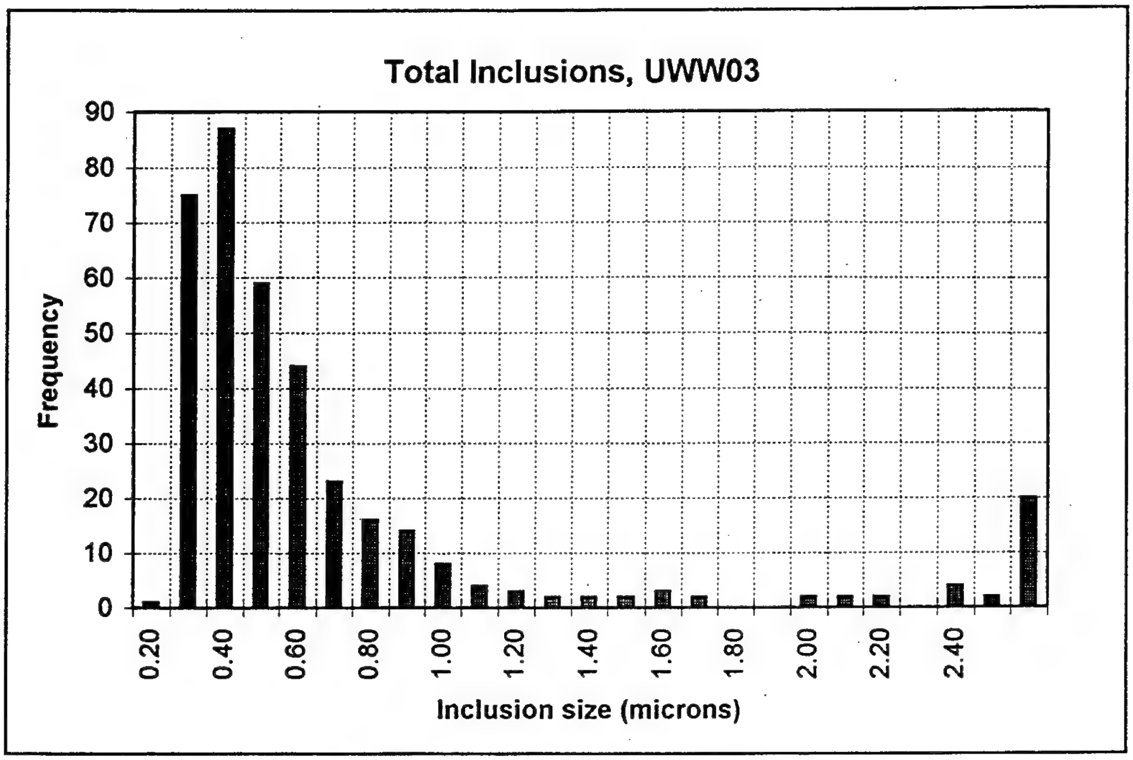

Figure 4.8 UWW03 Total Inclusion Distrubution.

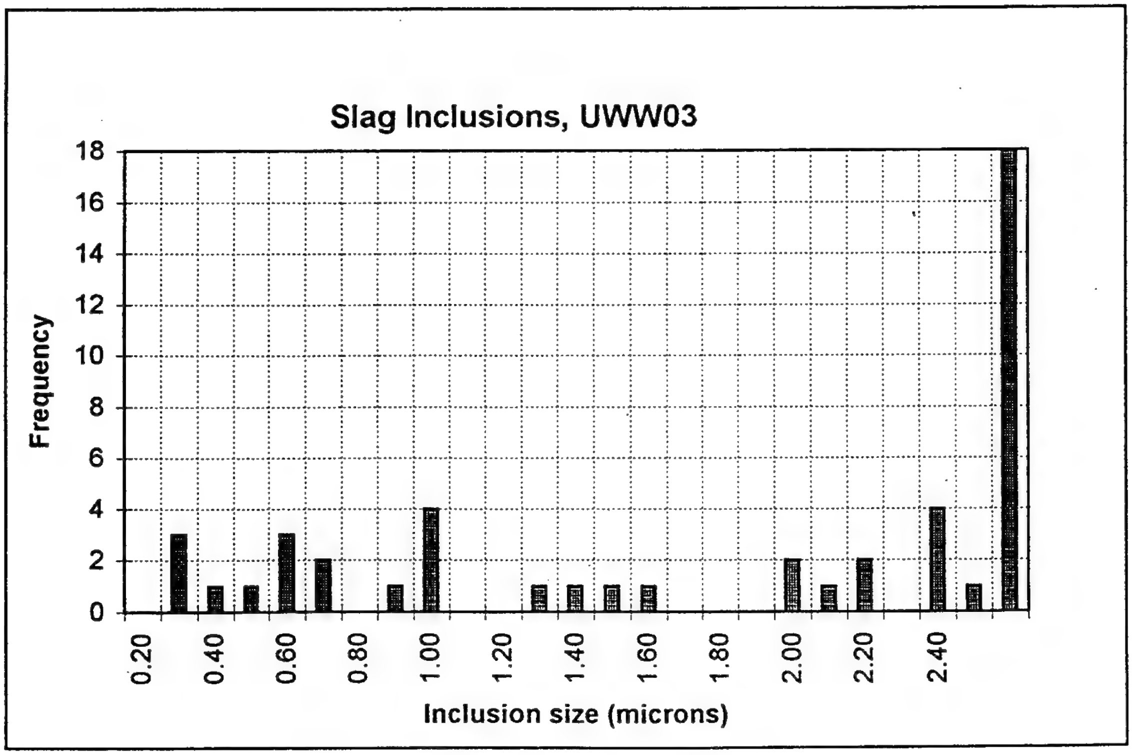

Figure 4.9 UWW03 Slag Inclusion Distrubution.

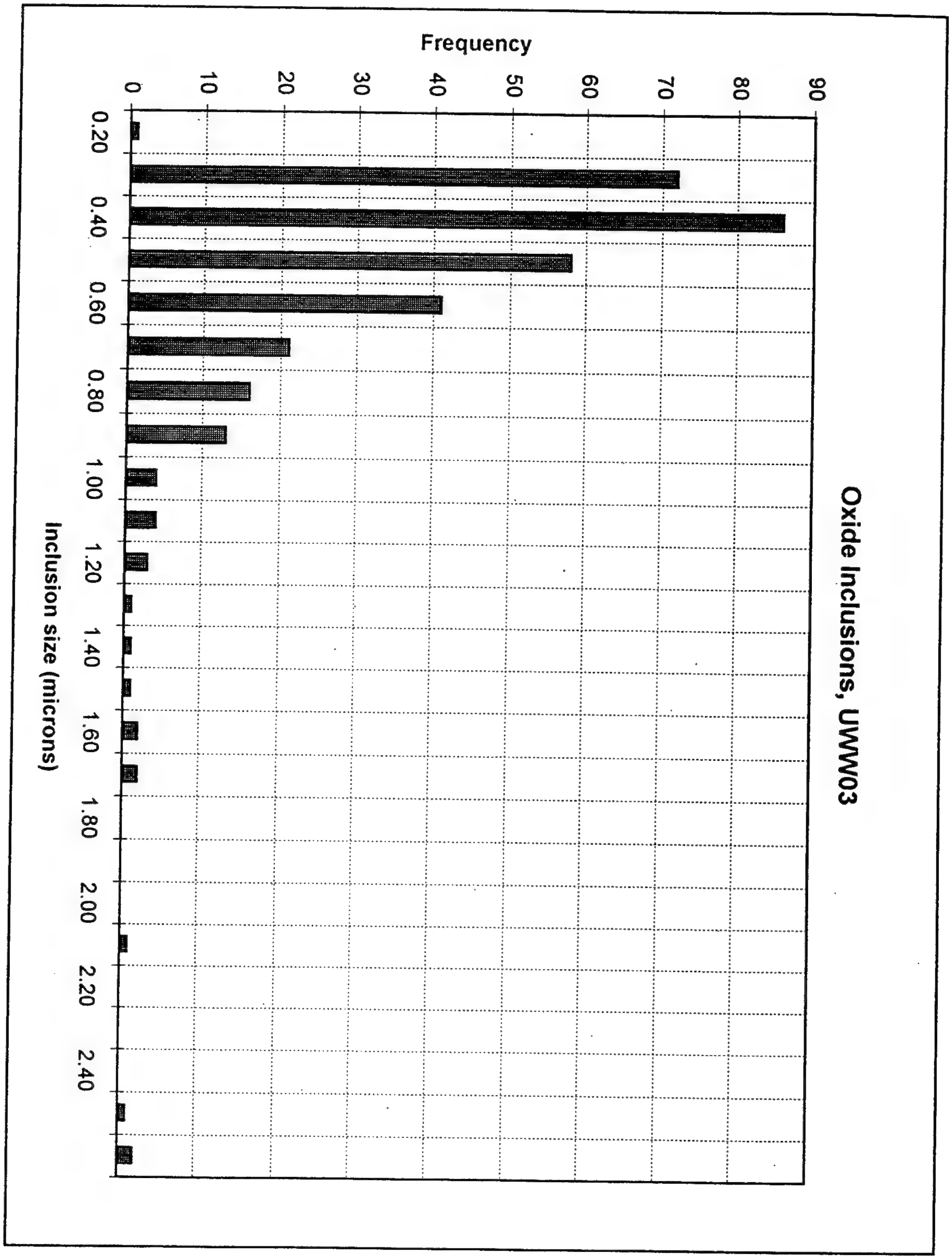

Figure 4.10 UWW03 Oxide Inclusion Distrubution.

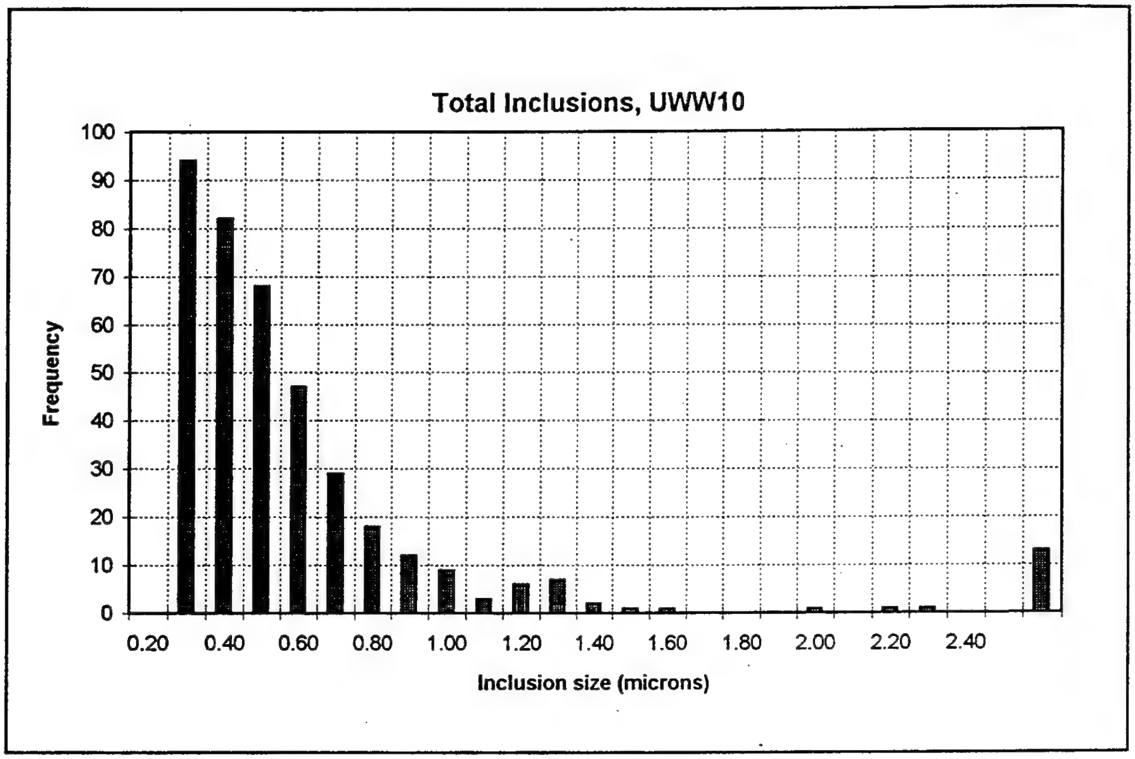

Figure 4.11 UWW10 Total Inclusion Distrubution.

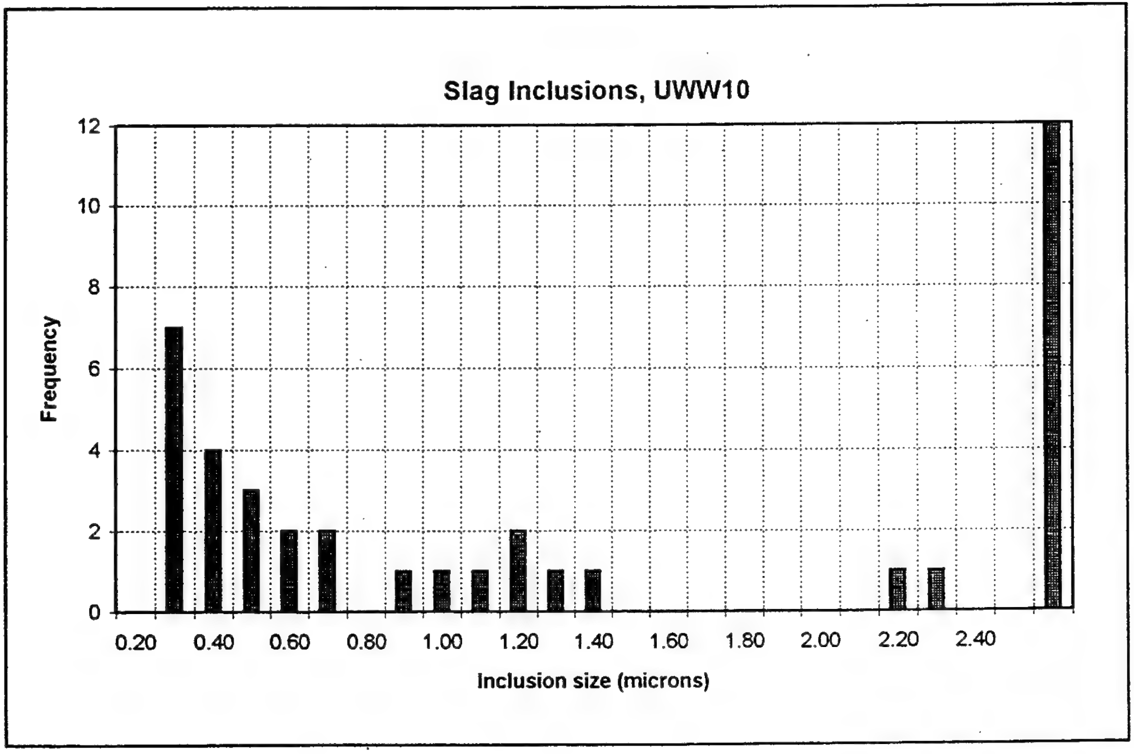

Figure 4.12 UWW10 Slag Inclusion Distrubution.

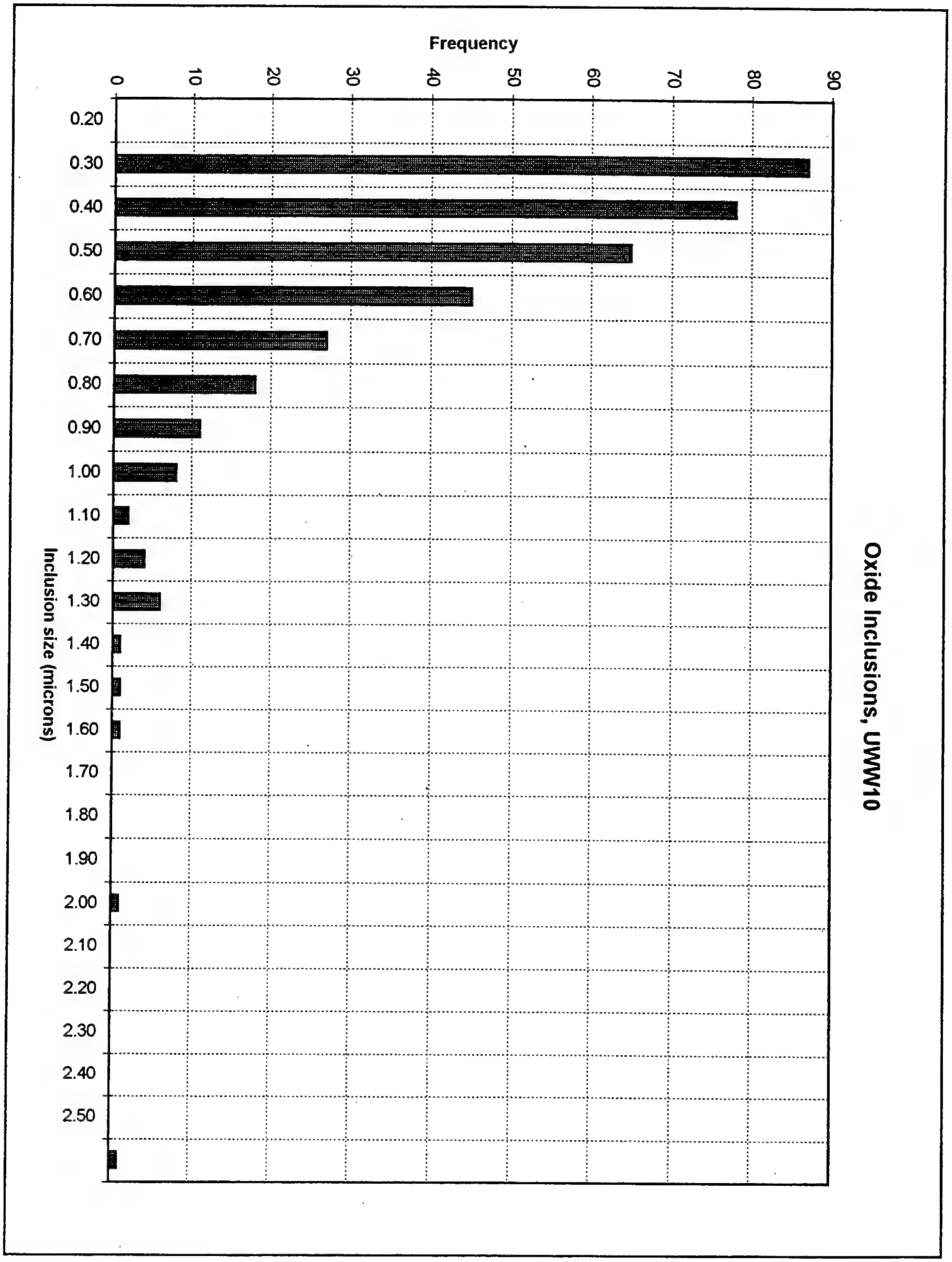

Figure 4.13 UWW10 Oxide Inclusion Distrubution.

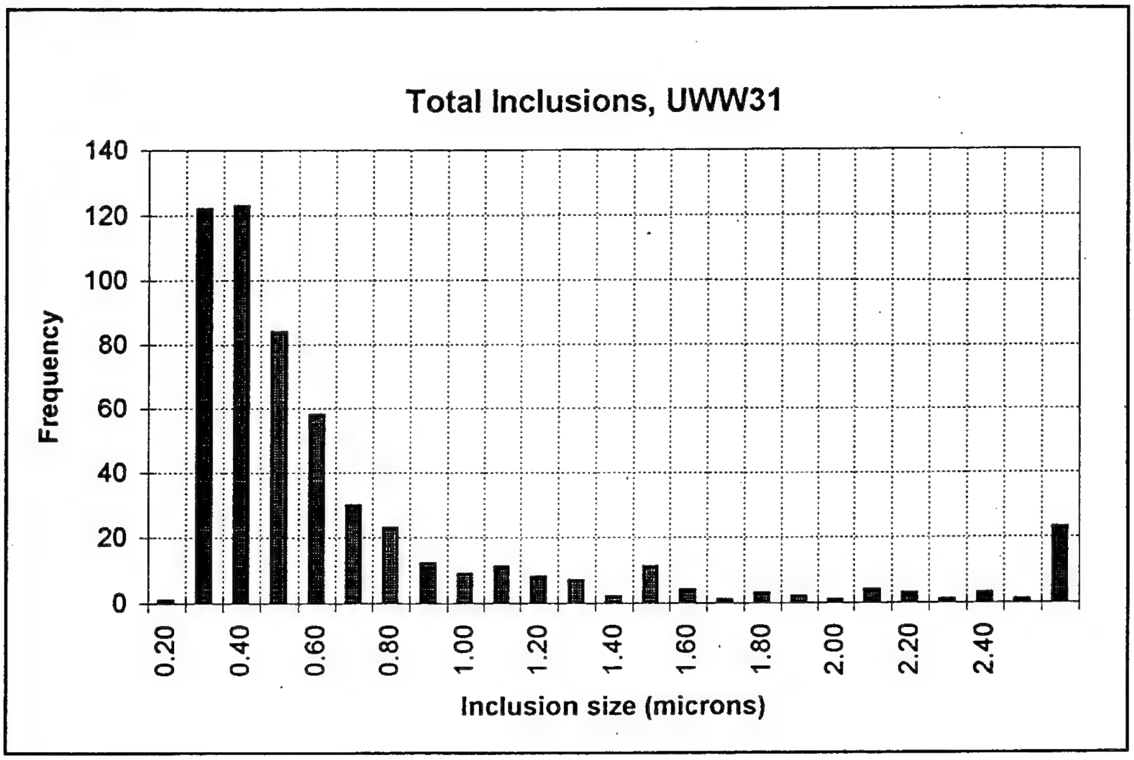

Figure 4.14 UWW31 Total Inclusion Distrubution.

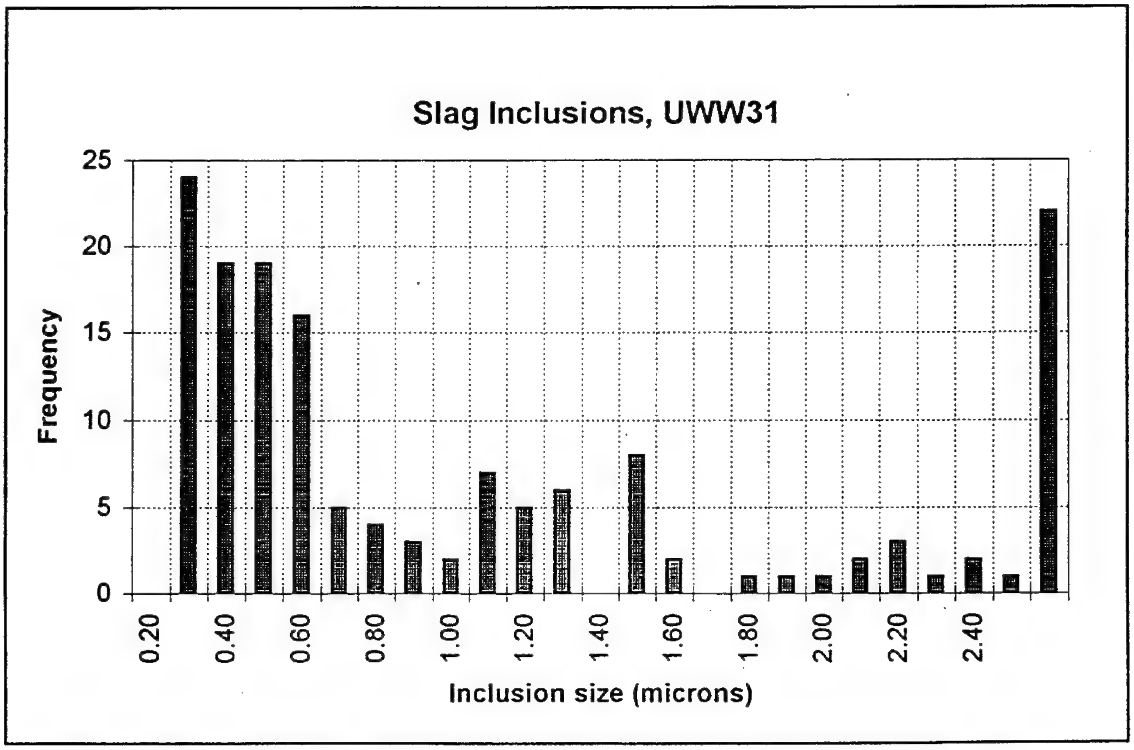

Figure 4.15 UWW31 Slag Inclusion Distrubution.

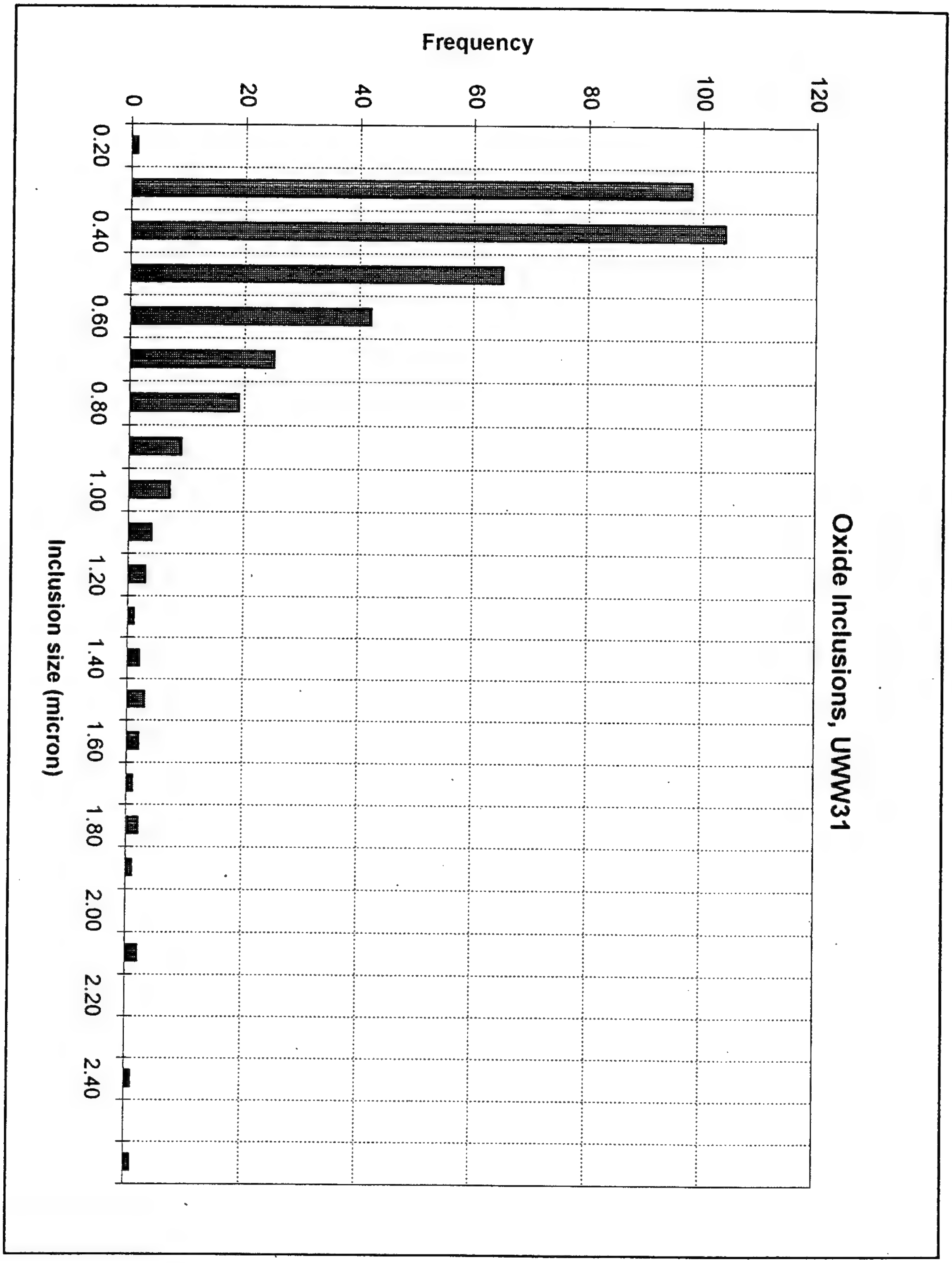

Figure 4.16 UWW31 Oxide Inclusion Distrubution.

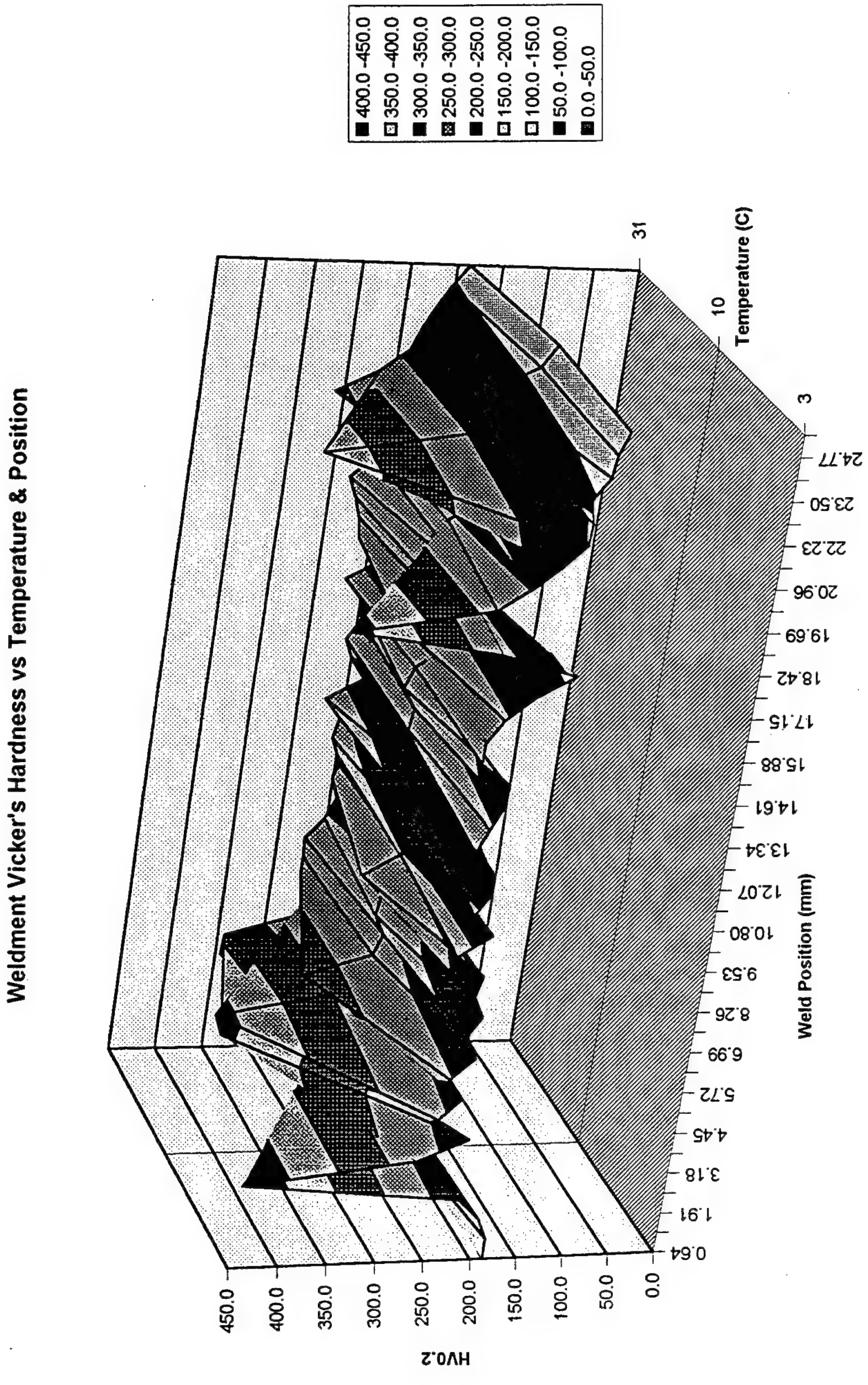

Figure 4.17 Traverse Vicker's Hardness for Mid-section of each Weldment

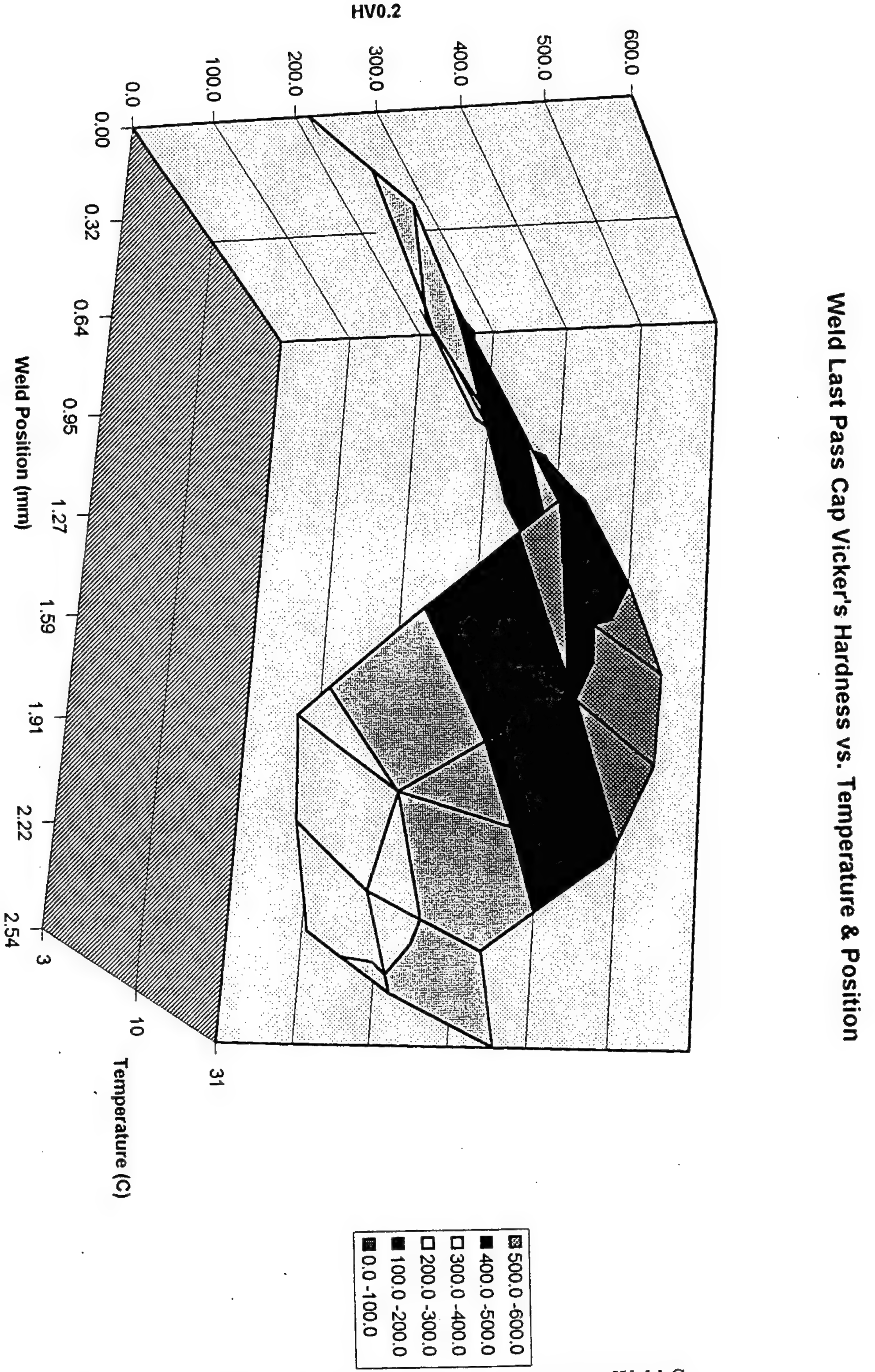

Figure 4.18 Traverse Vicker's Hardness for the Last Pass Weld Cap.

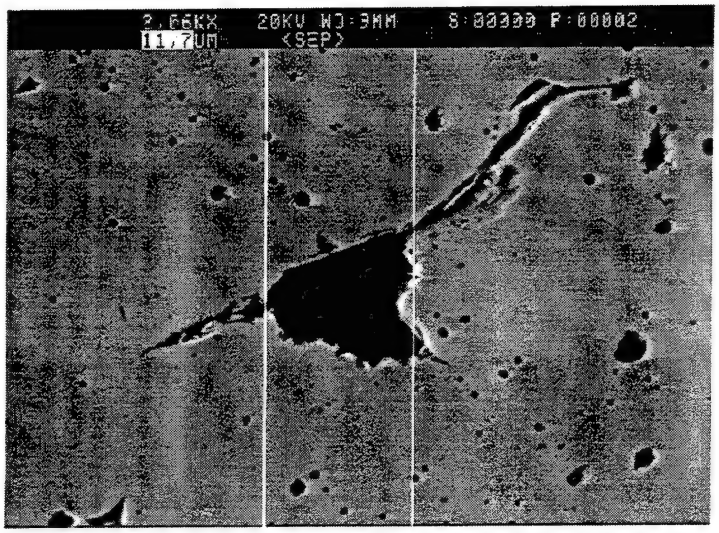
2.66KX 20KV WD:3MM S:00300 P:00002
11.7UM <SEP>

Figure 4.19 Porosity and Slag seen in UWW31 weld sample.

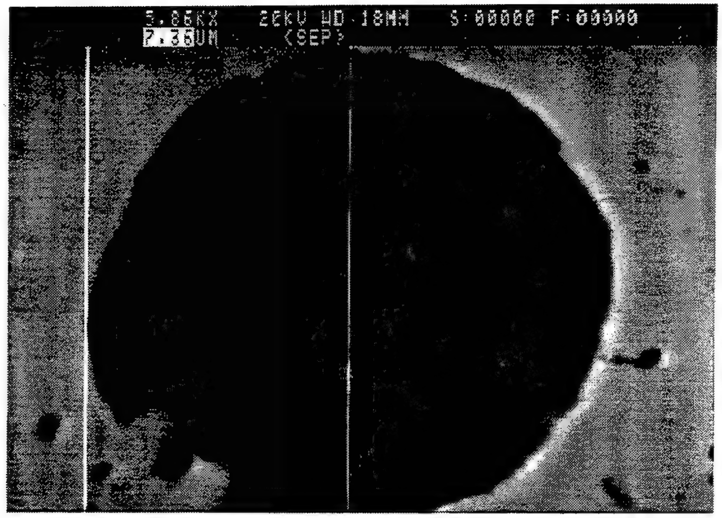
3.86KX 20KV WD:18MM S:00000 F:00000
7.36UM <SEP>

Figure 4.20 Large silicate matrix slag inclusion with Wustite dendrites (FeO).

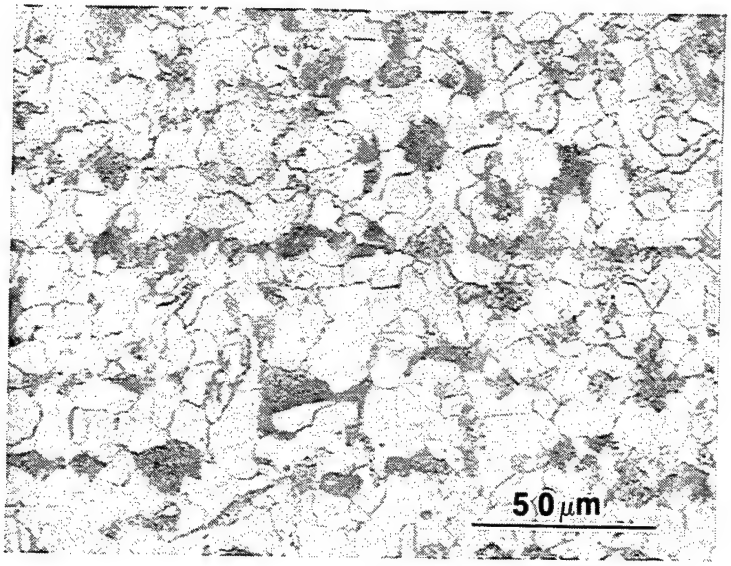

Figure 4.21 Subcritical HAZ, 240.1HV.

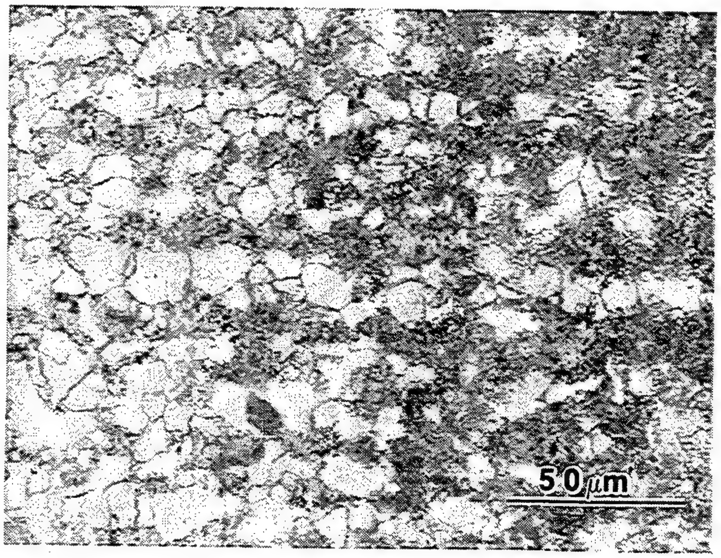

Figure 4.22 Intercritical HAZ, 289.3HV.

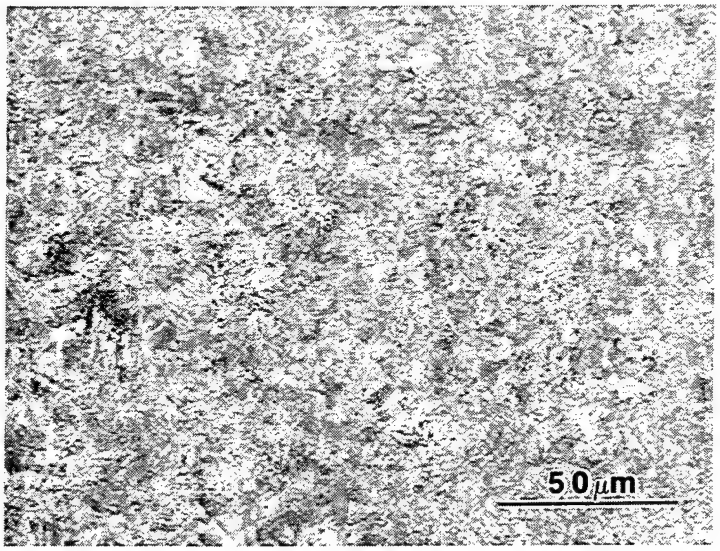

Figure 4.23 Fine Grain HAZ, 429.0HV .

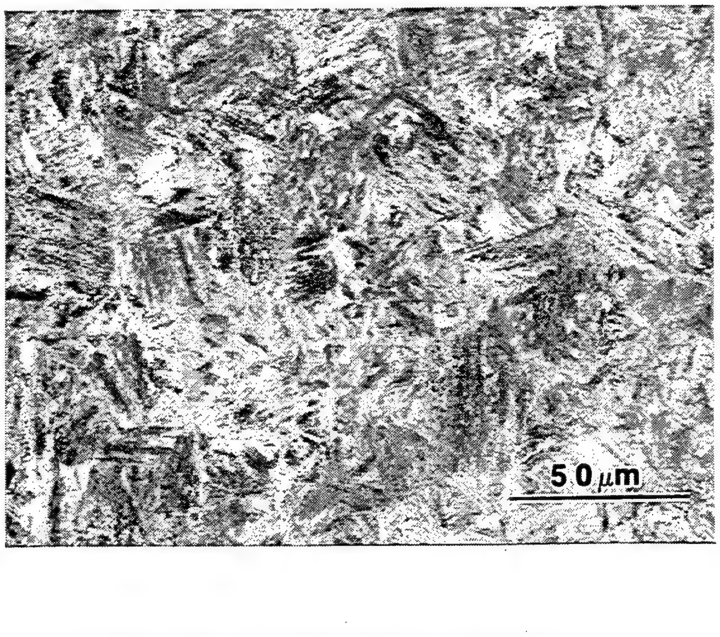

Figure 4.24 Coarse Grain HAZ, 503.1HV .

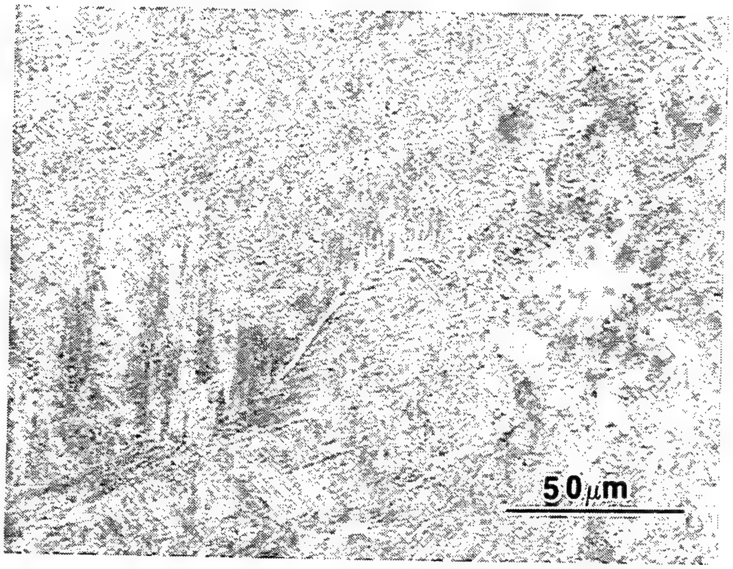

Figure 4.25 Solid-Liquid Transition Zone, 342.6HV.

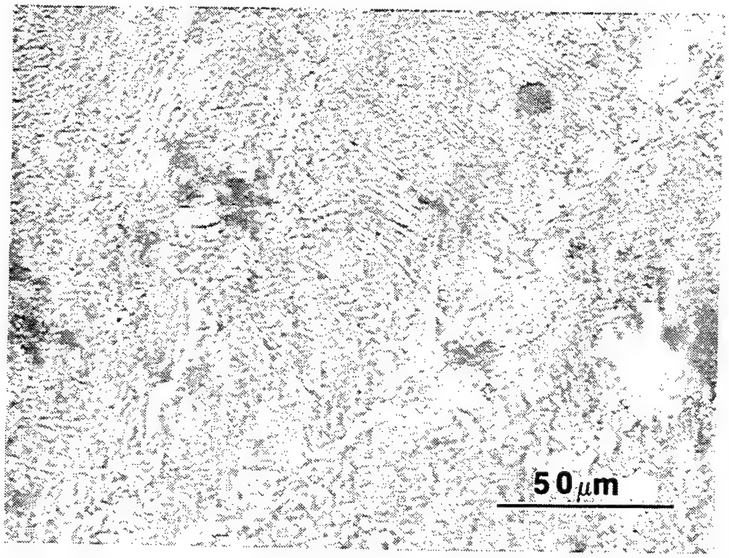

Figure 4.26 Columnar Grain FZ, 295.1HV.

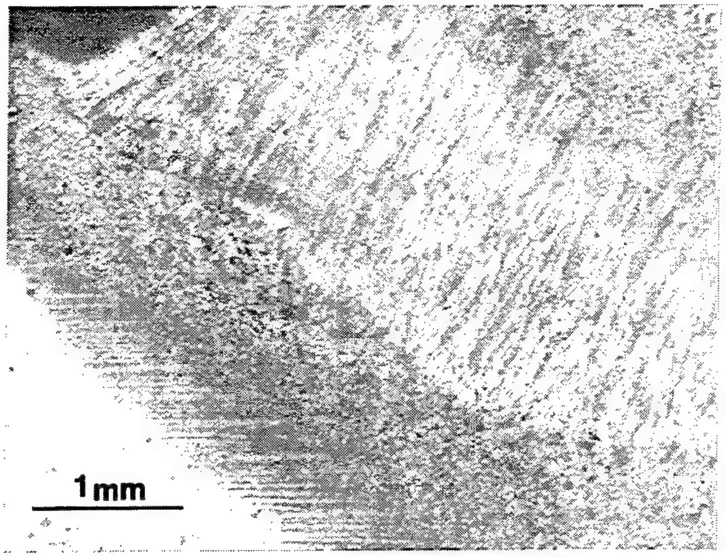

Figure 4.27 Overall View of the Last Pass of UWW31.

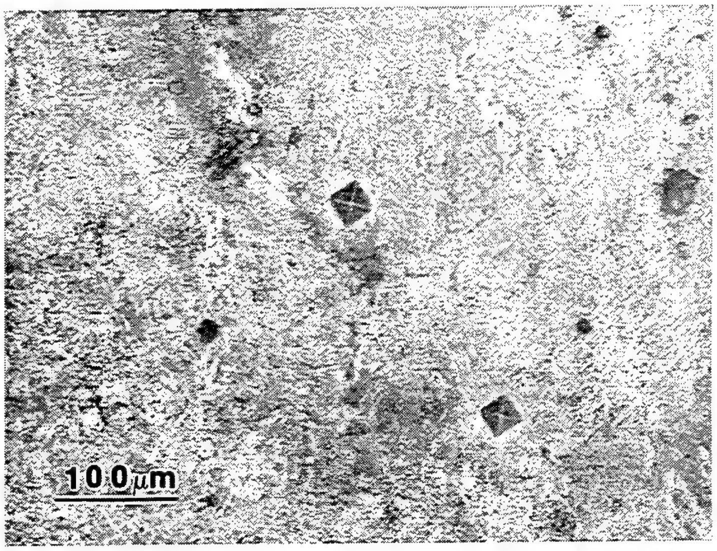

Figure 4.28 Fine HAZ cracking, near Vicker's hardness readings on the left side near the mid-section of UWW31 (See Figure 3.4).

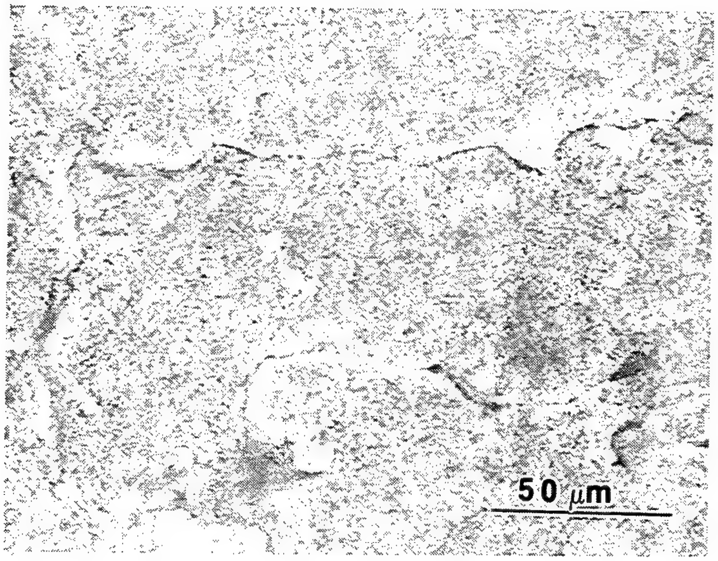

Figure 4.29 Fine HAZ cracking on the left side near the lower section of UWW31 (See Figure 3.4).

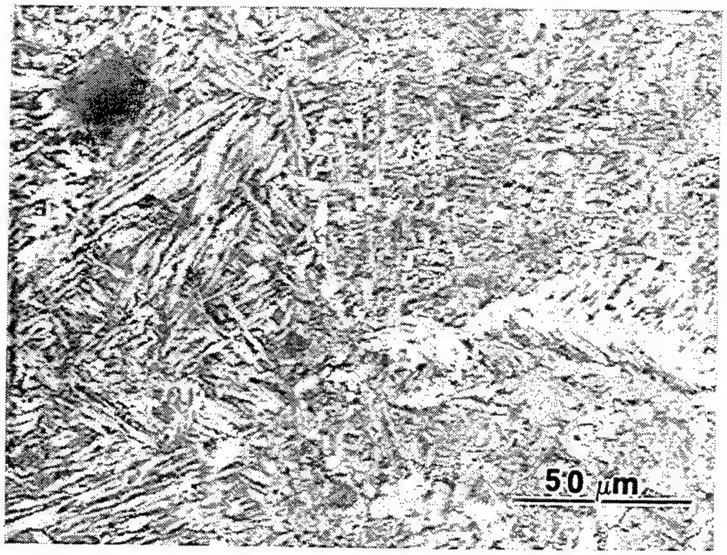

Figure 4.30 Edge of Fusion zone, 273.1 HV.

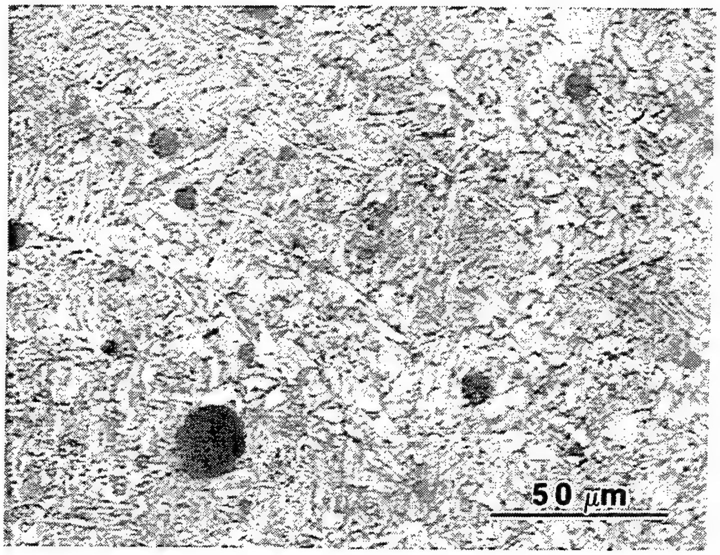

Figure 4.31 Weld metal field with large slag inclusions and smaller inclusions with acicular ferrite, 257.3 HV.

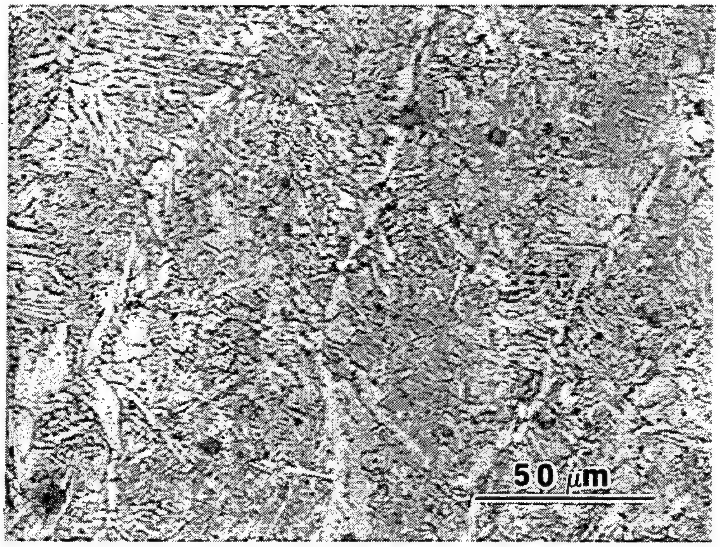

Figure 4.32 Columnar grain structure with widmanstatten ferrite and acicular ferrite, 227.7HV .

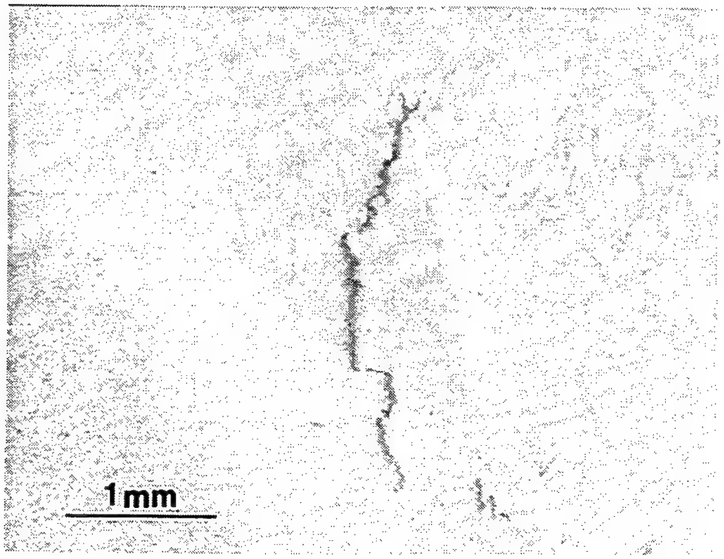

Figure 4.33 Upper crack in UWW10 weld sample from HAZ into the weld metal (See Figure 3.3).

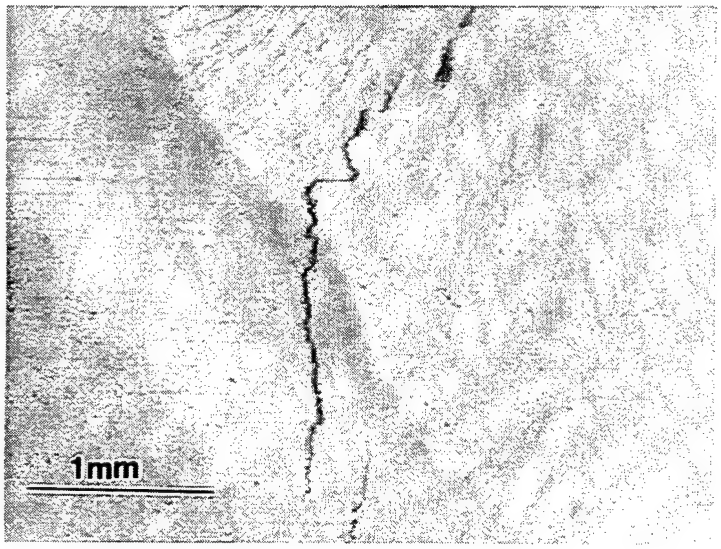

Figure 4.34 Lower crack in UWW10 weld sample from HAZ into the weld metal (See Figure 3.3).

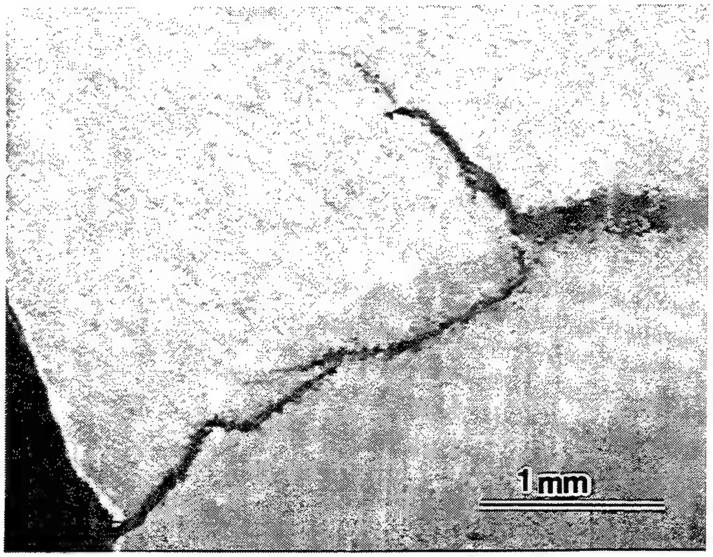

Figure 4.35 Underbead cracking from top of weld. UWW03

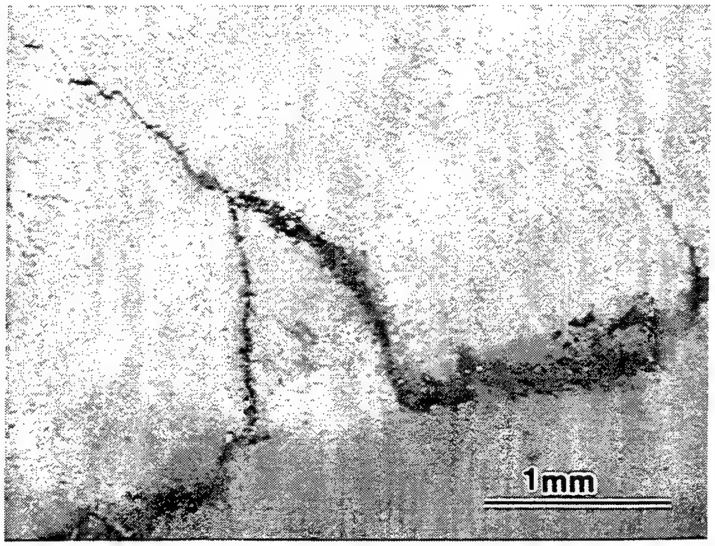

Figure 4.36 Underbead cracking sceond from top. Cracking progressed into the weld metal along the columnar grains. Note the subsequent pass HAZ within the weld metal. UWW03

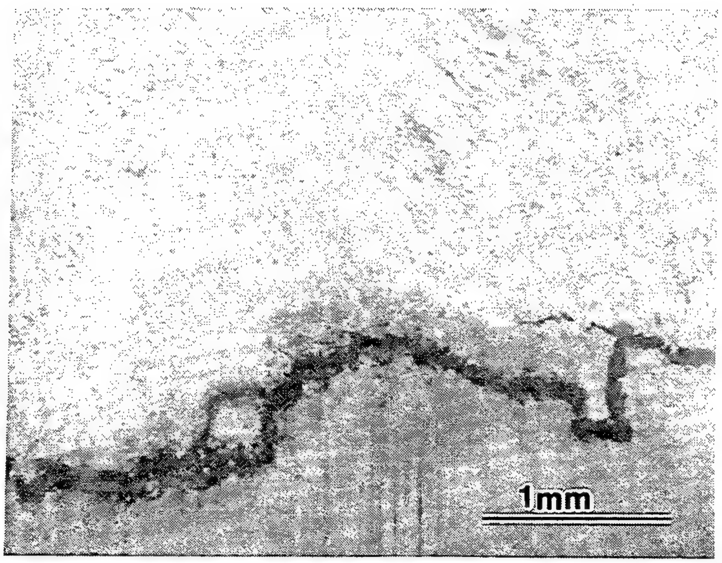

Figure 4.37 Underbead cracking third from top. UWW03

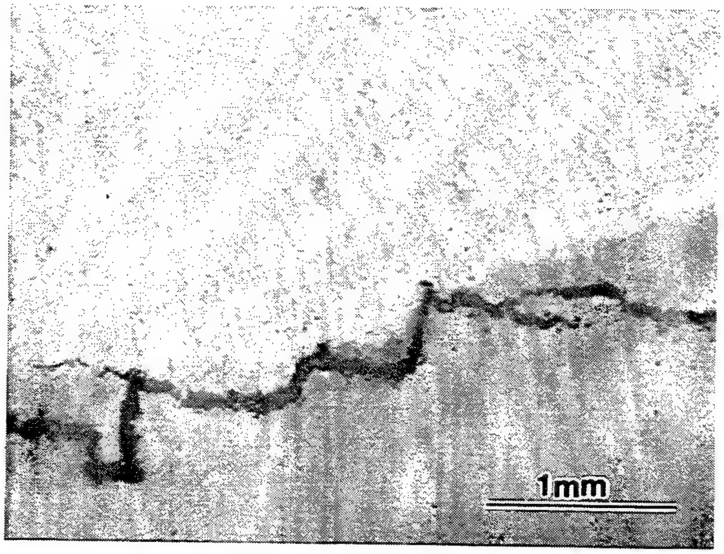

Figure 4.38 Underbead cracking fourth from top. The crack steps along the fusion line between the weld metal and the HAZ. UWW03

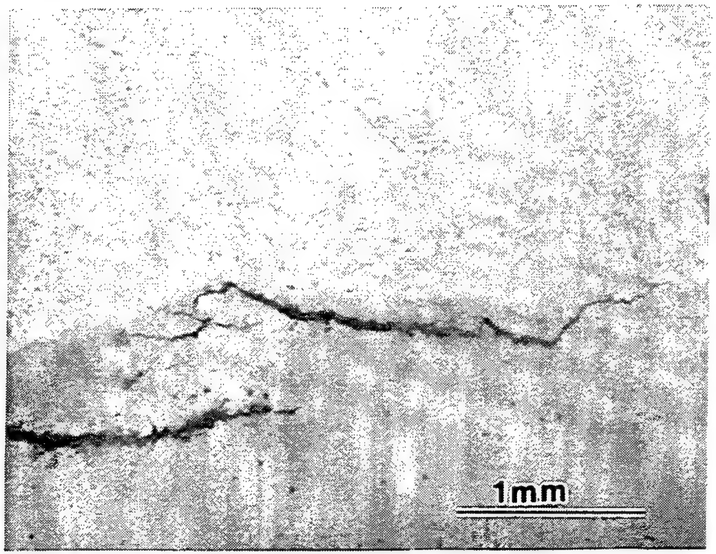

Figure 4.39 Underbead cracking fifth from top. UWW03

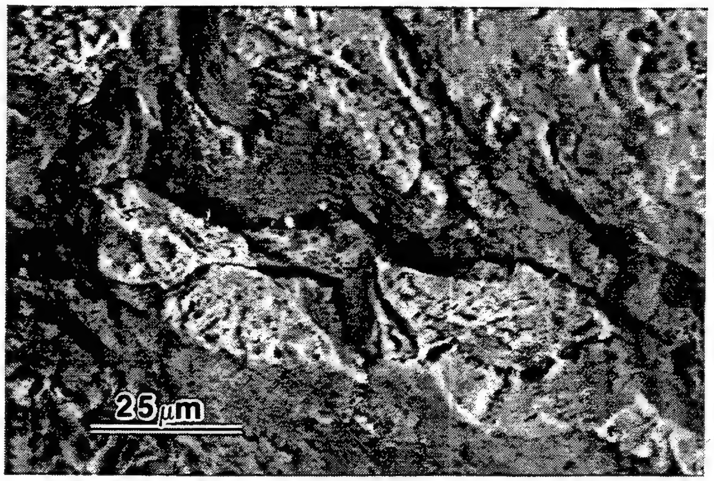

Figure 4.40 SEM of transgranular cracking on the surface of the fracture with secondary cracking.

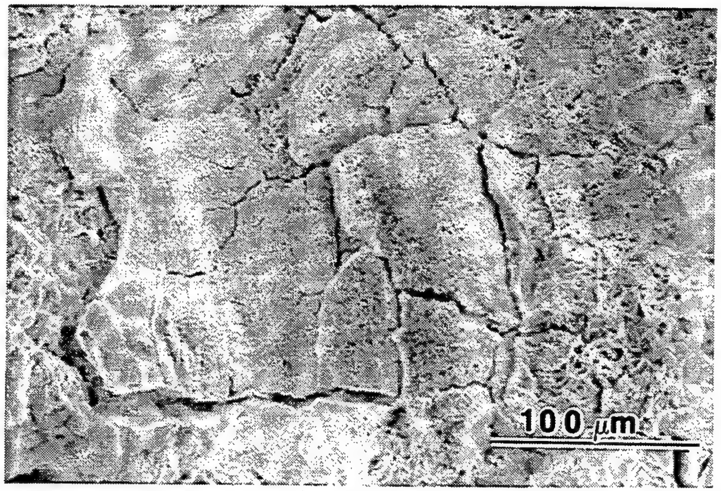

Figure 4.41 SEM of transgranular cracking on the surface of the fracture with secondary cracking.

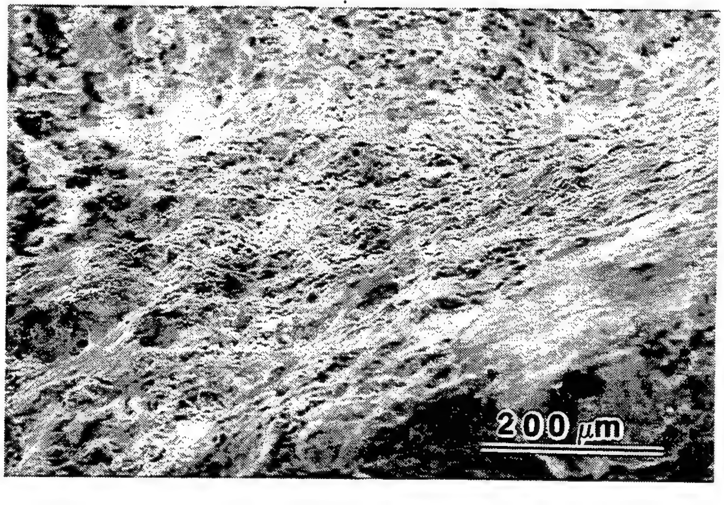

Figure 4.42 SEM of fracture surface that progressed into the weld metal as seen in Figure 4.36.

LIST OF REFERENCES

1. AWS Committee on Welding in Marine Construction, "Specification for Underwater Welding", *American Welding Society* (ANSI/AWS D3.6-93), August, 1992.

2. Ogden, D. and T. Joos, "Specification Stirs Underwater Electrode Development", *Welding Journal*, vol. 69, no. 8, pp. 59-61, 1990.

3. West, T.C., G. Mitchell and E. Lindberg, "Wet Welding Electrode Evaluation for Ship Repair", *Welding Journal*, vol. 69, no. 8, pp. 46-56, 1990.

4. West, T.C., W.E. Mitchell and R.I. Murray, "Effects of Water Temperature on Cracking of Wet-Welded Carbon Steel", *Welding Journal*, vol. 75, no. 10), pp. 51-55, 1996.

5. Silva, E.A., "Underwater Welding and Cutting", *Metals Handbook*, 9th Edition, vol. 6, American Society of Metals, 1983.

6. Boie, H., K. Schmidt and W. Schnelgelsberg, "Welding Pollution Within the Atmosphere of an Underwater Simulator", *20th Annual Offshore Technology Conference*, OTC 5816, Houston, TX, 1988.

7. Brown, R.T. and K. Masubuchi, "Fundamental Research on Underwater Welding", *Welding Journal*, vol. 54, no. 6, pp. 178s-188s, 1975.

8. Grubbs, C.E., "Underwater Wet Welding: A State of the Art Report", *OMAE 1993*, vol. III, part A, pp. 111-118, ASME, New York, 1993.

9. Lythall, D.J. and B.E. Pinfold, "New Underwater Welding Process Proved for Continental Shelf Depths", *9th Annual Offshore Technology Conference* , OTC 2857, Houston, TX, 1977.

10. Barnett, CDR Eben E., II, "Navy Maintenance Support - Why Three Levels?", *Naval Engineers Journal* , p. 92, March 1993.

11. Wright, Steven, Chief Engineer, CNSY C-240, conversation on November 22, 1993.

12. Malley, VADM Kenneth C., "The Response", *Naval Engineers Journal* (July 1993), p. 43.

13. Naval Sea Systems Command, *U.S. Navy Underwater Cutting and Welding Manual*, 1 April 1989.

14. Kou, S., *Welding Metallurgy*, John Wiley and Sons, 1987.

15. Masubuchi, K. and M.B. Meloney, "Underwater Welding of Low-Carbon and High-Strength (HY-80) Steel", *6th Annual Offshore Technology Conference*, OTC 1951, Houston, TX, 1974.

16. Silva, E.A. and T.H. Hazlett, "Shielded Metal-Arc Welding Underwater with Iron Powder Electrodes", *Welding Journal* , vol. 69, no. 8, pp. 59-61, 1990.

17. Szelagowski, P., "Underwater Welding - Present State and Developmental Trends", *Welding Research Abroad*, vol. 38, no. 1, pp. 7-11, January 1992.

18. Liu, S., D.L. Olson and S. Ibarra, "Electrode Formulation to Reduce Weld Metal Hydrogen and Porosity", *OMAE 1994*, vol. III, part A, pp. 291-298, ASME, New York, 1994.

19. Pope, A.M., S. Liu and D.L. Olson, "Effects of the Electrode Oxidizing Potential on Underwater Wet Welds", *OMAE 1994*, vol. III, part A, pp. 361-368, ASME, New York, 1994.

20. Sanchez-Osio, A. and S. Liu, "Influence of Consumable Composition and Solidification on Inclusion Formulation and Growth in Low Carbon Steel Underwater Welds", *Welding Research Council Bulletin*, no. 339, pp. 1-59, February 1995.

21. Sanchez-Osio, A., S. Liu and D.L. Olson, "Designing Shielded Metal Arc Consumables for Underwater Wet Welding in Offshore Applications", *Journal of Offshore Mechanics and Arctic Engineering*, Transactions of the ASME, vol. 117, August 1995.

22. Grubbs, C.E. and O.W. Seth, "Multipass All Position Wet Welding, A New Underwater Tool", *Offshore Technology Conference*, OTC 1620, Houston, TX, 1972.

23. Ozaki, H., J. Naiman and K. Masubuchi, "A Study of Hydrogen Cracking in Underwater Steel Welds", *Welding Journal*, Vol. 56, No. 8, pp. 231s-237s, 1977.

24. Chew, B., "Prediction of Weld Metal Hydrogen Levels Obtained Under Test Conditions", *Welding Journal*, vol. 52, no. 9, pp. 386s-391s, 1973.

25. Tsai, C.L. and K. Masubuchi, "Mechanisms of Rapid Cooling and Their Design Consideration in Underwater Welding", *11th Annual Offshore Technology Conference*, OTC 3469, Houston, TX, 1979.

26. The Welding Institute Report, "Fusion Welding Underwater", *Metal Construction*, pp. 256-258, May 1975.

27. Graville, B.A., Proceeding Welding of HSLA (Microalloyed) Structural Steeels (ROMS), pp. 29, Metals Park, 1978.

28. Lundin, C.D., G. Zhou and K.K. Khan, "Metallurgical Characterization of the HAZ in A516-70 and Evaluation of Fracture Toughness Specimens", *Welding Research Council Bulletin*, no. 403, Report 1, pp. 1-88, July 1995.

29. Ibarra, S. S. Liu and D.L. Olson, "Underwater Wet Welding of Steels", *Welding Research Council Bulletin*, no. 401, pp. 1-39, May 1995.

30. Savage, W.F., E.F. Nippes and E.S. Szekeres, "Hydrogen Induced Cold Cracking in a Low Alloy Steel", *Welding Journal*, vol. 55, no. 9, pp.276s-283s, 1976.

31. Smallman, R.E., *Modern Physical Metallurgy,* Butterworth-Heinemann Ltd., 1992.

32. Kluken, A.O., O. Grong and J. Hjelen, "The Origin of Transformation Textures in Steel Weld Metals Containing Acicular Ferrite", *Metallurgical Transactions A*, vol. 22A, pp. 657-663, March 1991.

33. Kononenko, V.Y., "Effect of Water Salinity and Mechanized Underwater Welding Parameters on Hydrogen and Oxygen Content of Weld Metal", *Welding Under Extreme Conditions, IIW Conference, Helsinki*, pp. 113-118, Pergamon Press, New York, 1989.

34. Christensen, N., "The Metallurgy of Underwater Welding:, *Underwater Welding, IIW Conference, Troadheim, Norway,* pp. 71-94, Pergamon Press, New York, 1983.

35. Grong, O., D.L. Olson and N. Christensen, "On the Carbon Oxidation in Hyperbaric MMA Welding", *Metal Construction*, vol. 17, no. 12), pp. 810R-814R, 1985.

36. Ibarra, S., C.E. Grubbs and D.L. Olson, "Metallurgical Aspects of Underwater Welding", *Journal of Metals*, vol. 40, no. 12, pp. 8-10, 1988.

37. Stalker, A.W., P.H.M. Hart and G.R. Salter, "An Assessment of Shielded Metal Arc Electrodes for the Underwater Welding of Carbon Manganese Structural Steels", *7th Annual Offshore Technology Conference*, OTC 2301, Houston, TX, 1975.

38. Oh, D.W., Olson, D.L. and Frost, R.H. "The Influence of Boron and Titanium Low-Carbon Steel Weld Metal", *Welding Journal*, vol. 69, no. 4, pp. 151-158s, 1990.

39. ASM Handbook Committee, Editor, *Metals Handbook, Fractography*, vol. 12, American Society of Metals, Metals Park, Ohio, 9th Ed, 1987.

INITIAL DISTRIBUTION LIST

Number of Copies

1. Defense Technical Information Center
8725 John J. Kingman Road, Ste 0944
Ft. Belvoir, Virginia 22060-6218 2

2. Dudley Knox Library
Naval Postgraduate School
411 Dyer Rd.
Monterey, California 93943-5101 2

3. Naval/Mechanical Engineering Curricular Office, Code 34
Naval Postgraduate School
Monterey, California 93943-5000 1

4. Department Chairman, Code ME
Department of Mechanical Engineering
Naval Postgraduate School
Monterey, California 93943-5101 1

5. Dr. Alan G. Fox, Code ME/FX
Department of Mechanical Engineering
Naval Postgraduate School
Monterey, California 93943-5101 2

6. Capt. Raymond McCord, SEA OOC
Supervisor of Salvage and Diving
Naval Sea Systems Command
2531 Jefferson Davis Hwy
Arlington, Virginia 22242-5160 1

7. Mr. Michael Dean, SEA OOC5
Supervisor of Salvage and Diving
Naval Sea Systems Command
2531 Jefferson Davis Hwy
Arlington, Virginia 22242-5160 3

8. Lt Robert L. Johnson
Navy Experimental Diving Unit
321 Bullfinch Road
Panama City, Fl 32407-7015 3